Untersuchung der Polarisation und Elektroporation von Lipid-Vesikeln und biologischen Zellen mittels elektro-optischer und konduktometrischer Signalanzeige

I. Oszillatorische Elektro-Deformation von Phospholipid Nanovesikeln und Membran-Leitfähigkeitsänderungen durch Elektroporation in Hochfeld-Pulsen

II. Polarisation und Aggregation von Polystyrene-Latex-Nanoteilchen und von *S. pombe* Hefezellen in elektrischen Feldern

III. Elektroporation und Orientierung von *S. pombe* Hefezellen und *E. coli* Bakterienzellen in elektrischen Feldern

DISSERTATION

zur

Erlangung des

Doktorgrades der Naturwissenschaften

an der Universität Bielefeld

vorgelegt von

Vasil Vangelov Dimitrov

Bielefeld 2013

1. Gutachter: Prof. Dr. E. Neumann
2. Gutachter: Prof. Dr. T. Hellweg

Tag der mündlichen Prüfung: 12. Juli 2013

Inhaltsverzeichnis

Zusammenfassung

Teil I. Die Analyse der elektrooptischen und konduktometrischen Messungen an unilamellaren Lipid-Vesikeln (mittlerer Radius von a = 90 nm gefüllt mit 0.2 M NaCl Lösung, suspendiert in 0.33 M Sucrose- und 0.2 mM NaCl-Lösung) in exponentiell abfallenden elektrischen Feldern der Feldstärke $10 \leq E_0$ /(kV/cm) ≤ 90 (Zeitkonstante τ_E = 154 μs) zeigen, dass zyklische Änderungen in der Vesikelform und in der Membranleitfähigkeit auftreten. Die zwei Maxima in den dichroitischen Turbiditätsrelaxationen lassen sich auf die schnelle Bildung und langsame Ausheilung der Membran-Elektroporen (Hysteresezyklus) zurückführen. Die feldinduzierten strukturellen Übergänge zwischen geschlossenen (C) und porierten (P) Membranzuständen werden mit 2 Typen von Poren, Typ P_1 und Typ P_2, beschrieben. Das Einschwingen der Membranleitfähigkeit und die oszillatorische Gestaltänderung der Vesikel werden in Rahmen eines chemischen Hysteresezyklus in der Porendichte der (größeren) P_2-Poren quantitativ analysiert. Im Hysteresemodell führt der Netto-Ionenfluss durch die P_2-Poren zur transienten Reduktion des Membranfeldes. Zur kinetischen Datenanalyse wurde ein neues Iterationsprogramm entwickelt, um die gekoppelten Struktur-Relaxationsmoden numerisch zu analysieren. Das „Torus-Loch"-Porenmodell liefert die mittleren Porenradien $r_1 = 0.38\ (\pm 0.05)$ nm und $r_2 = 1.7\ (\pm 0.1)$ nm. Die Beobachtung, dass die elektrisch-induzierten Membranporen (in exponentiell langsam-abfallenden elektrischen Feldern) oszillieren, ist richtungsweisend für die Entwicklung neuer Pulsprogramme zur Effizienzerhöhung des elektroporativen Transfers von Wirkstoffen in biologische Zellen.

Teil II. Die feldinduzierten Aggregationsmuster der (kleineren) *Polystyrene Latex* Teilchen rund um die (größeren) *S. pombe* Hefezellen wurden quantitativ auf feldinduzierte Dipol-Dipol Wechselwirkungen zurückgeführt. Die gefundene, unerwartet hohe Polarisierbarkeit der Hefe-Zellen (die nicht mit dem klassischen Polarisations-Model deutbar war), wurde mit einem neuen „Polarizationsfluß"-Modell analysiert. Darin wird das höhere ionische Dipolmoment der Zellen auf die hohe Gegenionendichte und die hohe Ladungsdichte in der Zell-Glycocalyx quantitativ zurückgeführt. Dazu wurde ein neues Simulationsprogramm (finite element, fast differential calculus) entwickelt.

Teil III. Die elektrooptischen Daten der Elektroporation und die Orientierung von ellipsoid-förmigen biologischen Zellen bei niedrigen Frequenzen (unter 3 kHz) zeigen, dass sich die elektrooptischen Messgrößen, die bisher als anomale Orientierungssignale bezeichnet wurden („anomalous orientation signals"), zwanglos durch die im Teil II vorgeschlagene ionische Hoch-Polarisation der Zell-Glycocalyx quantitativ beschreiben lassen. Dieses Hyper-Polarisationsmodell kann auch die beobachtete hohe Elektroporations-Effizienz bei niedrigen Frequenzen beschreiben.

Part I

Accepted publication in **Phys. Chem. Chem. Phys.**

DOI:10.1039/C3CP42873G

Transient oscillation of shape and membrane conductivity changes by field pulse-induced electroporation in nano-sized phospholipid vesicles*

Vasil Dimitrov, Sergej Kakorin and Eberhard Neumann

* Dedicated to Manfred Eigen, the founder of chemical relaxation spectrometry and chemical electric field analysis, at the occasion of his 86th birthday, May 9, 2013

Graphical Abstract

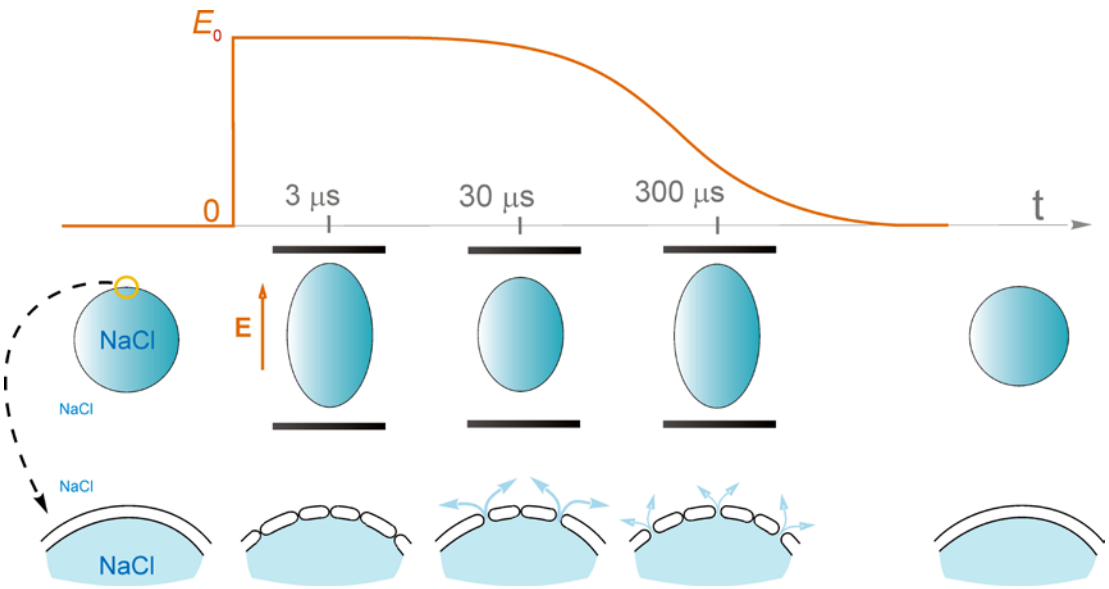

The constant electric field (10μs) causes transient vesicle elongation.
The decaying field (10-200μs) leads to the second transient elongation.
The transients are rationalized by coupling between membrane pores and field.

Phys. Chem. Chem. Phys.

Dynamic Article Links ►

Cite this: DOI: **10.1039/C3CP42873G**

www.rsc.org/xxxxxx

Full Paper

Transient oscillation of shape and membrane conductivity changes by field pulse-induced electroporation in nano-sized phospholipid vesicles*

Vasil Dimitrov,[a] Sergej Kakorin [a,+] and Eberhard Neumann [a]

The results of electrooptical and conductometrical measurements on unilamellar lipid vesicles (of mean radius a = 90 nm), filled with 0.2 M NaCl solution, suspended in 0.33 M sucrose solution of 0.2 mM NaCl, and exposed to a stepwise decaying electric field (time constant τ_E = 154 µs) in the range $10 \leq E_0$ /(kV/cm) ≤ 90, are analyzed in terms of cyclic changes in vesicle shape and vesicle membrane conductivity. The two peaks in the dichroitic turbidity relaxations reflect two cycles of rapid membrane electroporation and slower resealing of long-lived electropores. The field-induced changes reflect structural transitions between closed (C) and porated (P) membrane states, qualified by pores of type P_1 and of type P_2, respectively. The transient change in the membrane conductivity and the transient shape oscillation are based on changes in the pore density of the (larger) P_2-pores along a hysteresis cycle. The P_2-pore formation leads to transient net ion flows across the P_2-pores and to transient changes in the membrane field. The kinetic data are numerically processed in terms of coupled structural relaxation modes. Using the torus-hole pore model, the mean inner pore radii are r_1 = 0.38 (± 0.05) nm and r_2 = 1.7 (± 0.1) nm, respectively. The observation of a transient oscillation of membrane electroporation and of shape changes in a longer lasting external field pulse is suggestive for potential resonance enhancement, for instance, of electro-uptake by, and of electro-release of biogenic molecules from, biological cells in trains of long-lasting low-intensity voltage pulses.

* Dedicated to Manfred Eigen, the founder of chemical relaxation spectrometry and chemical electric field analysis, at the occasion of his 86th birthday, May 9, 2013

[a] Department of Chemistry, Physical and Biophysical Chemistry, Bielefeld University, Bielefeld, Germany

[+] Corresponding author, *sergej.kakorin@uni-bielefeld.de*

1. Introduction

Membrane electroporation (MEP) is an electric technique to induce structural changes in the lipid part of cell membranes or lipid vesicle membranes. Thereby the applied electric field causes the formation of electropores and electromechanical shape changes. The concept of "electroporation", short for electric pore formation, was introduced in 1982 in the context of the first functional electrotransfer of foreign gene DNA into mouse lyoma cells by high voltage pulses.[1-2] This first electro-reprogramming of biological cells by MEP has been seminal for many subsequent biotechnological and clinical applications to transfer biogenic agents into tissue cells, culminating nowadays in gene electro-vaccinations and electro-chemotherapeutical tumour curing.[3-6] Prior and complementary to functional electro-uptake, the electric pulse technique had been used in 1972 to achieve (non-destructive) electro-release of cellular components, such as catecholamines, ATP and proteins from isolated chromaffin granules (vesicles) of bovine adrenal medullae.[7] Similarly, electric pulse trains have been applied to produce large syncythia of living cells by electroporation of aggregates of single cells.[8]

A key observation is that field-induced porous membrane states can be structurally long-lived as compared to the rapid process of pore formation. This longevity is instrumental for the successful use of MEP for cellular material exchange in general and, in particular, for various biotechnological and medical applications. Although the fundamentals of the electroporation phenomena are slowly being elucidated, many application details, in particular for the various electroporation based medical treatments, are still not sufficiently understood.

A specific chemical-physical (i.e., thermodynamic) theory of MEP was based on data of organelles and culture cells,[2] whereas pure physical theories were developed to analyze the electro-

mechanical properties of both, planar and vesicular lipid bilayers,[9 - 15] and cellular systems such as erythrocytes.[16] Despite differences in size and time scales, the induced transmembrane voltage and the curvature effects[17] of cell membranes and of moderately small vesicles are well comparable.[18] Details are given in the Appendix 7. Therefore, with respect to electroporation, the curved membrane shells of lipid vesicles serve traditionally as models for the lipid parts of the membranes of cell organelles and of cells [19 - 21] It has been previously shown that, at higher field strengths (and 10µs field duration), the electro-optical turbidity relaxations of nano-sized lipid vesicles exhibit a pronounced extremum (peak) very similar to the first peak observed here in long-lasting fields.[22] This peculiar feature has been interpreted as being due to a decrease in the membrane field by cross-pore ion conduction, reducing the conductivity factor of the membrane. At that time, however, the first quantitative estimates suffered from too rough approximations as to the specification of the thermodynamic pore fraction, largely overestimating the conductivity factor.

The data of unilamellar lipid vesicles[22] as well as of biological membranes[23] suggested that the electric field can induce two types of ion conducting electropores: (a) short-lived fluctuating hydrophilic single-file pores (here called P_1-pores) involving small salt ions and (b) larger electropores (here called P_2-pores) of higher pore conductivity and permitting actual net transport (e.g., electrolyte release) also of larger ions. The after-field longevity is particularly pronounced for the P_2-pores; the mean life times in nano-sized vesicles are in the order of milliseconds, in cell membranes in the order of seconds and minutes.[23] The two pore types are characterized by different stress balances, leading to two different stable pore sizes. The stress balance in P_1-pores comprises electrical polarization stress, reduced by ion current, and stress due to a line tension in the pore edge.[24 - 26] In P_2-pores there is additionally a stress due to the net outflow of electrolyte, which is caused by the global electric Maxwell stress on the vesicles.

The conventional high-voltage apparatus provided rectangular pulses of 10 µs duration. Here, we use a new variant of applying a field pulse of long-lasting decaying electric field. As previously, the primary electrooptical data are first subjected to a numerical code analysis[27] yielding the surface area function, $f_s(t)$, which is the relative surface area increase due to water entrance accompanying the formation of electropores. The combination of $f_s(t)$ with the kinetics of the conductivity changes permits to determine the mean pore polarization volume, thus the mean pore radius of a specified geometry of the pore. The field dependence of the relaxation times and the amplitudes, respectively, yields the pore polarization energies and the activation volumes of the cyclic membrane permeability changes and of the shape changes.

In the context of the observed transient oscillation of the shape of nano-sized vesicles, it is instructive to recall that giant vesicles (vesicle radius in the order of 10 µm) under special electrolyte conditions, exhibit a transient shape change in long-lasting constant external fields.[11- 15, 27]

In the field of applications of electroporation in human clinical strategies, the use of longer lasting voltage pulses is guided by the original recognition of the longevity of the membrane pore states, permitting massive membrane transport of larger molecules after the pulse train termination.[1-2] The structural feature of pore longevity is instrumental for rationalizing the voltage pulse data for pulse train combination modes of high voltage (HV) pulses and low voltage (LV) pulses and the effects of a time interval between the pulses.[28] Viewed afterwards, the originally applied "exponential field pulses" [1-2] with the longer RC- circuit discharge times, combine the experimental conditions of a sequence of one HV-pulse followed by a long-lasting LV- pulse, thus achieving effective gene transfer in living tissue.[28] Because of less body stress, low voltage-pulses are desired in clinical protocols, but they are less efficient for human gene vaccination and for electro-chemotherapeutic treatments. Therefore, several cycles of field applications are projected to increase the otherwise low small-field efficiency of clinical electroporation treatments. In line with the previous theory-guided experimental approaches, the observation of transient oscillations in membrane transport in lipid vesicles is projected to enter into strategies to optimize field strength and pulse duration of a single pulse in a pulse train. The final aim is to improve the pulse protocols for clinical gene electrotransfer and electrochemotherapy.

2. Materials and methods

2.1 Unilamellar phospholipids vesicles

Unilamellar phospholipid vesicles have been prepared by the extrusion method [21] using the commercial chloroform/methanol extract of 20 (mass) % lecithin (Soy 20 or Avanti 20) kept deep-frozen at –80 °C. The purified extract contains 20 (mass) % phophatydilcholine (PC), 10 (mass) % phosphatidic acid (PA), 30 (mass) % phophatidylethanolamine (PE), 20 (mass) % phophatidylinositol (PI), and 20 (mass) % other not specified lipids from Avanti Polar Lipids.

The electrooptic data of a mixture of synthetic lipids at similar conditions of lipid concentration, buffer, and temperature are similar described here. The mean diameter $\varnothing$ = 180 nm, i.e., the mean vesicle radius a = 90 nm, has been determined by dynamic light-scattering measurements (data not presented). All samples are vesicle suspensions of aqueous 0.2 mM NaCl solution. In order to remove external NaCl, the vesicle suspension is dialyzed against degassed sucrose solution of the same osmolarity (0.33 M sucrose). The vesicle samples are subjected to measurement immediately after preparation. The final total lipid concentration used for the electrooptical measurements is [LT] = 1 mM, corresponding to a vesicle number density of $\rho_v \approx 10^{14} - 10^{16}$ dm^{-3}. For vesicles of radius of a = 90 nm and vesicle number density of $\rho_v \approx 2.4 \times 10^{15}$ dm^{-3}, the average distance between the surfaces of single vesicles is calculated to be about 0.6 µm. Compared with the vesicle diameter of 0.18 µm the suspension may be qualified as diluted, such that the induced dipole forces during the short field pulse is unlikely to induce dielectrophoretic (dipole-phoretic) clustering of vesicles at the low vesicle density.[20]

2.2 The electric field-jump technique

The electric field-jump relaxation technique, originally introduced by Eigen and DeMaeyer,[29] has been further developed such as to achieve simultaneous measurements of field induced

changes both in the electric conductance and in the optical properties of solutions in the time range of 0.1 µs up to about 200 µs with high resolution. Voltage pulses of field strengths up to 100 kV/cm and variable pulse durations are applied to a plate condenser sample chamber, using an extended version of the original cable discharge technology. The diagram of the field-jump relaxation spectrometer is shown in Fig. 1. The sample chambers are thermostated at the temperature T = 293.0 (± 0.1) K (20°C). The electrooptical chamber is equipped with quartz windows and parallel planar graphite electrodes. The electrode distance h can be adjusted between 3 mm and 10 mm, providing additional adjustment of the field strengths. The field-induced changes in the transmittance of plane-polarized light is measured at the wavelength of λ = 365.5 nm (Hg-line, highest intensity). The optical path length of the sample cell is l_{opt} = 10 mm. The triggered discharge of a 1000 m high-voltage cable provides a voltage U of constant amplitude U_0 (10µs) within the first 10 µs followed by a stepwise (exponentially) decaying part $U_0 \cdot \exp[-(t-10\mu s)/\tau_U]$ of the time constant τ_U = 154 µs. Because h is adjustable, the nominal external field function $E(t) = U(t)/h$ is expressed by the step function:

$$E(t) = E_0(10\mu s) + E_0 \exp\left[-\left(t-10\mu s\right)/\tau_U\right] \quad (1)$$

In order to use E(t) in the analysis as a continuous variable, the decrease of E in steps of 10µs (cable-discharge technique) is approximated as a continuous function according to:

$$E(t) = E_0 \exp\left(-t/\tau_E^*\right) \quad (2)$$

In Eq. (2), the step-to-exponential conversion is expressed in terms of a time function $\tau^*_E(t) = [\tau_U + A\cdot\exp(-t/\tau_e)]$, where $A = 5\times10^7$ µs and τ_e = 1 µs, to achieve 1% accuracy relative to the step function.

On a logarithmic scale, the time point t' = 0.2 µs (Fig. 2) is taken as time zero, t = t' – 0.2 µs = 0, for the analysis of the relaxation processes including the Maxwell-Wagner polarization of the vesicles suspended in aqueous NaCl solution.

2.3 Electrooptical turbidity relations (one-chamber system)

The light intensity change ΔI^σ, caused by the electric pulse and measured at the polarization angle σ relative to the direction of the applied external field vector E, is related to the optical density change by

$$\Delta OD^\sigma = OD^\sigma(E) - OD^\sigma = -\log\left(1 + \Delta I^\sigma / I^\sigma\right) \quad (3)$$

where $\Delta I^\sigma = I^\sigma(E) - I^\sigma$ is the light intensity change from I^σ (at E = 0) to $I^\sigma(E)$ in the presence of the electric field E, Fig. 1(a). The terms $OD^\sigma(E)$ and OD^σ_0 are defined as the optical densities at E (> 0) and E = 0, respectively. Generally, OD = A + T, comprising both absorbance (A) and turbidity (T) along the light path length. In the wavelength range where the approximation $A << T$ can be used, the reduction of the intensity of light, passing through the sample, is solely due to light scattering. Therefore, here $\Delta OD^\sigma = \Delta T^\sigma$.

The field induced changes $\Delta T^{\parallel}$ and $\Delta T^{\perp}$ at the two light polarization modes σ = 0° (||, parallel to the external field vector E) and σ = 90° (⊥, perpendicular to E) are given by $\Delta T^{\parallel} = T^{\parallel} - T_0$ and $\Delta T^{\perp} = T^{\perp} - T_0$, respectively. The scaled turbidity minus-mode (turbidity dichroism) is defined by

$$\frac{\Delta T^-}{T_0} = \frac{\Delta T^{\parallel} - \Delta T^{\perp}}{T_0} \quad (4)$$

where T_0 is the turbidity at E = 0, i.e., before field application.

The measured difference $(\Delta T^{\parallel} - \Delta T^{\perp}) \equiv \Delta T^-$ is not simply the classical (orientation) dichroism $\Delta T = \Delta T^{\parallel}_{OR} - \Delta T^{\perp}_{OR}$, originally defined for optical density changes due to pure deformation and orientation. If during the orientation process there is a chemical-structural transition, this is covered by the mixed term $\Delta T^{\sigma}_{OR,CH}$. Analogous to the treatment of absorbance changes,[30] the field-induced turbidity changes may be decomposed into deformation-orientation parts, ΔT^{σ}_{OR}, and structural-chemical parts, ΔT^{σ}_{CH}, according to: [31]

$$\Delta T^{\sigma} = \Delta T^{\sigma}_{OR} + \Delta T_{CH} + \Delta T^{\sigma}_{OR,CH} \quad (5)$$

The measured difference mode ΔT^- is thus explicitly given by: [32]

$$\Delta T^- = \Delta T^{\parallel} - \Delta T^{\perp} = \Delta T^-_{OR} + \Delta T^-_{OR,CH} \quad (6)$$

Therefore, here the (total) term ΔT^- represents the general linear turbidity dichroism, covering both ΔT^-_{OR} and $\Delta T^-_{OR,CH}$.

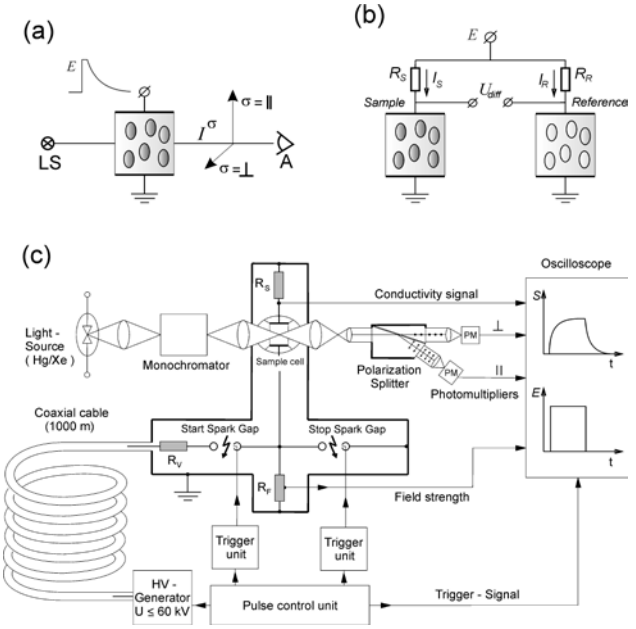

Fig. 1 Principle scheme of the "field-jump" relaxation spectrometer for the measurements of (a) electro-optical relaxations and (b) conductance relaxations of aqueous suspensions of nano-sized lipid vesicles. In (a), I^σ is the intensity of the light after the passage of the sample cell, analysed at polarization angles σ = 0° (||, parallel to the direction of the external field) and σ = 90° (⊥, perpendicular to the field direction), *LS* is the light source and *A* is the analyser. In (b), the tandem-chamber system permits to measure the difference $\Delta Y(t) = Y_{HEC}(t) - Y_{LEC}(t)$ of the conductivity term Y_{HEC} of vesicles of high electrolyte content (HEC), and of Y_{LEC} of vesicles of low electrolyte content (LEC). (c) The network of the components of the relaxation spectrometer set-up.

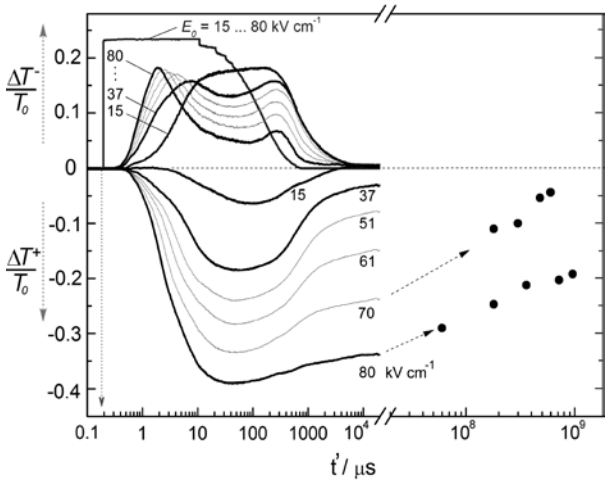

Fig.2 The dichroitic mode, $\Delta T^-/T_0$, and the chemical mode, $\Delta T^+/T_0$, of the turbidity relaxations (at wavelength λ = 365.4 nm) as a function of time at different field strengths E_0 of the applied voltage pulse (one-chamber system). The dots (•) refer to the post-field relaxation values of the plus-mode at E_0 = 70 and 80 kVcm^{-1}. Sample: unilamellar lipid vesicles (high electrolyte content) of mean vesicle radius a = 90(±10) nm; internal [NaCl] = c_{in} = 0.2 M; total lipid concentration [Lt] = 1.0 mM, suspended in isotonic 0.33 M sucrose and 0.2 mM NaCl solution; vesicle number density ρ_V = 2.4 ×10^{12}/ml. The zero-field conductivity of the vesicle suspension is λ_0 = 24.7 µS/cm. Temperature: T = 293 K (20 °C). The onset of the electric field (logarithmic time scale) is at t' = 0.2 µs.

In the line with, e.g., Revzin and Neumann, [33] the plus turbidity mode is given by:

$$\frac{\Delta T^+}{T_0} \equiv \frac{\Delta T_{CH}}{T_0} = \frac{\Delta T^{\parallel} + 2\Delta T^{\perp}}{3T_0} \qquad (7)$$

The turbidity plus-term $\Delta T^+/T_0$ generally refers to non-orientation changes in the scattering cross section. Here, the cross section is changed due to entrance of water (and salt ions like Na^+ and Cl^-) local (aqueous pores) into the electroporated membrane shell as well as due to global changes of the vesicle shape. [31]

2.4 Conductivity relaxation spectrometry (tandem-chamber system)

The electric field pulses for the conductance changes are the same as for the electrooptical changes. In order to compensate for Joule heating and electrode effects, two (equal) chambers in a tandem mode are used, both with identical initial conductivity (λ_0). The field strengths of the high voltage pulses are here in the range 10 ≤ E_0 / (kV/ cm) ≤ 90. The measuring diagram is illustrated in Fig. 1(b). The conductance chambers are equipped with parallel planar graphite electrodes separated by the distance *h*, adjustable within 0.3 ≤ *h* / cm ≤ 1, dependent on the field strength. [32] One of the chambers is filled with vesicles of low electrolyte content (LEC), suspended in low electrolyte solution. The other chamber is filled with vesicles with high electrolyte content (HEC), but suspended in low electrolyte solution. The external solution is adjusted with electrolyte solution, such that the initial conductivities are equal, i.e., the same (λ_0) for both chambers. The other experimental conditions are the same as those for the

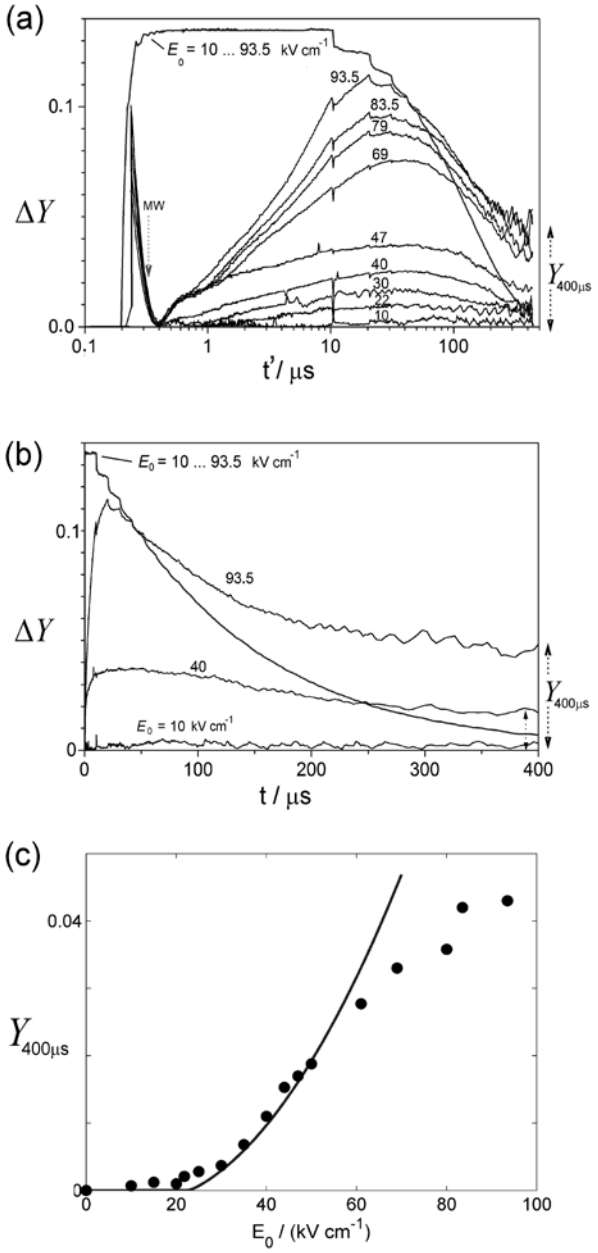

Fig. 3 The difference conductivity function (tandem-chamber system), $\Delta Y(t) = \Delta\lambda_{HEC}(t)/\lambda_0 - \Delta\lambda_{LEC}(t)/\lambda_0$, defined in Eq. (8) as the difference of the conductivity functions of the high electrolyte content (HEC) vesicles and that of the low electrolyte content (LEC) vesicles, as a function of time at different field strengths E_0: (a) logarithmic time scale and (b) linear time scale, t/µs = t'/µs – 0.2. (c) The post-field conductivity value $Y_{400\mu s}$, at t = 400µs, viewed as quasi-stationary, as a function of E_0. The bold curve in (c) corresponds to calculations using Eq. (76), where the mean radius of the release-pores (P_2-pores) r_2 = 1.7 nm (conductivity increase due to the P_2-pores) is used to satisfactorily cover the range from 20 kV/cm up to 50 kV/cm, see section 4.5.3. The vertical MW arrow in (a) indicates the characteristic time constant t_{MW} ≈ 100 ns of the (ionic) Maxwell-Wagner polarization. Experimental conditions as in Fig. 2.

electrooptical measurements (Fig. 2). The primary signals are relative current changes $\Delta i(t)/i_0 = [i(t) - i_0]/i_0$ at a given applied voltage *U*, yielding first the relative conductance change $\Delta g(t)/g_0$ that is then expressed as relative conductivity change $\Delta\lambda(t)/\lambda_0$

(=$\Delta g(t)/g_0$). If now a conductivity function $Y(t) = \Delta\lambda(t)/\lambda_0$ is defined as the relative conductivity change, the tandem-chamber system yields the "difference conductivity function", defined as:

$$\Delta Y(t) = Y_{HEC}(t) - Y_{LEC}(t) = \frac{\Delta\lambda_{HEC}(t)}{\lambda_0} - \frac{\Delta\lambda_{LEC}(t)}{\lambda_0} \quad (8)$$

In Eq. (8), HEC refers to high electrolyte concentration (0.1 M NaCl) in the vesicle and LEC, respectively, to low electrolyte concentration (0.2 mM NaCl, 0.33 M Sucrose) of the vesicle suspension. The initial conductivity of the vesicle suspension is λ_0 = 24.7 µS cm^{-1} before pulsing, measured with a KNICK digital conductometer (Krüss, Hamburg) using low voltage (U = 5 V).

3. Experimental Results and Discussion

3.1 Turbidity relaxation spectra

As seen in Fig. 2, the dichroitic mode ($\Delta T^-/T_0$) passes through two subsequent maxima and, finally at about 10 ms, relaxes to zero. The first maximum occurs at constant external field and is similar to the maximum observed previously at high fields. [22]

Remarkably, the second maximum occurs in the decaying field phase, approximately in the same time range for all applied E_0. On the other hand, the chemical mode $\Delta T^+/T_0$ passes smoothly through a broad minimum before it relaxes along the decaying field. In the field strength range of $0 \le E_0/(\text{kV cm}^{-1}) \le 30$, the post-field time course of the chemical mode returns towards the initial (zero) level. It is remarked that, in this field strength range, the application of a second pulse, some minutes after the first one, yields the same optical response as found for the first pulse. Even a series of several pulses applied within several minutes does not change the optical response.

However, at field strengths $E_0 > 30$ kV/cm, the chemical mode returns only very slowly towards the level before pulsing. Since the chemical mode mainly reflects entrance of water (and ions) into the porous membrane phase (electropores), the slower relaxation mode reflects the longevity of, in particular, the larger membrane electropores. As seen in Fig. 2 , the (negative) peak value of $\Delta T^+/T_0$ gradually increases with increasing field strength. At about E_0 = 70 kV/cm, the signal approaches zero only after about t = 20 min, indicating interference of additional processes.

3.2 Conductivity relaxation spectra

The time course of the "conductivity difference function", ΔY (t), starts at t' = 0.2 µs (log time scale). The onset of the field pulse is concomitant with the onset of the capacitive transient of the Maxwell-Wagner (MW) ionic polarization of the vesicles. The estimated MW time constant of 0.1 µs, see Fig. 3 (a), is close to the calculated value of τ_{pol} = 0.096 µs according to the approximation: [34]

$$\tau_{pol} = aC_m \frac{\lambda_{in} + 2\lambda_{ex}}{2\lambda_{in}\lambda_{ex}}, \quad (9)$$

where C_m = 0.8 µF/cm² is taken as the lipid typical specific membrane capacitance, λ_{ex} the (external) medium conductivity and λ_{in} the conductivity of the vesicle interior.

Subsequent to the Maxwell-Wagner polarization current there is another capacitive current contribution caused by Maxwell stress leading to membrane thinning due to (a) lipid tilting (membrane state C_1, and (b) due to smaller surface depression spots (intrusions) or eventual hydrophobic pores (capacitive-conductive, membrane state C_2, see below). The concomitant (ohmic) part in the total term $\Delta Y(t)$ is caused by the ion-conductive electropores. Remarkably, after the onset of the decay of the external field E_0, the conductivity of the suspension still continues to increase passing through a broad maximum (second peak, in the time range of $10 \le t/\mu s \le 40$) before decaying toward an apparent stationary level which is higher than that before the pulse (Fig. 3 a, b). Obviously, the second kinetic phase confirms that there is (diffusive) after-field continuation of the field-induced release of electrolyte ions from the vesicle interior into the bulk suspension due to pore longevity.

The data analysis suggests that the first kinetic phase (mode I) reflects membrane conductivity changes due to electropores without net release of electrolyte from the vesicle. This pore type (P_1) has been previously interpreted as "Nernst-Planck-pore", transporting in a fluctuating opening phase and in single-file fashion, either a cation or an anion, but not both at the same time.[22] The second (slower) mode (II) is accompanied by net outflow of ions; i.e., in one longer lasting opening phase both cations and anions are transported from the HEC (high-salt) vesicles across the long-lived P_2 - pores.

On the time scale displayed in Fig. 3, the relaxation curves appear to approach a quasi-stationary level at the end of the continuous recording at t = 400 µs. But it is seen that the external electric field still continues to decrease, yet the conductivity difference function $\Delta Y(t)$ approaches the finite limit value $Y_{400\mu s}$. In Fig. 3(c), it is shown that the quasi-stationary value $Y_{400\mu s}$ increases with increasing field strength in a way which is known to be typical for electroporation phenomena. [23]

4. Theory and data analysis

4.1 Nonequilibrium thermodynamic theory of membrane electroporation

Since MEP is a complex electro-mechano-chemical phenomenon involving local structural changes such as pore formations and global geometrical changes of membrane thinning and vesicle shape changes, any MEP theory has to comprise chemical-structural aspects as well as pure physical changes due to Maxwell stress. The analysis of the primary kinetic data (Fig. 2 and Fig. 3) will show that the elongation function $p(t)$ ($p = c/b$, see section 4.4.4) exhibits a first characteristic peak (at constant E_0). For instance, at E_0 = 47 kV cm^{-1}, the peak time point is t_{peak} = 4 µs, see Fig. 4 below. At the same field strength, the conductivity function $\Delta Y(t)$ indicates the (delayed) onset of the formation of P_2-pores at about $t = t_{del}$ = 4 µs.

This peculiar feature suggests that an intermediate pore state is rate limiting in the coupling between the two overall reaction cascades underlying electropore formation. In brief, in line with previous data,[23] the first kinetic phase involves a structural reaction cascade (I) toward forming electropores of the type P_1. The second kinetic phase (II) is delayed and reflects the build-up of pores of larger conductivity, previously called electropores (release pores) of type P_2.

4.2 Reaction scheme for the state transitions of MEP

The structural changes underlying the changes in conductance and vesicle shape have previously been represented by chemical reactions (C) $\rightleftharpoons$ (P) between closed (C) and porous (P) membrane states.[1] The new kinetic data confirm that at least two separate, but coupled, cascades of reaction steps are necessary to describe the kinetics of the electrooptical and conductometrical signals.

4.2.1 Reaction subscheme (I)

The first reaction cascade (I) comprises the reversible state changes and the respective rate coefficients (k_i) according to:

$$\text{(I)} \qquad C \underset{k_{-0}}{\overset{k_0}{\rightleftharpoons}} C_1 \underset{k_{21}}{\overset{k_{12}}{\rightleftharpoons}} C_2 \underset{k_{-1}}{\overset{k_1}{\rightleftharpoons}} P_1 \tag{10}$$

In Eq. (10), the first step ($C \rightleftharpoons C_1$) represents Maxwell stress-induced tilting of the lipids relative to the membrane normal. The state C_2 represents a torus like surface depression or eventually a small hydrophobic pore of diameter of the size of one or two water molecules.[35-36] The conductivity difference relaxations $\Delta Y(t)$ suggest a transient capacitive part $\Delta Y_C(t)$, preceding the actual formation of P_1-pores. In brief, the states C_1 and C_2 model the capacitive-conductive states, both impermeable for small ions (except perhaps for H_3O^+-ions). The kinetic curves up to the first peak (reversal of the dichroitic turbidity mode; see Fig. 2) are found to be described solely by the reaction cascade (I). This part is therefore denoted as the kinetic mode (I).

4.2.2 Reaction subscheme (II)

The second reaction cascade (II) is specified in terms of the two unidirectional reaction branches constituting the hysteresis loop in the sequence of state changes according to:

$$\text{(II)} \qquad P_1 \underset{k_{-11}}{\overset{k_{11}}{\rightleftharpoons}} P_{11} \xrightarrow{k^*_2} P_2 \qquad \uparrow\!\underline{\quad (P^*_2) \quad}\!\downarrow k^*_{-2} \tag{11}$$

The different pathways in the hysteresis scheme II are required to describe the second peak in the oscillatory elongation of vesicles in the decaying field. This second peak in the decaying field is more pronounced than the shoulder of the axis ratio function observed by Riske and Dimova (2005)[12] in giant vesicles after the rectangular field pulse (i.e., at field zero), and may be related to the same mechanism as in our case.

The hysteresis mechanism requires different intermediates for the two hysteresis pathways. Therefore, we model the upper branch of the hysteretic state transition $P_1 \rightleftharpoons P_2$ in terms of intermediate state P_{11} (possibly two P_1 pores in very close contact). Note that, in Eq. (11), P_1 is the end state of the reaction scheme I, Eq. (10).

The actual irreversible step is the unidirectional transition from P_{11} to P_2. The overall hysteresis loop is closed by the unidirectional transition back to pore state P_1. This lower branch probably represents the shrinking of P_2 pores, passing through a different (compared to the upper branch) intermediate state P_2^*. So, the cyclic reaction scheme describes the oscillatory shape changes between the pore states P_1 and P_2, caused by the changes in the membrane field due to ion flow.

4.3 Rate equations.

Conventionally, the reaction modes are described in terms of time constants and amplitudes. Here, the rate equations are formulated such that they can be extended to incorporate 'time dependent amplitudes'. For the case of constant field E_0, the amplitudes $[\bar{X}_i]$ of the membrane states X_i (= C, C_1, C_2, P_1, P_2) are used as the final reference equilibrium states. The kinetics of the field-induced state densities $[X_i(t)]$ is expressed in terms of state density deviations defined as:

$$\delta[X_i(t)] = [X_i(t)] - [\bar{X}_i] \tag{12}$$

Mass conservation implies:

$$\sum \delta[X_i(t)] = 0\,. \tag{13}$$

4.3.1 Kinetic overall phase (I)

The actual pore formation process of the P_1-pores is the intrinsic reaction step $C_2 \rightleftharpoons P_1$ in the cascade (I), Eq. (10). The respective (intrinsic) rate equation is $d[P_1]/dt = k_1[C_2] - k_{-1}[P_1]$, where k_1 and k_{-1} are the rate coefficients. The specific terms $[X_i(t)] = \delta[X_i(t)] + [\bar{X}_i]$, Eq. (12), are now inserted into the rate equation. If in addition, the equilibrium amplitude conditions $d[\bar{X}_i]/dt = 0$ and $k_{-1}[\bar{P}_1] = k_1[\bar{C}_2]$ are used, respectively, the rate equation is rewritten as:

$$\frac{d\delta[P_1(t)]}{dt} = -k_{-1}\delta[P_1(t)] + k_1\delta[C_2(t)] \tag{14}$$

In the actual coupled system, Eq. (10), mass conservation implies that $\delta[P_1(t)] = -\delta[C_2(t)] - \delta[C_1(t)] - \delta[C(t)]$; Eq. (13).

In the case of time dependent amplitudes, the rate equations will be extended to cover the amplitude terms $\bar{X}_i(t)$.

4.3.2 Kinetic overall phase (II)

The observed delay, at about $t_{del} \approx t_{peak\,I}$ (Fig. 3(a)), in the $\Delta Y(t)$ function suggests that the reaction mode (I) can be considered as rapidly equilibrated to the subsequent slower formation of P_2 -pores starting at times $t \geq t_{del}$. The rate equation of the reaction hysteresis (II) involves two unidirectional steps comprising the states P_1, P_{11}, P_2 and P_2, P_2^*, P_1, respectively, Eq. (11). They are here lumped together in terms the respective state densities $[X_i(t)]$ and deviations $\delta[X_i(t)]$.

The overall rate equation covering the intrinsic irreversible steps $P_{11} \rightarrow P_2$ and $P_2 \rightarrow P_1$, respectively, is given by $d[P_2]/dt = k^*_2 \cdot [P_{11}] - k^*_{-2} \cdot [P_2]$, where k^*_2 and k^*_{-2} are the rate coefficients.

Since the actual formation of P_2-pores is slower than the preceding steps, the reaction $P_1 \rightleftharpoons P_{11}$ is considered rapidly equilibrated during the slower step $P_{11} \rightarrow P_2$. Hence $[P_{11}]$ is given by $[P_{11}] = K_{11}[P_1]$. The equilibrium constant $K_{11} = [P_{11}]/[P_1] << 1$ can be expressed in terms of the respective state density deviations as: $K_{11} = \delta[P_{11}] / (-\delta[P_1])$.

The particular feature of the delayed appearance of the P_2-pores above a critical field strength E^* can be rationalized if, at $E \geq E^*$, a critical concentration $[\bar{P}_1^*]$ of the P_1-pores is reached. The peak values are apparently independent of the electric field. This indicates that the respective state density $[P_1(t = t_{peak})]$ is the constant critical pore density $[\bar{P}_1^*]$ for the formation of P_2-pores.

The conditions for the formation of P_2-pores are thus: $[P_1] \geq [\bar{P}_1^*]$ or $\delta[P_1^*] = [P_1] - [\bar{P}_1^*] \geq 0$ at $E \geq E^*$ and at $t \geq t_{del}$.

To incorporate these critical conditions, the rate equation is rewritten as $d[P_2]/dt = k^*_2 K_{11}([P_1] - [\bar{P}_1^*]) - k^*_{-2}[P_2]$, where $[P_{11}] = K_{11}[P_1]$ is used and $[P_1]$ is replaced by the difference $([P_1] - [P_1^*])$. Applying now Eq. (12) and substitution of the equilibrium conditions $d[\bar{P}_2]/dt = 0$ and $k^*_2 K_{11}([\bar{P}_1] - [\bar{P}_1^*]) = k^*_{-2}[\bar{P}_2]$, respectively, yields:

$$d\delta\left[P_2(t)\right]/dt = k_2^* K_{11}\delta\left[P_1^*(t)\right] - k_{-2}^*\delta\left[P_2(t)\right] \qquad (15)$$

where the relationship $\delta[P_1] = [P_1] - [\bar{P}_1] = [P_1] - [\bar{P}_1^*] - ([\bar{P}_1] - [\bar{P}_1^*]) \geq 0$ is used. Note that, at $E \geq E^*$, the maximum (amplitude) of the P_1-pore density, is given by: $[\bar{P}_1] = [\bar{P}_1^*]$. Insertion leads to the equality: $\delta[P_1] = \delta[P_1^*]$; thus all supercritical P_1-pores are converted to P_2-pores.

Mass conservation for the casade (II) for this supercritical range implies that $\delta[P_1^*] = -\delta[P_{11}] - \delta[P_2] = -\delta[P_2]/(1-K_{11})$.

Substitution into Eq. (15) finally leads to:

$$\frac{d\delta\left[P_2(t \geq t_{del})\right]}{dt} = -\frac{1}{\tau_2^{**}}\delta\left[P_2(t \geq t_{del})\right] \qquad (16)$$

where the overall relaxation rate is given by $1/\tau_2^{**} = k_2^* K_{11}/(1-K_{11}) + k_{-2}^*$. In the case of time dependent amplitudes, the rate equation will be extended to cover the amplitude term $[\bar{P}_2(t)] = [\bar{P}_2]\cdot f(t)$ in terms of the forcing function $f(t)$, see section 4.5.

4.3.3 Capacitive contributions to phase (I)

The rate equation for the capacitive current contribution, written in state densities, reads: $d[C_2]/dt = -(k_{21} + k_1)[C_2] + k_{12}[C_1] + k_{-1}[P_1]$. Since lipid tilting is known to be rapid as compared to the slower water entrance to form small hydrophobic pores, the reaction step $C \rightleftharpoons C_1$ is assumed to be rapidly equilibrated. The respective equilibrium constant $K_0 = k_0/k_{-0} = -\delta[C_1]/\delta[C]$ is used to express $\delta[C_1]$ in terms of $\delta[C]$. Rearrangement leads to the (capacitive) reaction mode within the first reaction cascade, Eq. (10). It is expressed in terms of Eq. (12) as:

$$\frac{d\delta\left[C_2(t)\right]}{dt} = -\frac{1}{\tau_C'}\delta\left[C_2(t)\right] + k_C'\,\delta\left[P_1(t)\right] \qquad (17)$$

In Eq. (17), the capacitive relaxation rate $1/\tau'_C = k_1 + 1/\tau'_{12}$ is given in terms of the mode relaxation rate $1/\tau'_{12} = -k'_{12} + k_{21}$ and the rate coefficients k_{21} and $k'_{12} = k_{12}K_0/(1-K_0)$, respectively. The overall capacitive rate coefficient is $k'_C = k'_{12} + k_{-1}$.

Again, in the case of time dependent amplitudes, the rate equations will be extended to cover the amplitude terms $\bar{X}_i(t)$.

4.4 Thermodynamics of electroporation field effects

4.4.1 The induced membrane field

The external electric field directly acts as an electric force on the charged groups of the lipid structure of the membrane and also on the ion transport directly within the electropores; the electric force refers to the induced membrane field E_{ind}. For spherical shells, Maxwell's original solution of the Laplace's equation refers to the stationary values of the electric potential φ_m at the membrane sites of the polar angle θ, i.e., in the angular range $0 \leq \theta \leq \pi$.

In the case of homogeneous external fields, the two hemispheres of the shell may be considered electrically equivalent relative to the direction of the homogeneous external field. Thus, at the pole caps, the induced membrane field $E_{ind} = |\Delta\varphi_m|/d_m$ is collinear with the direction of the external field E, where $\Delta\varphi_m$ is the potential difference between the external and internal membrane sites on the pole capes of vesicles. Thus, for field effects the (hemispherical) polar angle ranges $0 \leq \theta \leq \pi/2$ and $\pi/2 \leq \theta \leq \pi$ are equivalent. In this context it is recalled that the electric current density vector j_m for the cross- membrane ionic flows (of both cation and anion) is given by $j_m = \lambda_m(-\nabla\varphi_m) = \lambda_m E_m$, where λ_m is the conductivity (or specific conductance) of the membrane (referring to the conductive pores) and $E_m = E_{ind}$; here, the Maxwell definition of the field ($E_m = -\nabla\varphi_m$) as negative gradient of the electric potential φ is inherent.

It is recalled that the very primary effect of the external field in ionic solution is the built-up of the (ionic) Maxwell–Wagner polarization leading to the induced electric potential difference $\Delta\varphi_{ind}$ across the membrane shell. In the case of a larger outer shell radius a (the inner radius is $r = a - d_m$), the approximation $d_m/a \ll 1$ may be applied. Hence the time course of the induced potential difference is, analogous to Fricke, [37] given by: [38]

$$\Delta\varphi(\theta,t) = -(3/2)\; a\; E\; f_\lambda\; |\cos\theta|\left[1 - \exp\left(-t/\tau_{pol}\right)\right] \qquad (18)$$

In Eq. (18), f_λ is the conductivity factor, specified below. In the case of larger shells of very low membrane conductivity λ_m, we may use the approximations $d_m << a$, and the inequality $\lambda_m << \lambda_{ex}; \lambda_{in}$. Hence the conductivity factor of spherical shells in ionic medium is approximated by: [22-23]

$$f_\lambda = 1 - \nu\;\lambda_m, \qquad (19)$$

where ν is defined as:

$$\nu = \frac{2\lambda_{ex} + \lambda_{in}}{2\lambda_{ex}\lambda_{in} d_m/a} \qquad (20)$$

The stationary value of the induced membrane field at the polar angle θ is given by

$$E_m(\theta) = \frac{U_m(\theta)}{d_m} = \frac{-\Delta\varphi_m(\theta)}{d_m} = (3/2)\frac{a}{d_m} E\; f_\lambda\; |\cos\theta| \qquad (21)$$

In the case of major vesicle elongation at constant volume ($\Delta V/V_0 \approx 0$), Eq. (21) is replaced by:

$$E_m(p,\theta) = \frac{U_m(p,\theta)}{d_m} = (3/2)\; g_p(\theta)\; \frac{a}{d_m} E\; f_\lambda\; |\cos\theta| \qquad (22)$$

where $g_p(\theta)$ is the shape factor related to the elongation ratio p and the polar angle θ and is given by the approximation:

$$g_p(\theta) = \frac{1 + 0.28\,(p-1)}{\sqrt{p^2\sin^2\theta + \cos^2\theta}} \qquad (23)$$

Eq. (23) is valid in the interval $1 \leq p \leq 3$ with relative accuracy of

3×10^{-3}. The derivation of Eq. (23) is based on the exact solution of $\Delta\varphi_m(p,\theta)$, [39] see Eq. (C3) of ref. 39.

4.4.2 Field dependence of the chemical reaction parameters

If the intrinsic equilibrium constant $K_i = k_i / k_{-i}$ is field-dependent, in general also the respective rate constants k_i and k_{-i} and thus the relaxation times τ_i depend on the local field E_m. The van't Hoff-like relationship for K_i of the formation of aqueous pores of type i, at constant pressure P and constant absolute temperature T, is given by:

$$\left(\frac{\partial \ell n\, K_i}{\partial E}\right)_{P,T} = \frac{\Delta_r M_i}{RT} = \frac{\varepsilon_0(\varepsilon_{Pi} - \varepsilon_L)\, V_{Pi}}{k_B T} E_m \qquad (24)$$

In Eq. (24), ε_0 is the permittivity of the vacuum. At membrane fields E_m > 300 kV/cm, as in our experiments, the dielectric coefficient ε_{Pi} is very near to that of water $\varepsilon_W(293\ \mathrm{K}) = 78$; see the Appendix 8. Thus we use $\varepsilon_{Pi} = \varepsilon_W(293\ \mathrm{K}) = 78$. The dielectric coefficient of the lipid phase is given by ε_L = 2.3; k_B is the Boltzmann constant and V_{Pi} is the local polarization volume of the pore state P_i.

For the two-state transition of the type i, integration of Eq. (24) yields the explicit polarization field dependence of $K_i(E)$:

$$K_i(E) = K_i(0)\exp\left(b_i\, f_{\lambda,i}{}^2\, E^2\right) \qquad (25)$$

In Eq. (25), $K_i(0)$ is the distribution constant at the membrane field $E_m = 0$, i.e., before applying the external voltage pulse. As to the definition of the term $b_i \cdot f_{\lambda,i}$ it is important that in a suspension of vesicles, the thermodynamic and kinetic quantities refer to $|\cos\theta|$-averages of θ on both hemispheres.

Measured quantities like electrical currents reflect electropores on both hemispheres. But the local pore density of the electropores in the membrane shell depends on the membrane field $E_m(\theta, p)$, thus on the polar angle θ.

The averaging comprises the membrane field $E_m(\theta, p)$. It is shown in the Appendix 4, that the θ-average is given by:

$$E_m = \left\langle E_m(p,\theta)\right\rangle = \frac{3}{2}\frac{a}{d_m} f_\lambda\, E\, \left\langle g_p(\theta)\, \cos\theta\right\rangle \approx \frac{3}{2}\frac{a}{d_m} f_\lambda\, E \qquad (26)$$

For the data analysis we use the simple approximation given by Eq. (26). Further, the field parameter b_i (referring to the polarization of the pore water) is specified as:

$$b_i = \left(\frac{3}{2}\cdot\frac{a}{d_m}\right)^2 \frac{\varepsilon_0(\varepsilon_W - \varepsilon_L)}{2k_B T} V_{Pi} \qquad (27)$$

The torus-hole model characterizes V_{Pi} in terms of the inner pore radius r_i according to:

$$V_{Pi} = \pi d_m \left[r_i^2 + r_i\, d_m \frac{(4-\pi)}{4} + d_m{}^2 \frac{(10-3\pi)}{24}\right] \qquad (28)$$

Eq. (28) describes the volume V_{Pi} of the torus-hole as the sum of the inner cylinder volume ($\pi\, d_m\, r_i{}^2$) and the remaining two volume rings of outer radius ($d_m/2 + r_i$).

Recalling Eq. (19), the conductivity factor (of pore type i) is rewritten as: [22- 23]

$$f_{\lambda,i} = 1 - \nu\ \lambda_{m,Pi} \qquad (29)$$

In Eq. (29), $\lambda_{m,Pi}$ is the contribution of the pores of type P_i to the membrane conductivity. Recalling the context of Eq. (20), here λ_{in} = 1.56 S m^{-1} and $\lambda_{ex} = 2.85 \times 10^{-3}$ S m^{-1}, thus $\nu = 3.158 \times 10^3$ S^{-1} m.

For vesicles of outer radius a = 90 nm, membrane thickness d_m = 5 nm, the ratio is d_m / a = 0.0556. Hence the approximation $d_m / a << 1$ is justified only within 5.6 % accuracy.

Similar to Eq. (25), the field dependence of the rate coefficient k_i is given by:

$$k_i(E) = k_i(0)\exp\left(b_i^*\, f_{\lambda,i}{}^2\, E^2\right) \qquad (30)$$

The relaxation rate $1/\tau_i$ can be approximated by:

$$1/\tau_i(E) = \left[1/\tau_i(0)\right]\, \exp\left\{\left(b_i^* - b_i\right) f_{\lambda,i}{}^2\, E^2\right\}, \qquad (31)$$

where $[1/\tau_i(0)] = k_i(0) / K_i(0)$. Eq. (31) is an approximation derived in the Appendix 5. Data analysis yields the activation field parameter b_i^* and the activation volume $V_{Pi}{}^*$.

It will be shown below that, due to the changes in the membrane conductivity, the equilibrium constants and the rate coefficients are "indirectly time dependent". Therefore, a simple integration of the respective differential equations is not possible.

4.4.3 Surface area function and pore density

Before the primary data (Fig. 2) can be used in terms of the structural reaction schemes, the connections to the membrane state densities have to be defined. During pore formation in the membrane, the projected surface area $S(t)$ increases by $\Delta S(t)$, relative to the initial surface area $S_0 = 4\pi a^2$, before pulse application. The surface area function $f_s(t)$ is then defined as relative surface change according to:

$$f_S(t) = \frac{\Delta S(t)}{S_0} = \frac{S(t) - S_0}{S_0} \qquad (32)$$

If $f_{s,C}$ is the small contribution due to the closed membrane states C_1 (tilted lipids) and C_2 (small intrusions or hydrophobic pores), see the reaction scheme (I), and $f_{s,P1}$ is the contribution of the P_1 - pores and $f_{s,P2}$ that of the P_2 - pores, the total surface area function is given by:

$$f_s(t) = f_{s,C}(t) + f_{s,P1}(t) + f_{s,P2}(t) \qquad (33)$$

It will be seen that the experimental results of the transient conductivity term $\Delta Y^C(t)$ (see Fig. 5(a)) suggest that the assumption $f_{s,C}(t) << f_s(t)$ holds true. Therefore, here we may use the approximation:

$$f_s(t) \approx f_{s,P1}(t) + f_{s,P2}(t) \qquad (34)$$

Defining now the surface number-density $[N_i]$ of the N_i pores of type P_i and radius r_i by $[N_i] = N_i / S_0$, the surface area function is expressed in terms of the two pore types P_1 and P_2. For practical purposes, it may be assumed that at zero-field certainly $[N_2(0)] =$

0, whereas $[N_1(0)] = 0$ is a rather rough approximation, but may be justified within the experimental accuracy. The individual pore contributions are given by: $f_{s,P1} = \pi r_1^2[N_1]$ and $f_{s,P2} = \pi r_2^2[N_2]$, respectively. Finally, the pore surface area function is:

$$f_s(t) = \pi r_1^2[N_1] + \pi r_2^2[N_2] \tag{35}$$

Further, the concentration terms in the reaction equations of the membrane states can be replaced by the state surface densities and by number surface densities. For instance, the equilibrium constant $K_i(E)$ for the transition step i can be defined by the respective equilibrium terms:

$$K_i(E) = \frac{[\overline{N}_i(E)]}{[\overline{N}_{i,\max}] - [\overline{N}_i(E)]} \tag{36}$$

In Eq. (36), $[\overline{N}_{i,\max}]$ is the maximum amplitude of the number density, referring to the theoretical limit of pore formation in the membrane shell, assuming no loss of membrane patches, here up to about $E_0 \leq 50$ kV cm^{-1}.

The amplitude $\overline{f}_{s,Pi}$ of the individual function $f_{s,Pi}(t) = \pi r_i^2 [N_i]$ is connected to the thermodynamic pore fraction f_{Pi}. Generally, since fractions are in the range $0 \leq f_{Pi} \leq 1$, the P_i-pore fraction is defined by:

$$f_{Pi}(E_0) = \frac{\overline{f}_{s,Pi}(E)}{\overline{f}_{s,Pi}(\max)} \tag{37}$$

where the fictive maximum $\overline{f}_s(\max)$ refers to the limit of $[\overline{N}_{i,\max}]$ in a given lipid membrane shell. Since for a two-state transition the equilibrium constant is given by $K_i = f_{s,Pi}/(1 - f_{s,Pi})$, the dependence of $f_{s,Pi}$ on the external field E_0 is given by:

$$f_{Pi}(E_0) = \frac{\overline{f}_{s,Pi}(E_0)}{\overline{f}_{s,Pi}(\max)} = \frac{K_i(E_0)}{1 + K_i(E_0)} = \frac{K_i(0)\exp\left(b_i f_{\lambda,i}^2 E_0^2\right)}{1 + K_i(0)\exp\left(b_i f_{\lambda,i}^2 E_0^2\right)} \tag{38}$$

Eq. (38) provides the tool to determine pore polarization volumes (and thus pore radii) from the respective amplitudes of the surface area functions. This classical relationship serves as the reference for the non-classical approach of apparently "time-dependent amplitudes" and "time-dependent equilibrium constants" as required for the description of the hysteretic coupling between membrane conductivity, pore state changes and shape changes.

4.4.4 The electro-deformation functions $p(t)$, $f_V(t)$ and $f_s(t)$

It is recalled that the applied electric field polarizes, and the (tangential) Maxwell stress elongates, the vesicles (of high electrolyte content). If the elongation is modelled in terms of ellipsoids of revolution,[40] the extent of elongation is described by the axis ratio $p = c/b$ of the two principal semi-axes c and b, where $c > b$. Because the electro-elongation is relatively rapid (µs) and the rotational diffusion of the elongated vesicle is slower (usually ms), the long axes of the vesicle spheroids are considered oriented in the direction of the external field vector. The elongation of the spherical vesicle from the initial volume V_0 to $V(t)$ requires that either the vesicle membrane surface area S increases by ΔS, or that the vesicle internal volume V decreases by ΔV, respectively. The elongation function is then expressed as:

$$p = 1 + \Delta p_V + \Delta p_S \tag{39}$$

In Eq. (39), $\Delta p_V = p_V - 1$ and $\Delta p_S = p_S - 1$ are the increases in $p(t)$ at constant vesicle volume and at constant membrane surface area, respectively. The axis ratios p_V and p_S refer to the respective conditions. During the process of pore formation water enters locally the membrane forcing the lipids to form a pore wall. For elongation at constant volume, $p \approx p_V$, $\Delta p_S \approx 0$; thus $p(t)$ is solely a function of $f_s(t)$.

To obtain the surface area functions, the experimental turbidity modes $\Delta T^-/T_0$ and of $\Delta T^+/T_0$ are first subjected to a numerical code analysis[27] yielding the elongation function $p(t)$. The numerical code analysis is based on the solution of the electromagnetic *Mie*-type scattering problem for coated spheroids by separation of variables in a spheroid coordinate system. Fig. 4 shows an example for the elongation function $p(t)$, calculated from the turbidity relaxation data at $E_0 = 47$ kV cm^{-1}. Applying Eq. (A1.1) of the Appendix 1, yields the approximation:

$$f_S(t) = \frac{\Delta S(t)}{S_0} = \alpha\left(p_V(t) - 1\right)^{8/5} \tag{40}$$

where $\alpha = 0.082$.

Analogous to the surface function $f_s(t)$, the volume function $f_V(t)$ is defined by: $f_V(t) = \Delta V(t)/V_0 = [V(t) - V_0]/V_0$. Applying Eq. (A2.1) of the Appendix 2 yields the approximation:

$$f_V(t) = \frac{\Delta V(t)}{V_0} = -\beta\left(p_S(t) - 1\right)^{8/5} \tag{41}$$

where $\beta = 0.118$. Eq. (40) and Eq. (41) are valid in the range $1 \leq p(t) \leq 1.8$ with the accuracy of $\Delta f_{s,V} = \pm 0.003$. It is shown below that, alternatively, the volume function $f_V(t)$ can be determined from the conductometrical data. The exact solutions for $f_s(t)$ and $f_V(t)$ are reproduced in the Appendices 1 and 2. Rewriting Eq. (39) in the form $(p - 1) = (p_V - 1) + (p_S - 1)$ and substitution of Eq. (40) and Eq. (41) yields the final expression:

$$p(t) - 1 = \left(\frac{f_S(t)}{\alpha}\right)^{5/8} + \left(\frac{-f_V(t)}{\beta}\right)^{5/8} \tag{42}$$

Thus, using $p(t)$ calculated from the electrooptical data (Fig. 2) and applying Eq. (42) yields $f_s(t)$, provided $f_V(t)$ is known. The function $f_V(t)$ is determined by measuring the conductivity changes in the suspension of vesicles, see below.

4.4.5 Relaxation kinetics of conductivity changes

Analogous to the surface area function $f_s(t)$, Eq. (33), the difference conductivity function $\Delta Y(t)$, see Eq. (8), of the vesicle suspension involves the contributions of the vesicle membranes $\Delta Y_{ves}(t)$ and of the solution $Y_{sol}(t)$:[22]

$$\begin{aligned} \Delta Y(t) &= \Delta Y_{ves}(t) + Y_{sol}(t) \\ &= \Delta Y_C(t) + \Delta Y_{P1}(t) + \Delta Y_{P2}(t) + Y_{sol}(t) \end{aligned} \tag{43}$$

The vesicle term comprises the 'displacement conductivity' ΔY_C due to both, rapid global lipid tilting and the C_2 membrane states.

The contributions $\Delta Y_{P1}(t)$ and $\Delta Y_{P2}(t)$ result from the field-induced ion-conductive electropores.

The contribution $Y_{sol}(t) = \Delta\lambda_{sol}(t) / \lambda_0$ is due to release of electrolyte solution from the vesicle interior through the electropores of type P_2 in the second relaxation phase (II). The concomitant volume change is given by: [22]

$$f_V(t) = -\xi\, Y_{sol}(t) \tag{44}$$

Applying Eq. (44), the factor ξ can be calculated according to $\xi = (Y_{sol}{}^{max})^{-1} = \lambda_0 / \lambda_{max}$, where $Y_{sol}{}^{max}$ is the maximum value of $Y_{sol} = \Delta\lambda_{sol} / \lambda_0$. For vesicles of radius a = 90 nm, vesicle number density of $\rho_v \approx 2.4 \times 10^{15}$ / L, internal conductivity λ_{in} = 1.56 S/m and the external conductivity $\lambda_{ex} \approx \lambda_0 = 2.85 \times 10^{-3}$ S/m, we obtain $\lambda_{max} = 16.4\ (\pm 0.1) \times 10^{-3}$ S/m, yielding $\xi = 0.174$.

Analogous to Eq. (33), the membrane conductivity function is defined as:

$$\lambda_m(t) = \lambda_C(t) + \lambda_{m,P1}(t) + \lambda_{m,P2}(t) + \lambda_{sol}(t) \tag{45}$$

In Eq. (45), the various contributions are analogous to those in Eq. (43). The conductivity contribution $\lambda_{m,Pi}$ of a pore of type i can be expressed in terms of the conductivity of a single pore λ_{Pi} and the respective surface area function $f_{s,Pi}$ according to: [22 - 23]

$$\lambda_{m,Pi}(t) = \lambda_{Pi}(t) \cdot f_{s,Pi}(t) \tag{46}$$

The field dependence at constant field E_0 is expressed as: [23]

$$\lambda_{Pi}(t) = \lambda^0_{Pi} \exp\left(c_i \left[1 - \nu\, \lambda_{m,Pi}(t)\right] E_0\right) \tag{47}$$

where λ^0_{Pi} is the "zero" field ($E_0 \to 0$) pore conductivity, and the voltage factor c_i is defined by:

$$c_i = \frac{3}{2}\frac{a F}{RT}\left(1 - \frac{r_i}{d_m}\right) n_i \tag{48}$$

In Eq. (48), F is the Faraday constant, R is the gas constant and n_i the shape factor of the (torus-hole) pore type i; Fig. 5(c). Insertion of Eq. (48) into Eq. (46) yields the membrane conductivity contribution of the pores of type P_i:

$$\lambda_{m,Pi}(t) = f_{s,Pi}(t)\ \lambda^0_{Pi} \exp\left\{c_i \left[1 - \nu\, \lambda_{m,Pi}(t)\right] E_0\right\} \tag{49}$$

The solution of Eq. (49) for the term $\lambda_{m,Pi}$ involves a Lambert W-function according to:

$$\lambda_{m,Pi}(t) = \frac{W\left[\, f_{s,Pi}(t)\, c_i E_0\, \nu\, \lambda^0_{Pi} \exp\left(c_i E_0\right)\right]}{\nu\, c_i E_0} \tag{50}$$

where W is the Lambert-W function; see, e.g., ref. 42. Eq. (50) is used for the determination of the respective pore radius from the (experimental) functions $\lambda_{m,Pi}(t)$ and $f_{s,Pi}(t)$.

4.4.6 Vesicle volume function and surface-area function

It is recalled that the Maxwell stress elongates the vesicle and thereby increases the hydrostatic pressure in the vesicle interior. After the formation of electropores, the pressure difference, $\Delta P = P_{in} - P_{ex}$ between vesicle interior and exterior, causes electrolyte efflux from the interior of the vesicles through the membrane pores, thereby reducing the vesicle volume.

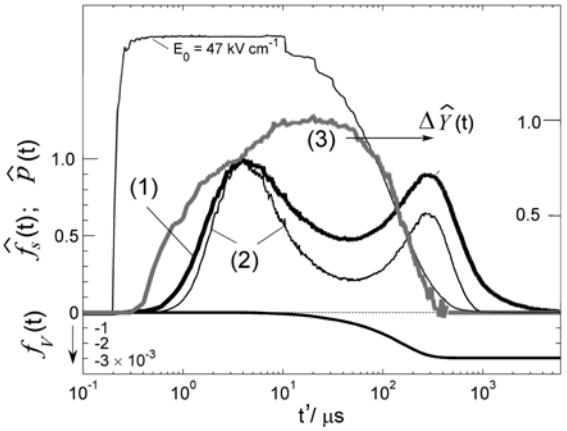

Fig. 4. The calculated time courses of system parameters at E_0 = 47 kV cm^{-1}: (1) The relative elongation function $\hat{p}(t) = \lceil p(t) - 1 \rceil / \lceil p(4\mu s) - 1 \rceil$; (2) the relative surface area function $\hat{f}_s(t) = f_s(t) / f_s(4\mu s)$; (3) the relative difference conductivity function $\Delta\hat{Y}(t) = \Delta Y_{ves}(t) / \Delta Y_{ves}(20\mu s)$ and the relative change of the vesicle volume $f_V(t) = \Delta V(t)/V_0$. All curves (except f_V) are normalized to the values at t = $t_{peak\ I}$ of the first maximum of p(t); here $t_{peak\ I}$ = 4 µs. Experimental conditions are as in Fig. 2.

In the simplest case of a spherical non-conductive vesicle, $\Delta P = (3/20)\varepsilon_0 \varepsilon_w E^2$, [41] where E is the intensity of the applied field strength, ε_0 is the permittivity of the vacuum and ε_w the dielectric coefficient of water; at T = 293 K (20°C), ε_w = 78. If the vesicle membrane contains N_P pores with average pore radius r_p, the volume flow (rate) is described by the Hagen-Poiseuille formula: $dV(t)/dt = -\pi r_p{}^4 N_P \Delta P / (8\eta d_m)$, [20] where $d_m \approx 5 \times 10^{-9}$ m is the membrane thickness and $\eta = 10.02 \times 10^{-4}$ kg m^{-1} s^{-1} is the viscosity of water in the pore volume at the temperature T = 293 K (20°C).

Mean system parameters. It is now for practical reasons of data processing, that the calculation strategy first introduces a formal mean radius $\langle r_p \rangle$ and a formal mean pore number density $[N_P]$ over both pore types such that the total surface area function is specified as:

$$f_S(t) = \pi \langle r_P \rangle^2 \left[N_P(t)\right] = \frac{\langle r_P \rangle^2 N_P(t)}{4a^2} \tag{51}$$

Insertion into the Hagen-Poiseuille formula finally results in:

$$\frac{dV(t)}{dt} = -\frac{3}{40}\frac{a^2 \pi\, \varepsilon_0 \varepsilon_w}{\eta d_m} \langle r_P \rangle^2\ f_s(t)\, E^2 \tag{52}$$

Here, after 10 µs of constant E_0, the external field is a function of time, see Eq. (2). Since, by definition, $\langle r_p \rangle$ is independent of time, the total decrease in the volume function $\Delta V(t) = V(t) - V_0$ is given by the general integral function:

$$\Delta V(t) = \int_{V_0}^{V} dV = -\frac{3}{40}\frac{a^2 \pi\, \varepsilon_0 \varepsilon_w}{\eta d_m} \int_0^t \langle r_P \rangle^2\ f_s(t)\, E^2(t)\, dt \tag{53}$$

In Eq. (53), the general time boundaries are t and t = 0. Data

analysis will show that the volume function is finite only for the time range $t \geq t_{del}$; thus $\Delta V\ (t \geq t_{del}) \geq 0$. Eq. (53) is now used to express the respective volume function as:

$$f_V(t) = \frac{\Delta V(t)}{V_0} = -\, w\, \langle r_P \rangle^2 \int_0^t f_s(t)\ E^2(t)\ dt \qquad (54)$$

where $V_0 = 4\pi a^3/3$ is used to obtain $w = (9/160)\cdot(\varepsilon_0 \varepsilon_w / \eta a d_m)$. Insertion of Eq. (54) into Eq. (41) yields the final form:

$$p(t) - 1 = \left(\frac{f_s(t)}{\alpha} \right)^{5/8} + \left(\frac{w}{\beta} \langle r_P \rangle^2 \int_0^t f_s(t)\ E^2(t)\ dt \right)^{5/8} \qquad (55)$$

It is recalled that $p(t) - 1$ represents the experimentally accessible time-course of the vesicle elongation at a given field strength E_0. In Eq. (55) there are two unknown parameters: the surface area function $f_s(t)$ and the mean pore radius $\langle r_p \rangle$. Both, $f_s(t)$ and $\langle r_p \rangle$, are related to the conductivity function $Y_{sol}(t)$ associated with the release of vesicular electrolyte. Substitution of Eq. (54) into Eq. (44) yields:

$$Y_{sol}(t) = \frac{w}{\xi} \langle r_P \rangle^2 \int_{t_0}^t f_s(t)\ E^2(t)\ dt \qquad (56)$$

At $t = 400$ µs, Fig. 3(c) indicates that $\Delta Y(t)$ appears to level off towards a quasi-stationary value ($Y_{400\mu s}$), where the external electric field is heading towards zero. The number of pores has further decreased due to pore resealing finally approaching zero, too. Therefore, the approximation $\Delta Y_{ves} \approx 0$ is applied to Eq. (43). Hence, towards the end of exponentially decaying electric pulse, $Y_{400\mu s}$ is assumed to refer solely to the solution term $Y_{sol}(t \geq 400\mu s)$. Therefore, the approximation $Y_{sol}(t \geq 400\mu s) = Y_{400\mu s}$ is used for analysis, except for high field strengths, where other processes can decrease the projected surface area.

Calculation of the surface area function $f_s(t)$. Eqs. (54) - (56) together with the boundary condition $Y_{sol}(t \geq 400\ \mu s) = Y_{400\mu s}$ are used to calculate the surface area function $f_s(t)$. In Eq. (55) and Eq. (56), $\langle r_p \rangle$ is a fitting parameter, $p(t)$ and $Y_{400\mu s}$ are experimental data. The procedure of the calculation is outlined in the Appendix 3.

4.4.7 Determination of the inner radius of the P_1 pores.

The membrane conductivity λ_m is related to the relative conductivity change $\Delta\lambda_{ves}/\lambda_0$ due to the electroporation of the vesicles by: [22]

$$\frac{\Delta\lambda_{ves}}{\lambda_0} = \left(\frac{\Delta\lambda_{ves}^{\max}}{\lambda_0}\ \frac{1}{\lambda_m^{\max}} \right) \lambda_m \qquad (57)$$

where $\Delta\lambda_{ves}^{\max}/\lambda_0$ and $\lambda_m^{\max}$ are the maximum values of $\Delta\lambda_{ves}/\lambda_0$ and of λ_m, respectively. Applying the vesicle radius of $a = 90$ nm, the vesicle number density $\rho_v \approx 2.4 \times 10^{15}$ / L, the vesicle-internal conductivity $\lambda_{in} = 1.56$ S m^{-1}, and that of the external medium $\lambda_{ex} \approx \lambda_0 = 2.85 \times 10^{-3}$ S m^{-1}, we obtain $(\Delta\lambda_{ves}^{\max}/\lambda_0) = 3.3 \times 10^{-2}$ and $\lambda_m^{\max} = 1.1 \times 10^{-4}$ S m^{-1}. In the time interval $0 \leq t \leq t_{peak}$, the first kinetic phase $f_s^{(I)}$ reflects dominantly the formation of P_1 pores. Therefore, the time range $0.3 \leq t \leq t_{peak}$ is qualified by $f_s^{\,I}(t)$ $= f_{s,P1}(t)$ and by $\Delta Y_{ves}(\ 0.3 \leq t \leq t_{peak}) = \Delta Y_{ves}^{\,I}(t) = \Delta Y_{P1}(t)$.

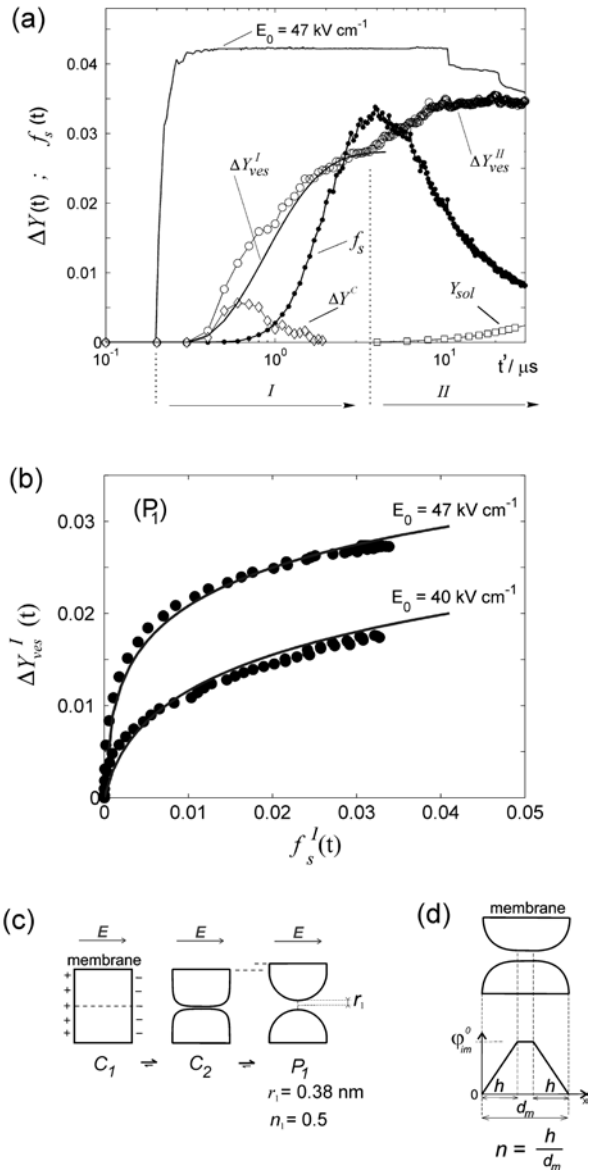

Fig. 5 Calculated parameters: (a) The surface area function $f_s(t)$ (•, connected by an eye-help line); the difference conductivity functions $\Delta Y(t)$ (o, open circles, connected by an eye-help line); $\Delta Y_{ves}^{\,I}(t)$ (bold line), $\Delta Y^C(t) = \Delta Y_{ves}(t) - \Delta Y_{ves}^{\,I}(t)$ (◊) and $Y_{sol}(t)$ (□), at $E_0 = 47$ kV cm^{-1}. Recall that $\Delta Y_{ves}^{\,I}(t) = \Delta Y_{P1}(t)$ and $\Delta Y_{ves}^{\,II}(t) = \Delta Y_{P1}(t) + \Delta Y_{P2}(t)$. It is seen that the concomitant capacitive part is $f_{s,C} \approx 0$. (b) The correlation between $\Delta Y_{ves}^{\,I}(t)$ and $f_s^{\,I}(t)$, each at a given t, at $E_0 = 40$ kV cm^{-1} and 47 kV cm^{-1} in the time range $0.3 \leq t/\mu s \leq t_{peak}$ (of the P_1-pore state). Using Eq. (37) of the text yields the mean inner pore radius $r_1 = (0.38 \pm 0.05)$ nm and the pore shape factor $n_1 = (0.50 \pm 0.01)$. (c) Scheme of the (charged) membrane states C_1 and C_2 and the pore states P_1 and the image force potential barrier at a field E. (d) Scheme of the image potential barrier $\varphi_{im}^{\,0}$ determined by the shape factor n for the thermodynamical treatment of the energy barrier for ions in the pore without molecular details; see Eqs. (47-50).

According to Eq. (8), the electroporative conductivity term of the kinetic phase (I) is described by $\Delta Y_{ves}^{\,I} = Y_{HEC,ves}^{\,I} - Y_{LEC,ves}^{\,I}$. Since $Y_{HEC,\,ves} >> Y_{LEC,\,ves}$, the approximation $\Delta Y_{ves}^{\,I} \approx Y_{HEC,ves}^{\,I} = \Delta\lambda_{ves}^{\,I}(t)/\lambda_0$ applies. Substitution of Eq. (50) into Eq. (57) yields:

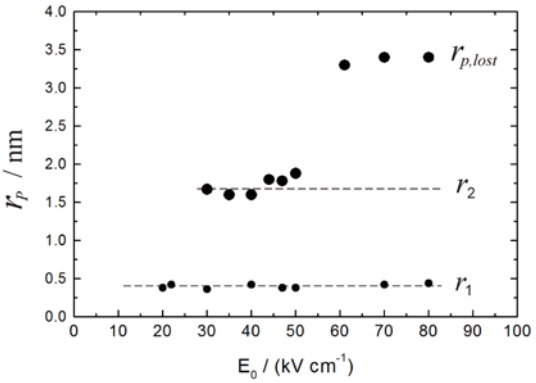

Fig. 6 The calculated (inner) mean radius of the P_1-electropores r_1 = (0.38 ± 0.05) nm, and that of the P_2 – electropores r_2 = (1.7 ± 0.2) nm, as a function of the field strengths E_0 of the applied electric field. The larger values of the P_2 pores at fields $E_0 \geq 50$ kV cm^{-1} reflect imaginary 'larger hole'. The respective membrane area of the large circular hole of effective radius $r_{p,lost}$ is interpreted as a lost membrane patch.

$$\Delta Y_{ves}^{I}(t) = \left(\frac{\Delta\lambda_{ves}^{\max}}{\lambda_0}\right) \frac{W\left[\, f_s^{I}(t)\; c_1 E_0\, \nu\, \lambda_{P1}^{0} \exp(c_1 E_0)\right]}{\nu\, \lambda_m^{\max}\, c_1 E_0} \qquad (58)$$

In Eq. (58), the factor c_1 refers to the inner pore radius r_1 and the pore shape factor n, see Eq. (48). The "zero" field ($E_0 \to 0$) pore conductivity is expressed as $\lambda^0{}_{P1} = [(\lambda_{in}+\lambda_{ex})/2]\cdot\exp(-d_m/r_1)$.[42] In the time range of the kinetic phase (I), see Fig. 5 (a), the difference conductivity function $\Delta Y_{ves}(t)$ also contains the displacement current contributions due to the transitions C ⇌ C_1 ⇌ C_2, such that $\Delta Y_{ves}(t) = \Delta Y_{ves}{}^{I}(t) + \Delta Y^{C}{}_{ves}(t)$, where $\Delta Y^{C}{}_{ves}$ refers to the displacement current contributions. The function $\Delta Y_{ves}{}^{I}(t)$ is obtained by interpolation within the time range of the kinetic phase (I).

Now, $\Delta Y_{ves}{}^{I}(t)$ is set, time point by time point, in relation to $f_s{}^{I}(t)$, see Fig. 5(b). Using Eq. (58), the analysis of variation of the numerical values of the two parameters, r_1 and n simultaneously, for all the time points at all field strengths, respectively, yields as the key result that the mean inner pore radius r_1 = (0.38 ±0.05) nm and the pore shape factor n = (0.50 ± 0.01) are constant, i.e., independent of reaction time and field strengths, see Fig. 6.

4.5 Hysteresis data evaluation

In the case of time dependent electric field $E(t) = E_0\cdot f(t)$, the amplitude $\overline{X}_i(t) = \overline{X}_i \cdot f(t)$, where $\overline{X}_i$ is the conventional time independent amplitude,[29] changes as a response to the forcing-function $f(t) = \exp(-t/\tau_E^*)$; see Eq. (2).

In order to express this feature in terms of practical variables $x_i(t)$ and amplitudes $\overline{x}_i(t) = \overline{x}_i \cdot f(t)$, the initial state densities $[X_i{}^o]$ of the membrane states X_i (= C, C_1, C_2, P_1, P_2) serve as additional reference equilibrium states (at zero external field). Therefore, the kinetics of the field-induced state densities $[X_i(t)]$ are expressed in terms of 'basic state density deviations' (relative to $[X_i{}^o]$) as:

$$\begin{aligned} x_i(t) &= [X_i(t)] - [X_i{}^o] \\ \overline{x}_i(t) &= [\overline{X}_i(t)] - [X_i{}^o] \end{aligned} \qquad (59)$$

Mass conservation dictates that $\Sigma\, x_i(t) = 0$ over all states i. In a similar manner, the amplitudes $\overline{x}_i(t)$ of the density deviations are related by the mass conservation condition: $\Sigma\, \overline{x}_i(t) = 0$.

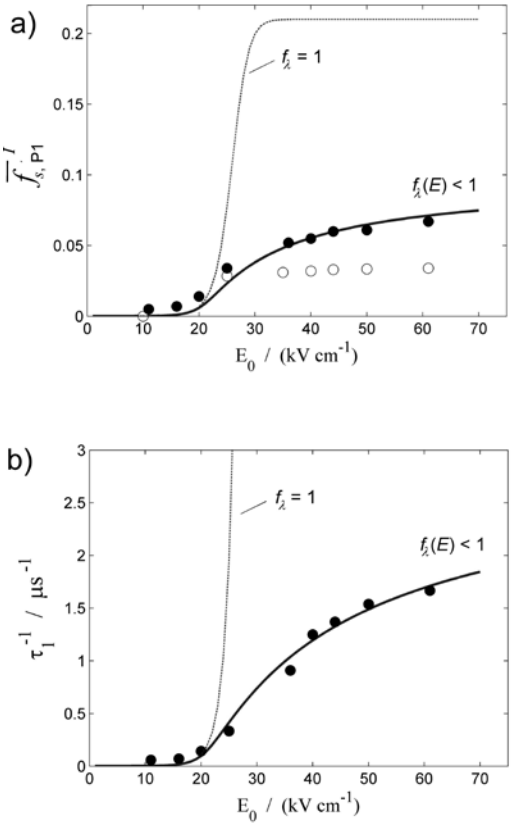

Fig. 7 The dependence (a) of the (virtual) amplitudes and (b) of the relaxation rate $1/\tau_1$ of the kinetic phase $f_s{}^{I}(t)$ due to formation of P_1-pores as a function of the (constant) external electric field strength E_0. Analysis yields (a) the pore polarization volume V_{P1} = 18 (± 2) nm^3 and (b) the activation volume $V_{P1}{}^* = 2V_{P1}$, see section 4.5.4. The open circles (o) in (a) represent the peak values of $f_s{}^{I}(t = t_{peak\,1})$. The peak values are apparently independent of the electric field; this indicates that the respective state density $[P_1(t = t_{peak})]$ is the constant critical pore density $[\overline{P}_1^*]$ for the formation of P_2-pores. See the context of Eq. (15).

Hereafter $i = 0$ denotes membrane state X_0 = C (before electric field application), $i = 3$ is the polarization state C_2, and $i = 1$; 2 refer to the porated membrane states P_1 and P_2, respectively.

4.5.1 Normal modes

Insertion of the terms $[X_i(t)] = x_i(t) + [X_i{}^o]$ and $[\overline{X}_i(t)] = \overline{x}_i(t) + [X_i{}^o]$, Eq. (59), into Eq. (12) yields the 'conventional state density deviations' in terms of 'basic state density deviations':[29]

$$\delta[X_i(t)] = x_i(t) - \overline{x}_i(t) \qquad (60)$$

We now apply Eq. (60) to Eq. (14), Eq. (16) and Eq. (17), respectively.

Since the time constants of all the structural state density changes are very much smaller (in the order of μs) than the time constant of the field decay (τ_E = 154μs, Eq. (2)), it is justified to assume instantaneous adjustment[29] of the amplitudes $\overline{x}_i(t) = \overline{x}_i \cdot f(t)$, $\overline{x}_i$ being independent of time. Thus, if $dx_i(t)/dt$, >> $d\overline{x}_i(t)/dt$, the approximation $d[x_i(t) - \overline{x}_i(t)]/dt = dx_i(t)/dt$ can be justified.

Applying these approximations, we obtain the set of rate equations (ordered in sequence of increasing time constants):

$$\frac{dx_3(t)}{dt} = -\frac{1}{\tau'_C}\left[x_3(t) - \overline{x}_3(t)\right] + k'_C\left[x_1(t) - \overline{x}_1(t)\right] \quad (61)$$

$$\frac{dx_1(t)}{dt} = -k_{-1}\left[x_1(t) - \overline{x}_1(t)\right] + k_1\left[x_3(t) - \overline{x}_3(t)\right] \quad (62)$$

$$\frac{dx_2(t)}{dt} = -\frac{1}{\tau_2^{**}}\left[x_2(t) - \overline{x}_2(t)\right] \quad ; \quad \left(t \geq t_{peak\ I}\right) \quad (63)$$

In Eq. (61) - Eq. (63), the time constants (τ'_C and τ^{**}_2) and rate coefficients (k'_C, k_1 and k_{-1}) are defined in the context of Eq. (14) - Eq. (17).

4.5.2 Integral equations

The rate equations are used to describe the (experimental) relaxation modes $f_{s,P1}(t)$ and $f_{s,P2}(t)$.

First, the two coupled differential equations Eq. (61) and Eq. (62) are solved analytically (see the Appendix 6), yielding the integral equation for $x_1(t)$. The data suggest that the first mode of the surface area function $f_{s,P1}(t)$ can be described in terms of the ratio $x_1(t) / \overline{x}_1 = f_{s,P1}(t) / \overline{f}_{s,P1}$, where $\overline{f}_{s,P1}$ is the amplitude of $f_{s,P1}(t)$. The final solution reads:

$$f_{s,P1}(t) = \overline{f}_{s,P1}\left[\frac{\tau_C\tau_E^*\left(e^{-t/\tau_E^*} - e^{-t/\tau_C}\right)}{\left(\tau_C - \tau_1\right)\left(\tau_E^* - \tau_C\right)} + \frac{\tau_1\tau_E^*\left(e^{-t/\tau_E^*} - e^{-t/\tau_1}\right)}{\left(\tau_1 - \tau_C\right)\left(\tau_E^* - \tau_1\right)}\right] \quad (64)$$

In Eq. (64), the intrinsic time constants τ_C and τ_1 are related to the respective intrinsic rate coefficients by $1/\tau_C = k_{12} + k_{21}$ and $1/\tau_1 = k_1 + k_{-1}$.

Secondly, integration of Eq. (63) in the time range of the kinetic phase (II) leads to the integral equation for $x_2(t)$. Since the data indicate that the second mode of the surface area function $f_{s,P2}(t)$ can be described in terms of $x_2(t) / \overline{x}_2 = f_{s,P2}(t) / \overline{f}_{s,P2}$, where $\overline{f}_{s,P2}$ is the amplitude of the function $f_{s,P2}(t)$. The final solution reads:

$$f_{s,P2}(t) = \overline{f}_{s,P2}\frac{\tau_E^*}{\tau_E^* - \tau_2^{**}}\left[e^{-t/\tau_E^*} - e^{-(t-t_{del})/\tau_2^{**}}\right] \; ; \; \left(t \geq t_{peak\ I}\right) \quad (65)$$

4.5.2 Electrical coupling in the second kinetic phase (II)

In the time interval $t > t_{peak\ I}$ of the operationally denoted second kinetic phase, the fraction f_{Pi}^{II} of electropores pores of type i is formulated as 'electrically' coupled (via the membrane field E_m) to that of the pore type j; note $i, j = 1, 2$; $i \neq j$. Thus, Eq. (38) is rewritten as

$$f_{Pi}^{II} = \frac{\overline{f}_{s,Pi}^{II}}{\overline{f}_{s,Pi}(\max)} = \frac{K_i^{II}}{1 + K_i^{II}} = \frac{K_i(0)\exp\left(b_i f_\lambda^{\,2} E_0^2\right)}{1 + K_i(0)\exp\left(b_i f_\lambda^{\,2} E_0^2\right)} \quad (66)$$

In Eq. (66), the distribution constant K_i (of the ith mode) is expressed in terms of the total conductivity factor f_λ defined as $f_\lambda = 1 - \nu\Sigma_i \lambda_{m,Pi}$, where $\lambda_{m,Pi}$ is the the membrane conductivity due to P_i pores (i =1; 2) and ν is given by Eq. (20).

Recalling Eq. (29), the total conductivity factor is

$$f_\lambda = f_{\lambda,1} + f_{\lambda,2} - 1 \quad (67)$$

Insertion of f_λ , Eq. (67), into Eq. (66) yields

$$K_i^{II} = K_i(0)\exp\left(b_i f_{\lambda,i}^{\,2} E_0^2\right)\; F_{ij} = K_i\;\; F_{ij} \quad ; \quad (i \neq j) \quad (68)$$

where the coupling factor is given by:

$$F_{ij} = \exp\left[-b_i\left(f_\lambda + f_{\lambda,i}\right)\left(1 - f_{\lambda,j}\right)E_0^{\,2}\right] \quad ; \quad (i \neq j) \quad (69)$$

describing the electrical coupling (via E_m) of the ith mode caused by the mode j. Recalling that $f_{s,Pi}(t)$ as well as $E(t)$ are time-dependent, substitution of Eq. (50) into Eq. (29) leads to:

$$f_{\lambda,i}(t) = 1 - \frac{W\left[\; f_{s,Pi}(t)\;\, c_i\, E(t)\, \nu\, \lambda_{Pi}^0 \exp\left(c_i\, E(t)\right)\right]}{c_i\, E(t)} \quad (70)$$

Substitution of Eq. (70) into Eq. (69) yields the time dependence of the coupling function, $F_{ij} = F_{ij}(t)$. In general, $F_{ij}(t)$ varies in the range $0 < F_{ij}(t) \leq 1$.

Since in the kinetic phase (II) $\overline{f}_{sPi}^{\;II} \approx 0.03 << \overline{f}_s(\max) = 0.21$, see Fig. 7(a), i.e., $f_P = [\overline{f}_{sPi}^{\;II} / \overline{f}_s(\max)] \ll 1$, the approximation $\overline{f}_{sPi}^{\;II} \approx \overline{f}_s(\max) \cdot K_i^{\,II} = \overline{f}_s(\max) K_i F_{ij}$ applies. Thus the surface functions of the two kinetic phases are expressed as:

$$f_{s,P1}^{I}(t) = f_{s,P1}(t) \quad ; \quad f_{s,P2}^{I}(t) = 0 \quad (71)$$

$$f_{s,P1}^{II}(t) = f_{s,P1}(t)\;\, F_{12}(t) \quad ; \quad f_{s,P2}^{II}(t) = f_{s,P2}(t)\;\, F_{21}(t) \quad (72)$$

In Eq. (71) and Eq. (72), $f_{s,P1}(t)$ and $f_{s,P2}(t)$ are given by Eq. (64) and Eq. (65), respectively. The total surface function in the kinetic phase (II) is given by:

$$f_s^{II}(t) = f_{s,P1}^{II} + f_{s,P2}^{II} = f_{s,P1}(t)\;\, F_{12}(t) + \; f_{s,P2}(t)\;\, F_{21}(t) \quad (73)$$

The single contributions $f_{s,P1}^{II}(t)$ and $f_{s,P2}^{II}(t)$ are obtained by fitting Eq. (73) to the function $f_s(t)$, calculated as described in section 4.4.6, yielding the amplitudes and the characteristic time constants of the electroporation modes, $\overline{f}_{s,Pi}$ and τ_i, respectively. The parameters r_2 and λ^0_{P2} are adjustable, too, whereas r_1 and λ^0_{P1} are calculated as described in section 4.4.7. In order to approach high accuracy of the calculations, $f_{s,P2}^{II}(t)$ and r_2 are optimized by applying an iterative calculation procedure, see below section 4.5.3.

4.5.3 Calculation of $f_{s,P2}^{II}(t)$, $Y_{sol}(t)$ and r_2

It is recalled that the total surface area function $f_s(t) = \Delta S(t)/S_0$ due to the electropores (calculated as described in section 4.4.6) is viewed in terms of two different phases: phase (I) up to $t = t_{peak\ I}$, and phase (II) at times $t > t_{peak\ I}$, see Fig. 5. Since in the time interval $1 \leq t/\mu s \leq 10$ the external field is constant, the reversal in $f_s(t)$ is due to lowering of the local field across the lipid membrane. The reversal of $f_s(t)$, see Fig. 4, coincides with the onset (at $t > t_{peak\ I}$) of the decrease of the vesicle volume concomitant with release of vesicular electrolyte through the P_2-pores causing the delayed increase in the contribution ΔY_{ves}.

Decrease in vesicle volume and increase in ΔY_{ves}, both indicate the onset of the formation of the larger P_2-electropores. Ion flow through the P_2-electropores starts to appreciably decrease the membrane field and thus total surface area function (due electropores). On the other hand, in the time up to 10 µs at constant E_0, after a short capacitive delay, $f_s(t) = f_s^{\,I}(t)$ starts to increase exponentially with time, suggesting that the local field apparently remains constant. Consistent with the smaller radius of the P_1-pores and thus smaller pore conductance, the P_1-pores dominate the kinetic phase (I). Also, because of lower pore density, the P_1-pores apparently do not appreciably affect the membrane conductivity, thus keeping E_m approximately constant. Therefore, it is justified to apply Eq. (73) and describe the kinetic phase (II) in terms of the total surface area function $f_s^{\,II}(t) = f_{s,P1}^{\,II}(t) + f_{s,P2}^{\,II}(t)$, specified as the set:

$$\frac{f_{s,P1}^{\,II}(t) + f_{s,P2}^{\,II}(t)}{\alpha} = \left[p(t) - 1 - \left(r_2^{\,2} \frac{w}{\beta} \int_{t_{peak}}^{t} f_{s,P2}^{\,II}(t)\; E^2(t)\; dt \right)^{\frac{5}{8}} \right]^{\frac{8}{5}} \quad (74)$$

$$Y_{sol}(t) = \frac{w}{\xi} r_2^{\,2} \int_{t_{peak}}^{t} f_{s,P2}^{\,II}(t)\; E^2(t)\; dt \quad (75)$$

Using the boundary condition $Y_{sol}(t \geq 400\mu s) = Y_{400\mu s}$, Eq. (74) and Eq. (75) are solved for $f_s^{\,II}{}_{,P2}(t)$, $Y_{sol}(t)$ and r_2 by numerical iteration procedures; see the Appendix 3. From the function $Y_{sol}(t)$ we obtain the conductivity change $Y_{ves}(t) = \Delta Y(t) - Y_{sol}(t)$, where $\Delta Y(t)$ is the measured (total) relative conductivity change in the suspension, see Eq. (43).

Some representative results are shown in Fig. 6 - Fig. 8. In Fig. 6, it is seen that at $E_0 < 50$ kV cm^{-1}, both r_1 and r_2 are independent of the field strength. At fields $E_0 \geq 50$ kV cm^{-1}, the calculated mean P_2 pore radius is apparently larger. However, at those fields, the relaxation of the chemical mode (plus-mode) $\Delta T^+/T_0$ does not reach the initial zero value (even 20 min after the electric pulse; Fig. 2). On the other hand, the surface area function $f_s(t)$ always decays to zero after termination of the field pulse. These features are consistent with the suggestion that, at fields $E_0 \geq 50$ kV cm^{-1}, the very slow after-field relaxations of the plus mode reflect pore resealing and loss of membrane, resulting in a slightly smaller vesicle. The lost membrane is probably found in smaller lipid particles like small bicells;[43] see also the Appendix 3.

The proposal of a small lost membrane patch of area $\Delta S_{p,lost} = \pi r_{p,lost}^{\,2} = 38.48$ nm^2 for the observed reduction in the vesicle size (after high field pulsing) is similar to the large lost membrane patch of a single giant vesicle.[44] Alternatively, however, the (irreversible) electrooptical signal changes, observed in our small vesicles (filled with electrolyte) at higher field strength (E > 50 kV/cm) can also be rationalized by the observed decrease in vesicle volume due to release of vesicular electrolyte (across the P_2-pores) resulting in a now wrinkled membrane surrounding the smaller electrolyte volume. Because the small loss of area in the small vesicle would mean a loss of about 100 lipids, a number too small to form very small lipid vesicle, most likely only small bicells are formed.

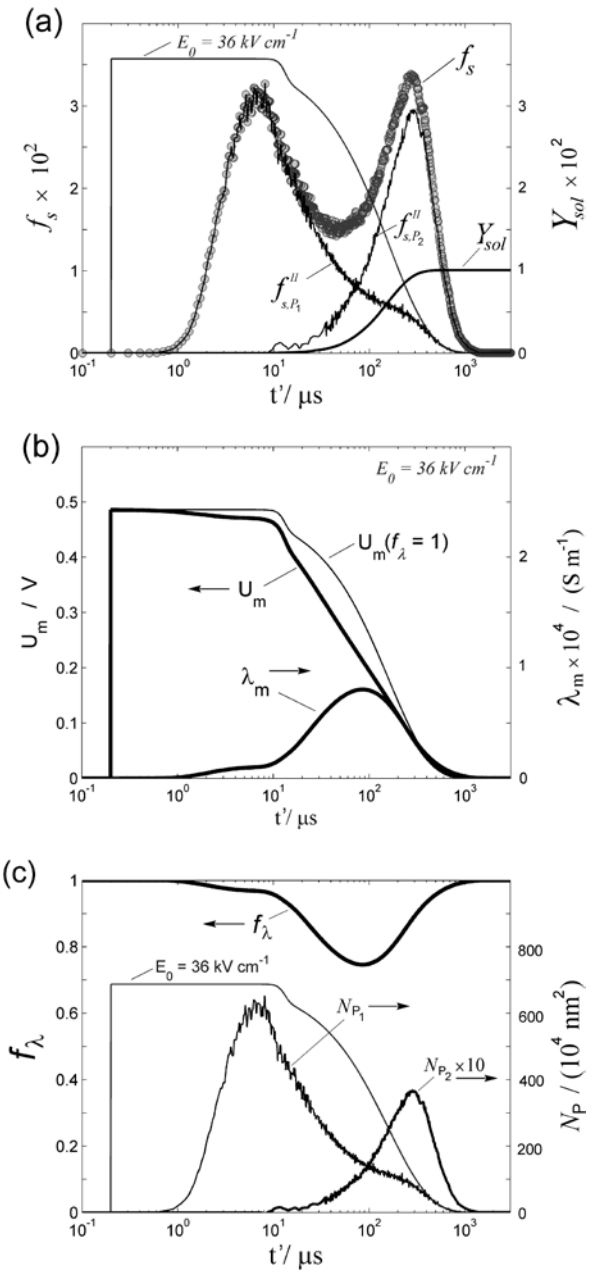

Fig. 8 The kinetics at $E_0 = 36$ kV cm^{-1}. (a) The total surface area function $f_s(t)$ and the calculated surface area functions of the electroporation modes, $f^{|}{}_{s,P1}(t)$ and $f^{|}{}_{s,P2}(t)$, respectively. Curve fit yields the mean inner pore radii $r_1 = 0.38$ nm and $r_2 = 1.7$ nm, and the pore-conductivities (at $E \rightarrow 0$) $\lambda^0{}_{P1} = 1.5 \times 10^{-6}$ S m^{-1} and $\lambda^0{}_{P2} = 1.3 \times 10^{-4}$ S m^{-1}. (b) The mean membrane voltage $U_m(t) = E_m(t) \cdot d_m$ (bold curve); the thin trace represents the membrane voltage for the case of conductivity factor $f_\lambda = 1$. (c) The conductivity factor $f_\lambda(t)$ and the respective numbers $N_P = N_{P1}(t)$ and $N_P = N_{P2}(t)$ of P_1 and P_2 pores per 10^4 nm^2 surface area, respectively, where the reference surface area 10^4 nm^2 is approximately the projected pole cap area of a vesicle.

The total surface area function $f_s(t)$ and the constituent contributions $f_{s,P1}(t)$ and $f_{s,P2}(t)$ at $E_0 = 36$ kV cm^{-1} are shown in Fig. 8(a). The calculated surface area functions $f_{s,P1}(t)$ and $f_{s,P2}(t)$ are used to calculate, applying Eq. (29) and Eq. (70), the membrane conductivity function $\lambda_m(t) = \lambda_{m,P1}(t) + \lambda_{m,P2}(t)$, see Fig. 8(b). The conductivity factor $f_\lambda(t)$ is calculated by applying

Eq. (67) and Eq. (70), see Fig. 8(c). Using Eq. (26)), the transmembrane voltage $U_m(t) = E_m(t) \cdot d_m$ is calculated and shown in Fig. 8(b). The number $N_{Pi}(t)$ of the P_1 and P_2 pores per 10^4 nm^2, see Fig. 8 (c), are calculated using Eq. (35).

4.5.4 Field dependence of $\overline{f}_{s,Pi}(E_0)$ and $1/\tau_i(E_0)$

The field dependence of the amplitudes $\overline{f}_{s,Pi}(E_0)$ of the kinetic phase P_i are analysed using Eq. (38), where the conductivity factor $f_{\lambda,i}$ is given by Eq. (70) applied for the case of the (time independent) amplitudes $\overline{f}_{s,Pi}$ and constant E_0. The parameters in Eq. (38) and Eq. (70) are: $\overline{f}_{s,Pi}(\max)$, λ^0_{Pi}, $K_i(0)$ and the field factor b_i related to the mean inner pore radius r_i (see Eq. (27)). By solving (numerically) the set of equations Eq. (38) and Eq. (70) for $\overline{f}_{s,Pi}$ and $f_{\lambda,i}$ (at given values of the parameters and E_0) we obtain the functions $\overline{f}_{s,Pi}(E_0)$ and $f_{\lambda,i}(E_0)$ which are used to fit the corresponding experimental data sets. The field dependence of the relaxation rates $1/\tau_i(E_0)$ are analysed applying Eq. (31), where $f_{\lambda,i}(E_0)$ is determined by the same parameters as above.

(P_1): The analysis of field dependence of the amplitude $\overline{f}_{s,P1}(E_0)$ and the rates $1/\tau_1(E_0)$ obtained by fitting $f_s(t)$, see section 4.5.2 yields (see Fig. 7): pore volume $V_{P1} = 18\ (\pm 2)$ nm^3 ($r_1 = 0.38$ nm, torus-hole pore model), fictive maximum (at $E \to \infty$; $f_\lambda = 1$) of the amplitude $\overline{f}_{s,P1}(\max) = 0.21\ (\pm 0.02)$, distribution constant (at $E \to 0$) $K_1(0) = 2.0\ (\pm 0.3) \times 10^{-4}$, and the activation volume $V_{P1}^* = 2.00\ (\pm 0.01) \times V_{P1}$. Recall that the conductivity of the P_1-pores at $E \to 0$ is determined by $\lambda^0_{P1} = [(\lambda_{in}+\lambda_{ex})/2]\exp(-d_m/r_1)$.[42] The result for r_1 coincides with that obtained in section 4.4.8.

(P_2): The field dependence of the amplitude $\overline{f}_{s,P2}(E_0)$, Eq. (38), is analysed by fitting the experimental data-set of the conductivity changes in the solution $Y_{400\mu s}$ (see Fig. 3(c)) by applying Eq. (75), where $f_{s,P2}(t)$ and $E(t)$ are expressed in terms of Eq. (65) and Eq. (2). Explicit integration of Eq. (75) within the limits $t_{peak\ I}$ and $t = \infty$, for the simplest case of high field approximation ($E_0 >> 30$ kV cm^{-1}) $\tau_2 << \tau_E$, and recalling that $Y_{sol}(t \geq 400\mu s) = Y_{400\mu s}$, yields the relationship:

$$Y_{400\mu s}(E_0) = (w/\xi)(\tau_E/3)\, E_0^{\,2}\, r_2^{\,2}\, \overline{f}_{s,P2}(E_0) \qquad (76)$$

where w and ξ are defined in the context of Eq. (54). Here we assume the limit case of $\overline{f}_{s,P1}(\max) \approx \overline{f}_{s,P2}(\max) = 0.21$, see Fig. 7(a). Therefore, since $Y_{400\mu s}$ is solely due to P_2-pores, the fictive maximum in Eq. (38) is approximated by $\overline{f}_{s,P2}(\max) = 0.21$. Application of Eq. (76) and Eq. (38) to the experimental quasi-amplitudes $Y_{400\mu s}(E_0)$, Fig. 3(c), yields $r_2 = 1.7\ (\pm 0.1)$ nm, $K_2(0) = 0.024\ (\pm 0.004)$ and $\lambda^0_{P2} = 1.2\ (\pm 0.2) \times 10^{-4}$ S m^{-1}. The so calculated r_2 and λ^0_{P2} coincide with that obtained in sections 4.5.2 and 4.5.3 (see Fig. 6).

5. Summary and conclusions

In summary, the analysis of the electrooptical turbidity modes, $\Delta T^+/T_0$ and $\Delta T^-/T_0$ (Fig. 2), and the conductometrical relaxations (Fig. 3) yields first the geometric quantities $f_s(t) = \Delta S(t)/S_0$ and $f_V(t) = \Delta V(t)/V_0$ and the conductance function $Y_{sol}(t)$ due to electrolyte release. Remarkably, efflux of vesicular electrolyte begins at about the time point $t = t_{peak\ I}$, where the reversal of the function $f_s^{\,I}(t)$, kinetic phase (I), indicates that the membrane electric field E_m starts to decrease (Fig. 5). The reduction of E_m is

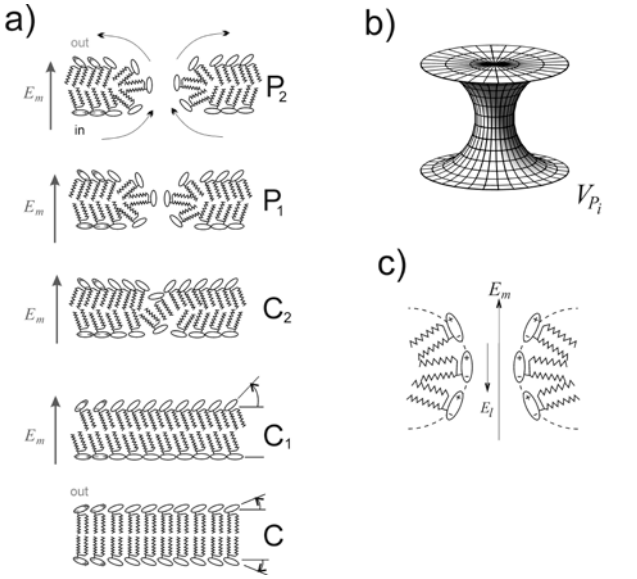

Fig. 9 (a) Schematic representation of the transitions between closed (C) and porous (P) membrane states. In brief, the pore states P_1 and P_2 are "ohmic conductive". The P_2-pores permit net outflow of ions from the high-salt vesicle interior into the medium. The states C_1 and C_2 refer to lipid tilt and depression spots, respectively. (b) The torus-hole model of the Pi pores. (c) The reaction field E_l due to the tilted dipoles of the lipid head groups determines the dielectric properties of the pore water, see App. 8.

dominantly caused by the onset of formation of the net-conductive P_2-pores. Although the inner radius of P_2-pores (1.7 nm) is larger than that of the P_1 pores (0.38 nm), the P_2-pore conductivity is also associated with a nonlinear current-voltage characteristics. The external field reduces the repulsive energy barrier for ions in the pore, thus increasing the pore-conductivity with increasing external electric field. Thus the membrane field $E_m(t)$ is modulated, too.

The nonlinear field strength dependence of the pore-conductivity is the rationale for the oscillatory character of both membrane electroporation and of shape change. When the external electric field starts to decrease with time, the conductivity of both the electropores P_1 and P_2 decreases with time, too, leading here to a second peak in the surface area function $f_s(t)$. Recall, the onset of the P_2-pores is delayed in time.

These features of oscillatory changes in shape and pore densities in non oscillatory external fields are suggestive for potential resonance enhancement, for instance, of electro-uptake by, and electro-release of bioactive molecules from, electroporated cell organelles and cells in low-voltage pulses.

Acknowledgements

The article is part of the Ph.D. thesis of Dipl. Phys. V. D. We thank Dr. C. R. Rabl and Dr. U. Pliquett for the apparative extension of the classical field-jump set-up to apply a high external voltage, decaying (exponentially) in steps of 10 µs by repetitive cable discharge. We thank Prof. Dr. Th. Hellweg for hospitality to establish the final form of the manuscript in his department. E.N. and V.D. thank the GFT e.V. of the University of Bielefeld for financial support by Grant CK 01 (2011-2012) to E.N.

Glossary

a	vesicle radius
d_m	membrane thickness
V; S	vesicle volume; projected vesicle surface
V_{Pi}	polarization volume of pore type P_i
$f_s(t)$	surface area function, $f_s = \Delta S/S_0$
$f_V(t)$	vesicle volume function, $f_V = \Delta V/V_0$
f_{Pi}	pore fraction of pore type Pi
$f_{\lambda,i}$	conductivity factor of pore type Pi
λ_m	membrane conductivity
$\lambda_{m,\,Pi}$	membrane conductivity due to P_i pores
λ_{Pi} (λ^0_{Pi})	pore conductivity of pore type i (at $E \to 0$)
F_{ij}	coupling factor between mode i and mode j
$p(t)$	vesicle elongation function (axis ratio)
X_i	membrane states: C, C_1, C_2, P_1, P_2
$[X_i]$	state (area) density
$[X_i^{\,o}]$	reference equilibrium state (area) density at $E = 0$
$\delta[X_i]$	($= x_i - \overline{x}_i$), conventional state density deviation from the amplitude value $[\overline{X}_i]$
x_i	($= [X_i] - [X_i^{\,o}]$), basic state density deviation from $[X_i^{\,o}]$
$\overline{x}_i$	amplitude value of $x_i(t)$
$\overline{x}_i(t)$	$= \overline{x}_i\, f(t)$, time dependent amplitude
N_i	number of pores of type i (= 1, 2)
$[N_i]$	number (area) density of N_i
W[x]	the Lambert W-function of x

Appendix

Appendix 1: Vesicle Elongation at constant volume.

The constraint of constant internal volume V_0 of an elongated vesicle can be expressed in terms of the elongation factor p_V according to: $V_0 = (4\pi/3)a^3 = (4\pi/3)c^3/p_V^{\,2}$, where a is the radius of initially spherical vesicle, c is the long axis and p_V the axis ratio of the ellipsoid at constant volume V_0.

The relative increase in the projected vesicle surface area, required to elongate a spherical vesicle at constant volume, is given by: [22]

$$\frac{\Delta S}{S_0} = \frac{p_V^{-2/3}}{2} + \frac{p_V^{1/3}\arcsin(\sqrt{1-p_V^{-2}})}{2\sqrt{1-p_V^{-2}}} - 1 \qquad \text{(A1.1)}$$

where $S_0 = 4\pi a^2$ is the initial surface area of the vesicle and $\Delta S = S - S_0$ is the increase in the projected surface area.

For vesicle elongations in the range $1 \le p_V \le 1.8$, Eq. (A1.1) is approximated by Eq. (40) of the main text.

Appendix 2: Vesicle Elongation at constant surface area

When the membrane surface area inclusively the projected area of the membrane pores is constant, the volume reduction required to elongate the vesicle up to the axis ratio p_s is given by the volume function: [22]

$$\frac{\Delta V}{V_0} = p_S^{-2}\left(\frac{\arcsin\sqrt{1-p_S^{-2}}}{2\sqrt{p_S^{-2}-1}} + \frac{p_S^{-2}}{2}\right)^{-\frac{3}{2}} - 1 \qquad \text{(A2.1)}$$

For elongations in the range $1 \le p_s \le 1.8$, Eq. (A2.1) is approximated by Eq. (41) of the main text.

Appendix 3: Calculation of the system parameters

The total (relative) surface area function $f_s(t)$, due to formation of electropores, and the relative conductivity change in the suspension $Y_{sol}(t)$, due to net release of electrolyte from the vesicle interior, are calculated using the approximation $Y_{sol}(t \ge 400\mu s) = Y_{400\mu s}$ by solving the set of equations:

$$f_s(t) = \alpha\left[p(t) - 1 - \left(\langle r_P\rangle^2 \frac{w}{\beta}\int_0^t f_s(t)\; E^2(t)\; dt\right)^{5/8}\right]^{8/5} \qquad \text{(A3.1)}$$

$$Y_{sol}(t) = \frac{w}{\xi}\langle r_P\rangle^2 \int_0^t f_s(t)\; E^2(t)\; dt \qquad \text{(A3.2)}$$

In Eq. (A3.1) and Eq. (A3.2), $\langle r_p\rangle$ is the adjustable parameter; $p(t)$ is calculated from the turbidity modes $\Delta T^-(t)/T_0$ and $\Delta T^+(t)/T_0$, and $Y_{400\mu s}$ is experimentally determined (Fig. 3 of the main text).

Calculation of $f_s(t)$. For a given E_0, Eq. (A3.1) and Eq. (A3.2) are solved for $f_s(t)$ and $Y_{sol}(t)$. The actual fit parameter $\langle r_p\rangle$ is obtained starting with the initial guess of $\langle r_p\rangle$ = 1 nm and heading iteratively to the optimum $\langle r_p\rangle_{optim}$, for which $Y_{sol}(t \ge 400\mu s) = Y_{400\mu s}$ (Eq. (A3.2)) is satisfied. If $Y_{sol}(t \ge 400\mu s) = Y_{400\mu s}$ is not satisfied, the calculation is repeated by taking another $\langle r_p\rangle$ value, until $Y_{sol}(t \ge 400\mu s) = Y_{400\mu s}$ holds. The iterative approach for solving Eq. (A3.1) starts from an initial guess $f_s^{(0)}(t)$ and continues by computing the subsequent function $f_s^{(n)}(t)$ based on (the old one) $f_s^{(n-1)}(t)$:

$$f_s^{(1)}(t) = \alpha\left[p(t) - 1 - \left(\frac{w}{\beta}\langle r_P\rangle^2 \int_0^t f_s^{(0)}(t)\ E^2(t)\ dt \right)^{\frac{5}{8}} \right]^{\frac{8}{5}}$$

$$f_s^{(2)}(t) = \alpha\left[p(t) - 1 - \left(\frac{w}{\beta}\langle r_P\rangle^2 \int_0^t f_s^{(1)}(t)\ E^2(t)\ dt \right)^{\frac{5}{8}} \right]^{\frac{8}{5}}$$

…

$$f_s^{(n)}(t) = \alpha\left[p(t) - 1 - \left(\frac{w}{\beta}\langle r_P\rangle^2 \int_0^t f_s^{(n-1)}(t)\ E^2(t)\ dt \right)^{\frac{5}{8}} \right]^{\frac{8}{5}} \qquad \text{(A3.3)}$$

until $|f_s^{(n)}(t) - f_s^{(n-1)}(t)| \le 10^{-5}$ applies for any t. At any iteration step (n), the approximate solution $f_s^{(n)}(t)$ is constrained by the real root values guided by the condition:

$$(p(t) - 1) - \left(\frac{w}{\beta}\langle r_P\rangle^2 \int_0^t f_s^{(n)}(t)\ E^2(t)\ dt \right)^{\frac{5}{8}} \ge 0 \qquad \text{(A3.4)}$$

If the values of the function $f_s^{(n)}(t)$ are complex numbers, $f_s^{(n)}(t)$ refers to a 'lost membrane patch'. Lost membrane patches have been visualized in giant lipid vesicles[44], in erythrocyte ghosts,[45] and cells.[46] Here, the respective lost fractional area $f_{s,\,lost} = r_{p,lost}^2 / 4a^2$ is associated with a single fictive membrane pore (patch) of radius $r_{p,lost}$, see Eq. (51) of the main text. Therefore, if $f_s^{(n)}(t)$ becomes a complex number, we consider $f_s^{(n)}(t) \equiv f_{s,lost}$ and $\langle r_p\rangle \equiv r_{p,lost}$.

As judged from the very small reduction of the size of the vesicle after pulsing, the increase in curvature due to removing a lipid patch of radius $r_{p,lost}$ = 3.5 nm (see Fig. 6) is extremely small. Quantitatively, the area of the lost patch is $\Delta S_{p,lost} = \pi r_{p,lost}^2$ = 38.49 nm^2, the area of the vesicle membrane is $S_0 = 4\pi a^2 = 1.02 \times 10^5$ nm^2 leading to the relative decrease in the vesicle surface area by $\Delta S_{p,lost} / S_0 = 3.78\times10^{-4}$. This corresponds to an increase in the curvature by 0.019 %. Thus, with respect to the membrane electroporation, the energy contribution of the curvature change is negligibly small.

The initial guess-function $f_s^{(0)}(t)$ in the iteration (see Eq. (A3.3)) is deduced by taking a time-independent (averaged) function $\langle f_s\rangle \equiv \langle f_s(t)\rangle$ in the integral of Eq. (A3.2). Applying now the approximation $E(t) = E_0\cdot\exp(-t/\tau_E)$ with τ_E = 154 µs, and integrating Eq. (A3.2) under the boundary condition $Y_{sol}(t \ge 400\mu s) = Y_{400\mu s}$, we obtain the approximation:

$$Y_{sol}(t) \approx Y_{400\mu s}\left[1 - \exp\left(-2t/\tau_E\right)\right] \qquad \text{(A3.5)}$$

Substitution of Eq. (A3.5) into $f_s(t) = \alpha[p(t) - 1 - (\xi\, Y_{sol}(t)/\beta)^{5/8}]^{8/5}$ (obtained by combining Eq. (A3.1) with Eq.(A3.2)) leads to the first approximation of the surface area function:

$$f_s^{(0)}(t) = \alpha\left[p(t) - 1 - \left(\frac{\xi}{\beta} Y_{400\,\mu s}\left[1 - \exp(-2t/\tau_E)\right] \right)^{\frac{5}{8}} \right]^{\frac{8}{5}} \qquad \text{(A3.6)}$$

Calculation of the specific parameters $f_{s,P2}^{\ II}(t)$, $Y_{sol}(t)$ and r_2. Using the boundary condition $Y_{sol}(t \ge 400\mu s) = Y_{400\mu s}$ (at given E_0), Eq. (74) and Eq. (75) of the main text are solved for $f_{s,P2}^{\ II}(t)$, $Y_{sol}(t)$ and $r_{2,optim}$ by applying an iterative numerical approach analogous to that for $f_s(t)$ and $Y_{ves}(t)$; see Eq. (A3.3). First, Eq. (74) is rewritten as:

$$\frac{f_{s,P2}^{II}(t)}{\alpha} = \left| \left[p(t) - 1 - \left(r_2^{\,2} \frac{w}{\beta} \int_0^t f_{s,P2}^{II}(t)\ E^2(t)\ dt \right)^{\frac{5}{8}} \right]^{\frac{8}{5}} - f_{s,P1}^{II}(t) \right|. \qquad \text{(A3.7)}$$

By applying now the iteration Eq. (A3.3) to Eq. (A3.7), where r_2 is the optimization parameter, Eq. (A3.7) and Eq. (75) of the main text are solved for $f_{s,P2}^{\ II}(t)$. The actual fit parameter r_2 is obtained starting with the initial guess of r_2 = 1.5 nm and heading iteratively to the optimum $r_{2,optim}$ = (1.7 ± 0.2) nm for which $Y_{sol}(t \ge 400\mu s) = Y_{400\mu s}$ (Eq. (A3.2)) is satisfied. The initial guess in the iteration $f_{s,P2}^{II(0)}(t)$ as well as the surface function $f_{s,P1}^{II}(t)$ are obtained by fitting the total surface function $f_s(t)$ with Eq. (73) of the main text.

Appendix 4: The θ-average of $E_m(\theta)$.

Spherical vesicle. The polarization free energy of the membrane pore in an electric field is $W_P = -1/2\cdot V_P\cdot\varepsilon_0(\varepsilon_P - \varepsilon_L)E_m^2$, where V_P is the pore volume. It is recalled that the stationary induced membrane field E_m at the polar angle θ is given by $E_m(\theta) = (3/2)\cdot(a/d_m)\cdot f_\lambda\cdot E_0\,|\cos\theta\,|$, Eq. (21) of the main text. Since the polar distribution of pores is symmetric with respect to the vesicle equator, we shall discuss the relative probabilities of the various positions in the range $0 \le \theta \le \pi/2$.

If there is no field ($E_0 \to 0$), we have $W_P = 0$ for every θ, and all pore positions on the vesicle surface have the same probability. Therefore the probability $p(\theta)d\theta$ of having a pore at the polar angle θ between θ and $\theta + d\theta$ is given by:

$$p(\theta)d\theta = \frac{2\pi a^2 \sin\theta d\theta}{\int_0^{\pi/2} 2\pi a^2 \sin\theta d\theta} = \frac{2\pi a^2 \sin\theta d\theta}{4\pi a^2/2} = \sin\theta d\theta \qquad \text{(A4.8)}$$

When a field is present, a weight factor $\exp(-W_P/k_BT)$ must be introduced. Thus, the probability is given by:

$$p(\theta)d\theta = Ae^{B\cos^2\theta}\sin\theta d\theta \qquad \text{(A4.9)}$$

In Eq. (A4.9), the field factor B is related to the external field E_0 as well as to the pore volume V_{Pi} of a pore of type i and to the conductivity factor $f_{\lambda,i}$ by:

$$B = \left(\frac{3}{2}\right)^2 \frac{V_{Pi}\, a^2 \varepsilon_0 \left(\varepsilon_P - \varepsilon_L\right)}{2 k_B T\, d_m^{\,2}}\; f_{\lambda,i}^{\,2}\, E_0^{\,2} \qquad \text{(A4.10)}$$

Since the probability to find a pore within the total range is $\int_0^{\pi/2} p(\theta) d\theta = 1$, the factor A is given by:

$$A = \left[\int_0^{\pi/2} e^{B\cos^2\theta} \sin\theta d\theta \right]^{-1} \qquad \text{(A4.11)}$$

From Eq. (A4.9) we obtain the $\cos\theta$-average:

$$\left\langle \cos\theta \right\rangle = \frac{\int_0^{\pi/2} \cos\theta\, e^{B\cos^2\theta} \sin\theta d\theta}{\int_0^{\pi/2} e^{B\cos^2\theta} \sin\theta d\theta} \qquad \text{(A4.12)}$$

Elongated vesicle. For a prolate spheroid, the magnitude of the radius vector $\rho(\theta)$ is given by $\rho(\theta) = c\ (p^2\sin^2\theta + \cos^2\theta)^{-1/2}$. The respective surface element is $dS = \rho\,[\rho^2 + (\partial\rho/\partial\theta)^2]^{1/2} \sin\theta\, d\theta\, d\theta$. Recalling $p = c / b$, the average of the product $g_p(\theta)\cdot\cos\theta$, analogous to Eq. (A4.12), is given by:

$$\left\langle g_p(\theta)\cdot\cos\theta \right\rangle = \frac{\int_0^{\pi/2} g_p(\theta)\cdot\cos\theta\; e^{B\cos^2\theta}\; J_p(\theta)\cdot\sin\theta d\theta}{\int_0^{\pi/2} e^{B\cos^2\theta}\; J_p(\theta)\cdot\sin\theta d\theta} \qquad \text{(A4.13)}$$

where

$$J_p(\theta) = \frac{\sqrt{\left(p^2\sin^2\theta + \cos^2\theta\right)^2 + \left(p^2-1\right)^2 \sin^2\theta\cos^2\theta}}{\left(p^2\sin^2\theta + \cos^2\theta\right)^2} \qquad \text{(A4.14)}$$

Since B is given by Eq. (A4.10), Eq. (29) and Eq. (50) of the main text yield the time independent conductivity factor:

$$f_{\lambda,i} = 1 - W\left[f_{s,Pi}\, c_i\, E_0\, \nu\, \lambda_{Pi}^0 \exp\left(c_i E_0\right)\right] \Big/ c_i E_0 \qquad \text{(A4.15)}$$

In Eq. (A4.15), $f_{s,P1}$ varies in the range $0 \le f_{s,P1}(t) \le 0.03$. The average $\langle f_{s,P1}(t)\rangle = [\int f_{s,P1}(t)dt] / t_{peak\,I}$ for the range $0 \le t \le t_{peak\,I}$ is $\langle f_{s,P1}(t)\rangle \approx 0.012$. Since $r_1 = 0.38$ nm and $\lambda^0_{P1} = [(\lambda_{in}+\lambda_{ex})/2] \cdot\exp(-d_m/r_1)$, [42] we obtain the function $f_{\lambda,1}(E_0)$, and thus $B(E_0)$. Substitution in Eq. (A4.13) yields the field dependence of $\langle g_p(\theta)\cdot\cos\theta\rangle$ in the range $0 \le E_0/(\text{kV cm}^{-1}) \le 90$, see Fig. A4. For $E_0 > 30$ kV cm^{-1}, the approximation $\langle g_p(\theta)\cdot\cos\theta\rangle \approx 1$ holds true with the accuracy ≤ 5%, see Eq. (26) of the main text.

Appendix 5: The field dependence of $1/\tau_1$

Since $K_i = k_i / k_{-i}$, Eq. (30) of the main text, the equilibrium constant $K_1(E)$ of the formation of the P_1-pores is given by:

$$K_1(E) = K_1(0)\; e^{b_1 f_{\lambda,1}^2 E^2} = \frac{k_1(0)\; e^{b_1^* f_{\lambda,1}^2 E^2}}{k_{-1}(0)\; e^{b_{-1}^* f_{\lambda,1}^2 E^2}} \qquad \text{(A5.1)}$$

The relaxation rate $1/\tau_1$ of the P_1-formation is specified as:

$$\frac{1}{\tau_1} = k_1 + k_{-1} = k_1\left(1 + \frac{k_{-1}}{k_1}\right) = k_1 \frac{1+K_1}{K_1} = k_1 \frac{1}{f_{P1}} \qquad \text{(A5.2)}$$

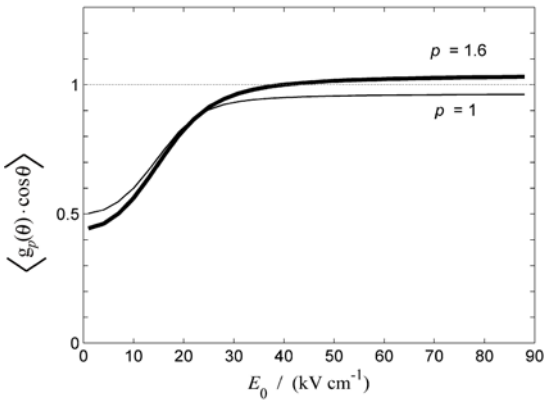

Fig. A4 The average of the product $g_p(\theta)\cdot\cos\theta$ covering the region $0 \le \theta \le \pi/2$ for the elongation ratio $p = 1$ (spherical vesicle, thin line) and $p = 1.6$ (ellipsoid, bold line) as function of E_0.

Insertion of the low-field approximation $f_{P1} \approx K_1(0) \cdot\exp(b_1 f_{\lambda,1}^{\,2} E^2)$, Eq. (38) of the main text, into (A5.2) yields:

$$\frac{1}{\tau_1} = \frac{k_i(0)\; e^{b_1^* f_{\lambda,1}^2 E^2}}{K_1(0)\; e^{b_1 f_{\lambda,1}^2 E^2}} = \frac{k_i(0)}{K_i(0)} e^{\left(b_1^* - b_1\right) f_{\lambda,1}^2 E^2} \qquad \text{(A5.3)}$$

At $E = 0$, the relaxation rate is given by $1/\tau_1(0) = k_1(0)/K_1(0)$. Substitution yields:

$$\frac{1}{\tau_1(E_0)} = \frac{1}{\tau_1(0)} \exp\left[\left(b_1^* - b_1\right)\; f_{\lambda,1}^2\; E^2\right] \qquad \text{(A5.4)}$$

Appendix 6: Solution of Eq. (61) and Eq. (62).

Using the notations $y_1 \equiv x_3$ and $y_2 \equiv x_1$, the set of equations, Eq. (61) and Eq. (62), is rewritten in the more convenient matrix form:

$$\begin{pmatrix} dy_1(t)/dt \\ dy_2(t)/dt \end{pmatrix} + \begin{pmatrix} a_{11} & a_{12} \\ a_{21} & a_{22} \end{pmatrix} \begin{pmatrix} y_1(t) \\ y_2(t) \end{pmatrix} = \begin{pmatrix} a_{11} & a_{12} \\ a_{21} & a_{22} \end{pmatrix} \begin{pmatrix} \overline{y}_1(t) \\ \overline{y}_2(t) \end{pmatrix}, \qquad \text{(A6.5)}$$

where

$$\begin{aligned} a_{11} &= -k'_{12} + k_{21} + k_1 & a_{12} &= -k'_{12} - k_{-1} \\ a_{21} &= -k_1 & a_{22} &= k_{-1} \end{aligned} \qquad \text{(A6.6)}$$

Solving the characteristic equation of Eq. (A6.5), $|a_{ij} - \lambda\delta_{ij}| = 0$, we obtain

$$\lambda_{1,2} = \frac{1}{\tau_{1,2}} = 1/2\left(\Sigma\mathbf{k} \pm \sqrt{\left(\Sigma\mathbf{k}\right)^2 - 4\Pi\mathbf{k}}\right) \qquad \text{(A6.7)}$$

where

$$\begin{aligned} \Sigma\mathbf{k} &= -k'_{12} + k_{21} + k_1 + k_{-1} \\ \Pi\mathbf{k} &= -k'_{12}k_1 - k'_{12}k_{-1} + k_{21}k_{-1} \end{aligned} \qquad \text{(A6.8)}$$

For initial conditions $y_i(0) = 0$ and $\overline{y}_i(0) = 0$, the general solution of Eq. (A6.5) is given by: [47]

$$y_i(t) = \sum_{j=1}^{2} A_{ij} G(t, \lambda_j) \qquad \text{(A6.9)}$$

In Eq. (A6.9), $G(t,\lambda_i)$ is the transfer function expressed as

$$G(t, \lambda_i) = \lambda_i \exp(-\lambda_i t) \int_0^t \exp(\lambda_i \theta)\ \mathrm{f}(\theta)\ d\theta \qquad \text{(A6.10)}$$

In Eq. (A6.10), the forcing function $\mathrm{f}(t) = \exp(-t/\tau_E^*)$ is expressed by the characteristic time constant τ_E^* of exponentially decaying electric field, see Eq. (2) of the main text. In Eq. (A6.9), the amplitudes A_{ij} are given by: [47]

$$A_{ij} = \left\{ \prod_{p \neq j} (\lambda_p - \lambda_j) \right\}^{-1} \sum_{q=1}^{n} (-1)^{i+q} \left| M_{i,q}(\lambda_j) \right| \bar{y}_q \,, \qquad \text{(A6.11)}$$

where $|M_{iq}(\lambda_j)|$ is the minor of the determinant $|a_{kl} - \lambda_j \delta_{kl}|$ with respect to the i, q – element and $\bar{y}_q$ is the time independent amplitude. The result for $y_2 (\equiv x_1)$ is:

$$\begin{aligned} y_2(t) = {} & \bar{\mu}_1 \frac{\tau_1 \tau_2}{\tau_1 - \tau_2} \frac{\tau_E^*}{\tau_E^* - \tau_1} \left(e^{-t/\tau_E^*} - e^{-t/\tau_1} \right) + \\ & + \bar{\mu}_2 \frac{\tau_1 \tau_2}{\tau_2 - \tau_1} \frac{\tau_E^*}{\tau_E^* - \tau_2} \left(e^{-t/\tau_E^*} - e^{-t/\tau_2} \right) \end{aligned} \qquad \text{(A6.12)}$$

where $\bar{\mu}_i = \bar{y}_2 (a_{11} - 1/\tau_i) - \bar{y}_1 a_{12}$ $(i = 1; 2)$. Since at (higher) electric fields, certainly $[C_1] >> [C]$, thus $K_0 = [C_1]/[C] >> 1$ and the approximation $k'_{12} = k_{12} K_0 /(1 - K_0) \approx -k_{12}$ is justified. Additionally, the data analysis indicates that $K_1 >> 1$, thus the inequality $k_1 >> k_{-1}$ can be used. Hence, $a_{11} = k_{12} + k_{21} + k_1 \approx (k_{12} + k_{21}) + (k_1 + k_{-1}) = 1/\tau_1 + 1/\tau_2$. Because $\bar{y}_1 \equiv \bar{x}_3 = 0$, the amplitude terms are $\bar{\mu}_1 = \bar{y}_2 / \tau_2$ and $\bar{\mu}_2 = \bar{y}_2 / \tau_1$. Substitution into Eq. (A6.12), and recalling that $y_2(t) \equiv x_1(t)$, yields:

$$x_1(t) = \bar{x}_1 \left[\frac{\tau_C \tau_E^* \left(e^{-t/\tau_E^*} - e^{-t/\tau_C} \right)}{\left(\tau_C - \tau_1 \right)\left(\tau_E^* - \tau_C \right)} + \frac{\tau_1 \tau_E^* \left(e^{-t/\tau_E^*} - e^{-t/\tau_1} \right)}{\left(\tau_1 - \tau_C \right)\left(\tau_E^* - \tau_1 \right)} \right], \qquad \text{(A6.13)}$$

where $\bar{x}_1$ is the amplitude, $1/\tau_c = k_{12} + k_{21}$ and $1/\tau_1 = k_1 + k_{-1}$ are intrinsic relaxation times of the first reaction cascade.

Appendix 7: Membrane curvature.

The electroporation parameters of large vesicles (a = 10 μm) and of moderately small vesicles (a = 90 nm) are very similar with respect to curvature. The membrane curvature, $C = 1/a$, is classified as small, if the corresponding radius a (of vesicle or cell) is much larger than the membrane thickness $d_m = 5$ nm.[17-18] Explicit, if $a >> d_m$, we have $d_m/a = d_m C << 1$. For our moderatelly small vesicles, the inequality $d_m/a = 0.055 << 1$ holds true. Hence, we may consider the curvature of these small vesicles as small. Therefore, the very curvature effects are comparable for small and for large vesicles or cells.

Appendix 8: The dielectric constant of pore water

In analogy to the observations of Sansom et. al.,[48] who investigated the dielectric properties of water within model transbilayer pores, the dielectric coefficient ε_{Pi} of water within the Pi pores depends on the local field $E_{P,local} = E_m - E_l$; E_m is the membrane field (which is related to the external field E by Eq. (26) of the main text) and E_l is the field induced by the oriented dipoles of the lipid head groups, see Fig. 9(c). For small external fields, $E_m << E_l$, thus $E_{P,local} \approx - E_l$, and the water molecules are nearly oriented antiparallel to the external electric field. In this case, the polarization of water molecules is nearly saturated because of the electric field from the tilted lipids. Thus at "low" E_m, up to $E_m \approx E_l$, the approximation $\varepsilon_P \approx 8$ applies. For the case $E_m \geq E_l$, the approximation $\varepsilon_P \approx \varepsilon_W = 78$ holds true. If we take the mean value of 20 D for the dipole moment of phosphatidyl choline head group,[49] and assume the tilting angle of the lipid heads $\Delta\theta = 20°$ (see Fig. 9(a)), E_l is calculated numerically by solving Poisson's equation for the three dimensional case of the torus-hole pore model (Fig. 9(b)). Additional parameters used for the calculation are: the projected membrane surface area of one lipid head group is on average 0.65 nm^2, $\varepsilon_W = 78$ and $\varepsilon_P = 8$ (at $E_m \to 0$). 48 For P_1 and P_2 pores of mean inner radius $r_1 = 0.4$ nm and $r_2 = 1.7$ nm, respectively, we obtain $E_{l,P1} \approx 300$ kV/cm and $E_{l,P2} \approx 200$ kV/cm. These values are much smaller than the induced transmembrane fields E_m in our experiment, e.g, $E_m >$ 2700 kV/cm at $E >$ 10 kV/cm. Hence, the inequality $E_m \geq E_l$ holds true and the approximation $\varepsilon_P \approx \varepsilon_W = 78$ is justified; see the text below Eq. (24).

Notes and references

[a] *Department of Chemistry, Biophysical Chemistry*
Bielefeld University
Universitaetsstr. 25, D-33615 Bielefeld, Germany
Phone: (+49)521-1062064
Fax: (+49)521-1062981
E-mail: sergej.kakorin@uni-bielefeld.de

† Electronic Supplementary Information (ESI) available: [details of any supplementary information available should be included here]. See DOI: 10.1039/b000000x/

1 E. Neumann, M. Schaefer-Ridder, Y. Wang and P. H. Hofschneider, *EMBO J.*, 1982, **1**, 841.
2 T. K. Wong and E. Neumann, *Biophys. Biochem. Res. Commun.*, 1982, **107**, 584.
3 L. M. Mir, S. Orlowski, J. Jr. Belehradek, J. Teissie, M. R. Rols, G. Serša, D. Miklavcic, R. Gilbert and R. Heller, *Bioelectrochem. Bioenerg.*, 1995, **38**, 203.
4 L. Mir, O. Tounekti and S. Orlowski, *Gen. Pharmac*., 1996, **27**, 745.
5 R. Heller, M. Jaroszeski, L. Glass, J. Messina, D. Rapaport, R. DeConti, N. Fenske, R. Gilbert, L. Mir and D. Reintgen, *Cancer*, 1996, **77**, 964.
6 F.M. André, J. Gehl, G. Sersa, et al., *Human Gene Therapy*, 2008, **19**, 1261.
7 E. Neumann and K. Rosenheck, *J. Membr. Biol*., 1972, **10**, 279.
8 E. Neumann, G. Gerisch and K. Opatz, *Naturwissenschaften*, 1980, **67**, 414.
9 I. G. Abidor, V. B. Arakelyan, L. V. Chernomordik, Y. A. Chizmadzhev, V. P. Pastuchenko and M. R. Tarasevich, *Bioelectrochem. Bioenerg*., 1979, **6**, 37.
10 J. Weaver and Yu. Chizmadzhev, *Bioelectrochem. Bioenerg.*, 1996, **41**, 135.
11 R. Dimova, K. A. Riske, S. Aranda, N. Bezlyepkina, R. L. Knorr and R. Lipowsky, *Soft Mater*, 2007, **3**, 817.
12 K. A. Riske, R. Dimova, *Biophys J*., 2005, **88**,1143.
13 K. A. Riske, R. Dimova, *Biophys J*., 2006, **91**, 1778.
14 P. M. Vlahovska, R. S. Gracia, S. Aranda-Espinoza, R. Dimova, *Biophys J*. 2009, **96**, 4789.
15 T. Yamamoto T, S. Aranda-Espinoza, R. Dimova, R. Lipowsky, *Langmuir*. 2010, **26**, 12390.
16 K. Kinosita and T. Y. Tsong, *Biochim Biophys. Acta*, 1977, **471**, 227.
17 W. Helfrich, *Z. Naturforsc. [C]*, 1973, **28**, 693.
18 J. Zimmerberg and M. Kozlov, *Nature Rev. Mol. Biol*., 2006, **7**, 9.
19 E. Neumann and S. Kakorin, *Curr. Opin. Coll. Int. Sci.*, 1996, **1**, 790.
20 S. Kakorin, E. Redeker and E. Neumann, *Eur. Biophys. J*.,1998, **27**,43.
21 K. Tönsing, S. Kakorin, E. Neumann, S. Liemann and R. Huber, *Eur. Biophys. J.*, 1997, **26**,307.
22 T. Griese, S. Kakorin and E. Neumann, *Phys. Chem. Chem. Phys.*, 2002, **4**, 1217.
23 M. Schmeer, T. Seipp, U. Pliquet, S. Kakorin and E. Neumann, *Phys. Chem. Chem. Phys.*, 2004, **6**, 5564.
24 I. P. Sugar, *J. Physiol. Paris*, 1981, **77**, 1035.
25 I. P. Sugar and E. Neumann, *Biophys. Chem.*, 1984, **19**, 211.
26 T. Portet, R. Dimova, *Biophys J*., 2010, **99**, 3264.
27 V. G. Farafonov, V. Voshinnikov and V. V. Somsikov, *Appl. Opt.*, 1996, **35**, 5412.
28 G. Sersa, D. Miklavcic, M. Gemazar, Jr. Beleradek, T. Jarm and L. Mir, *Bioelectrochem. Bioenerg.*, 1997, **43**, 279.
29 M. Eigen and L. DeMaeyer, in *Technique of Organic Chemistry*, 2nd edn., Vol. 8, Part 2.
30 S. Kakorin and E. Neumann, *Ber. Bunsenges. Phys. Chem.*, 1996, **100**, 721.
31 S. Kakorin and E. Neumann, *Coll. Surf. A.*, 2002, **209**, 147.
32 E. Neumann, S. Kakorin and K. Toensing, *Faraday Discuss.*, 1998, **111**, 111.
33 A. Revzin and E. Neumann, *Biophys. Chem.*, 1974, **2**, 144.
34 H. P. Schwan, *Adv. Biol. Med. Phys.* 1957, **5**, 147-209.
35 H. Leontiadis, A. E. Mark and S.-J. Marrink, *Biophys. J*., 2007, 92, 4209-4215.
36 R. A. Böckmann, B. L. de Groot, S. Kakorin, E. Neumann and H. Grubmüller, *Biophys. J*., 2008, 95, 1837-1850.
37 H. Fricke, *J. Appl. Phys*., 1953, **24**, 644.
38 E. Neumann, in *Electroporation and Electrofusion in Cell Biology*, ed. E. Neumann, A. E. Sowers and C. Jordan, Plenum Press, New York, 1989, pp. 61.
39 S. Kakorin, T. Liese and E. Neumann, *J. Phys. Chem. B*, 2003, **107**, 10243.
40 S. Zeks and S. Svetina, in *The Structure and conformation of amphiphilic membranes*, ed. R. Lipovsky, D. Richter and K. Kremer, Spinger Proceedings in Physics, 1992, vol. **66**, p. 174.
41 S. Kakorin and E. Neumann, *Ber. Bunsen-Ges. Phys. Chem.*, 1998, **102**, 607.
42 S. Kakorin and E. Neumann, *Bioelectrochemistry*, 2002, **56**, 163.
43 Y. Jiang, H. Wang, and J. T. Kindt, *Biophys J*., 2010, **98**, 2895.
44 E. Tekle, R. D. Astumian, W. A. Friauf and P. B. Chock, *Biophys. J*., 2001, **81**, 960.
45 D. C. Chang, in *Guide to Electroporation and Electrofusion*, ed. D. C. Chang, B. M. Chassy, J. A. Saunder and A. E. Sowers, Academic Press, 1992, pp. 9.
46 U. Pliquett , R. P. Joshi, V. Sridhara, K. H. Schoenbach, *Bioelectrochemistry*, 2007, **70**(2), 275.
47 Tamura and Z. A. Schelly, *Adv. Mol. Relax. Interact. Processes*, 1982, **24**, 259-269.
48 M. S. P. Sansom, G. R. Smith, C. Adcock and P. C. Biggin, Biophys. J., 1997, **73**, 2404.
49 K. Gawrisch, D. Ruston, J. Zimmerberg, V. A. Parsegian, R. P. Rand, and N. Fuller, *Biophys. J*., 1992, **61**, 1213.

Part II

Polarization and Aggregation of *Polystyrene Latex* Particles and *S. Pombe* Yeast Cells in External Electric Fields

Abstract

In a.c. electric fields, diluted suspensions of *S. pombe* yeast cells and smaller polystyrene latex particles of radius a = 400 nm exhibit various pattern of particle aggregations. In the frequency range $3 \leq f / \mathrm{Hz} \leq 3000$, the particular field-induced associations of the latex particles around the cells change from accumulation near the pole-caps facing the electrodes to accumulation near the equator of the yeast cells. The frequency of transition ranges depends on the ionic strength of the suspending medium, conductivity range (10^{-5} – 10^{-4} S m^{-1}). The low frequency behavior is described in terms of ion-flow polarization of the ionic double layers associated with the charged particles. The yeast cell interaction with the latex particles is rationalized in terms of induced-dipole forces.

The analysis of the data yields the electro-kinetic parameters of the yeast cells and the latex particles in 0.1 mM NaCl solution. The resulting ζ-potentials are: ζ_p = –76 (± 4) mV for the latex particles and ζ_c = –57 (± 4) mV for the yeast cells. The surface-conductivities K^{σ} of the latex particles and the yeast cells are characterized in terms of the ratio $\Theta = K^{\sigma i} / K^{\sigma d}$ between the surface-conductivity $K^{\sigma i}$ inside the plane of shear and $K^{\sigma d}$ that outside the plane of shear (diffuse layer). For the latex particles, Θ_p = 0.56 (± 3). For the yeast cells, Θ_c = 27 (± 3), i.e. ca. 50 times higher. Thus, yeast cells exhibit a very much higher induced dipole moment as expected by the classical (diffuse) double layer polarization model, whereas the latex particles behave according to the classical model.

The newly developed flow-polarization model for the yeast cells incorporates the dominant polarization contribution of the inner layer (shell) and is analogous to the *Schwarz*-polarization model (of no net ion exchange between the larger inner shell and the diffuse outer ion layer). The large induced yeast cell polarization structurally resides in the thick polyionic glycocalix shell of high fixed charge density and corresponding large counterion concentrations.

1. Introduction

Among all cell-manipulation techniques, the membrane electroporation (ME) is widely used in Electrochemotherapy and Gene Electrotherapy to deliver macromolecules into cells. ME involves rapid changing of the cell membrane structure induced by an external electric field, [1], [2] make it porous and permeable, to allow uptake of DNA or RNA. Recently, gene (or drug) delivery methods based on small particles used as gene (drug) carriers have shown their potential on enhancing the delivery rate. Drug-loaded particles, such as liposomes micelles and polymeric particles also demonstrate a broad variety of useful properties.

When an electric field is applied to a colloid particle suspension, the particles in the suspension become polarized, acquiring an induced dipole moment (i.d.m.) directed parallel to the applied electric field. As a result, the particles attract each other in the direction of the i.d.m. to form pearl chains in the suspension. The association of biological cells in external electric field has been used to produce cell electro-fusion [3] by electroporation.[1] On the other hand, in suspensions with two different types of particles there is not always pearl chain formation parallel to the field lines. For instance, mixture of polystyrene and silica particles suspended in low conductive medium can develop structures near planar electrodes which changes morphology within the frequency range 1 Hz - 10 kHz.[4] Diluted mixtures of charged rod-like particles suspended in a 'sea' of smaller spherical particles having similar charge density, show 'anomalous' induced electric birefringence in the same (low) frequency range.[5] In mixtures of particles of two types, in a given frequency range of the applied field, the induced dipole moment of one of the type of the suspended particles may differs in sign from the other, leading to lateral (transverse to the field lines) separation and lateral chaining of the particles.[4], [6] Although the induced particle interaction and its sign change with frequency has been discussed in depth, less attention has been paid to the magnitude of the induced dipole. It is found that the induced particle dipole can be obtained, for instance, by electro-optical or (and) by dielectric spectroscopy. Electro-optical methods have been traditionally applied aiming at quantifying the polarizability of rod-like particles and DNA fragments from changes in the field induced orientation of the colloids.[9]-[11] Dielectric spectroscopy is probably the most useful technique to quantify the induced dipole moment of spherical colloids in very low a.c. electric fields.[12], [15]-[21] Both, the dielectric spectroscopy and electro-optics are particularly useful in the case of monodisperse particle solutions, but have serious

limitations when mixtures of particles of different types lead to complex dielectric dispersion and relaxation curves.

Therefore, here an optical microscope video-recording system is used to observe the dynamics of the peculiar field induced aggregation behaviour of polystyrene latex particles and yeast cells. The changes in the aggregates as a function of frequency were analysed by simulation techniques. The main electro-kinetic parameters of the latex particles and the yeast cells (ζ-potential and surface conductivity) are used as adjustable parameters. Applying different theoretical models of electric double layer (EDL) polarization, starting with the standard (diffuse) EDL-polarization model, the optimum values of the parameters have been obtained.

2. Materials and methods

The samples are of suspensions volume fraction $f_{V,latex} = V_{\text{latex}} / V_{\text{total}} = 0.01$ of polystyrene latex particles and ~0.002 volume fraction $f_{V,yeast} = 0.002$ of *S. pombe* yeast cells suspended in weak NaCl solution, varied in the concentration range 10^{-5} - 10^{-3} M. The polystyrene latex stock suspensions (Estapor© microspheres, ECS 080) were washed 4 times by repeated centrifugation. After each centrifugation the supernatant was discarded and the particles resuspended in the bidistilled water. A final centrifugation/decantation in 0.1 - 10 mM NaCl was used to prepare the particles for experimentation. The culture of *Schizosaccharomyces pombe* (*S. pombe*) 972h$^-$ was propagated in YED (yeast extract 1%, glucose 2%) in Erlenmeyer flasks at 250 rpm and 24°C. The cells were killed by autoclaving at 120°C, washed 4 times in doubly-distilled water followed by final washing with NaCl solution of desired concentrations. The so prepared particle (cell) dispersions were mixed to become suspensions with a given ionic strengths of the medium.

The sample cell, as illustrated in Fig. 1, was made of two microscope glass slides separated at a distance of about 200 μm by spacers prepared from micro cover glasses (thickness 170-250 μm). The electrodes are made of two platinum wires (150 μm diameter) spaced 5 mm apart. Homemade amplifier, capable of delivering voltages of up to 400 V in the range from d.c. to 1 MHz, supplied an alternating voltage across the electrodes. The construction of the sample cell allows flow as in a open type electrophoretic chamber.

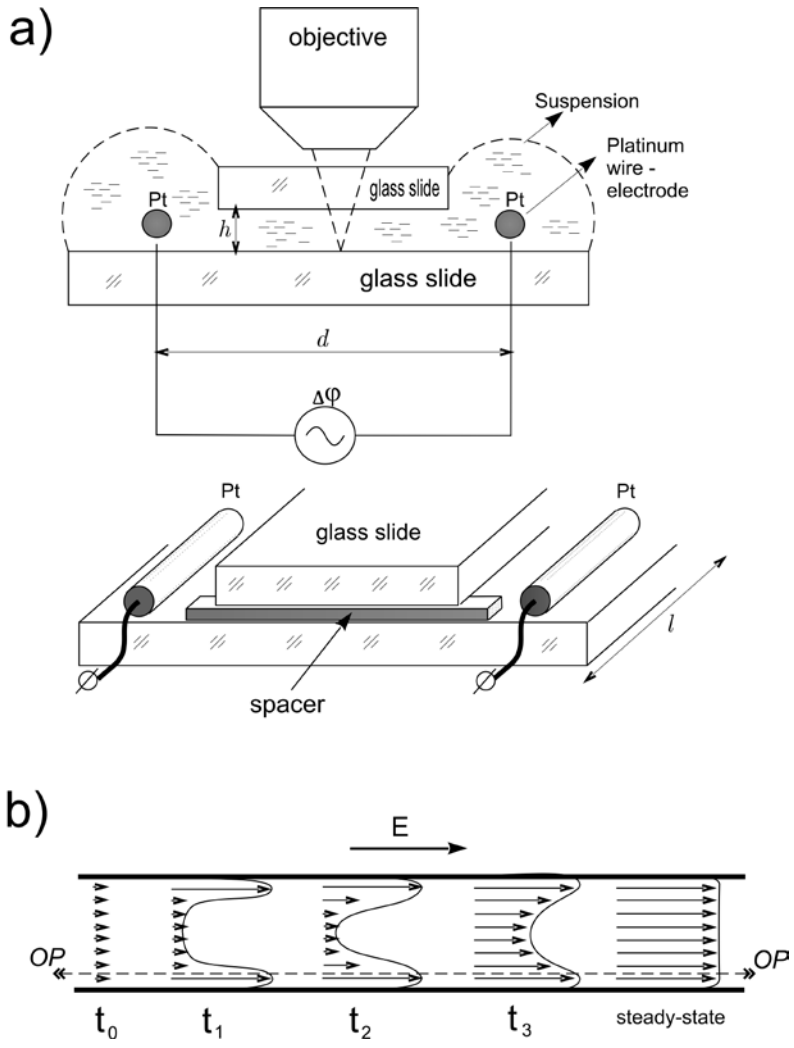

Fig. 1 Schematic illustrations of the sample cell prepared (a) and the time evolution of the electro-osmotic flow velocity profile (b) from switching on of an external d.c. electric field E (at t_0 - left) to fully developed flow (right). The dashed line (*OP*) indicates the observation plane. Diagrams not to scale. ($h \approx 200$ μm; $d = 5$ mm; $l \approx 10$ mm)

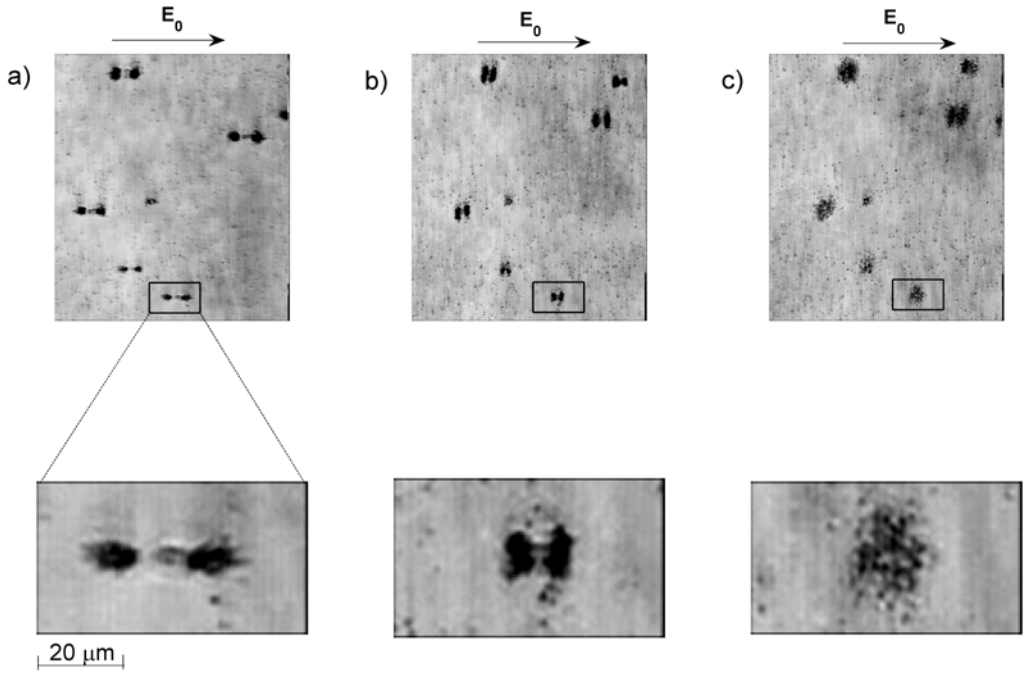

Fig. 2 Optical images of aggregates formed by accumulation of polystyrene latex particles around *S. pombe* yeast cells under action of electric field at different frequencies: f = 4 Hz (a), f = 30 Hz (b), and f = 3 kHz (c). The particles, radius a_p = 400 nm, can be seen as dark 'cloud'-like bands around the cells - the prolate ellipsoid in the middle of the dark 'clouds'. Suspending medium: 10^{-4} M NaCl. The external electric field, $\mathbf{E} = \mathbf{E_0} \cos(2\pi \cdot f \cdot t)$ with amplitude $E_0 = (10 - 60) \times 10^3$ V m^{-1} is applied in the horizontal direction.

3. Experimental results

Fig. 2 shows typical responses of the yeast cells / polystyrene latex particles mixture in the frequency range $3 \leq f$ / Hz ≤ 3000 of the external a.c. electric field. The yeast cells can be seen in the middle of the clouds of particles as a prolate ellipsoid of revolution. In the frequency range $3 \leq f$ / Hz ≤ 3000, the biological cells remain oriented with its longest axis parallel to the external field lines whereas the particles change its position depending on the frequency. At frequency below 100 Hz the particles accumulate on the 'pole-capes' (the ends of the field-oriented prolate cell body). At frequency above 500 Hz the particles tend to accumulate on the 'equator' of the prolate *S. pombe* yeast cell. In the latter configuration the particles cover the cells and therefore they remain under the plane of observation (Fig. 2(c)). In addition to the optical microscopy observations, electrooptical turbidity relaxation spectroscopy has been used (unpublished results) to analyse the orientation of the *S. pombe* yeast cells at different salt concentrations in suspension without and with particles.

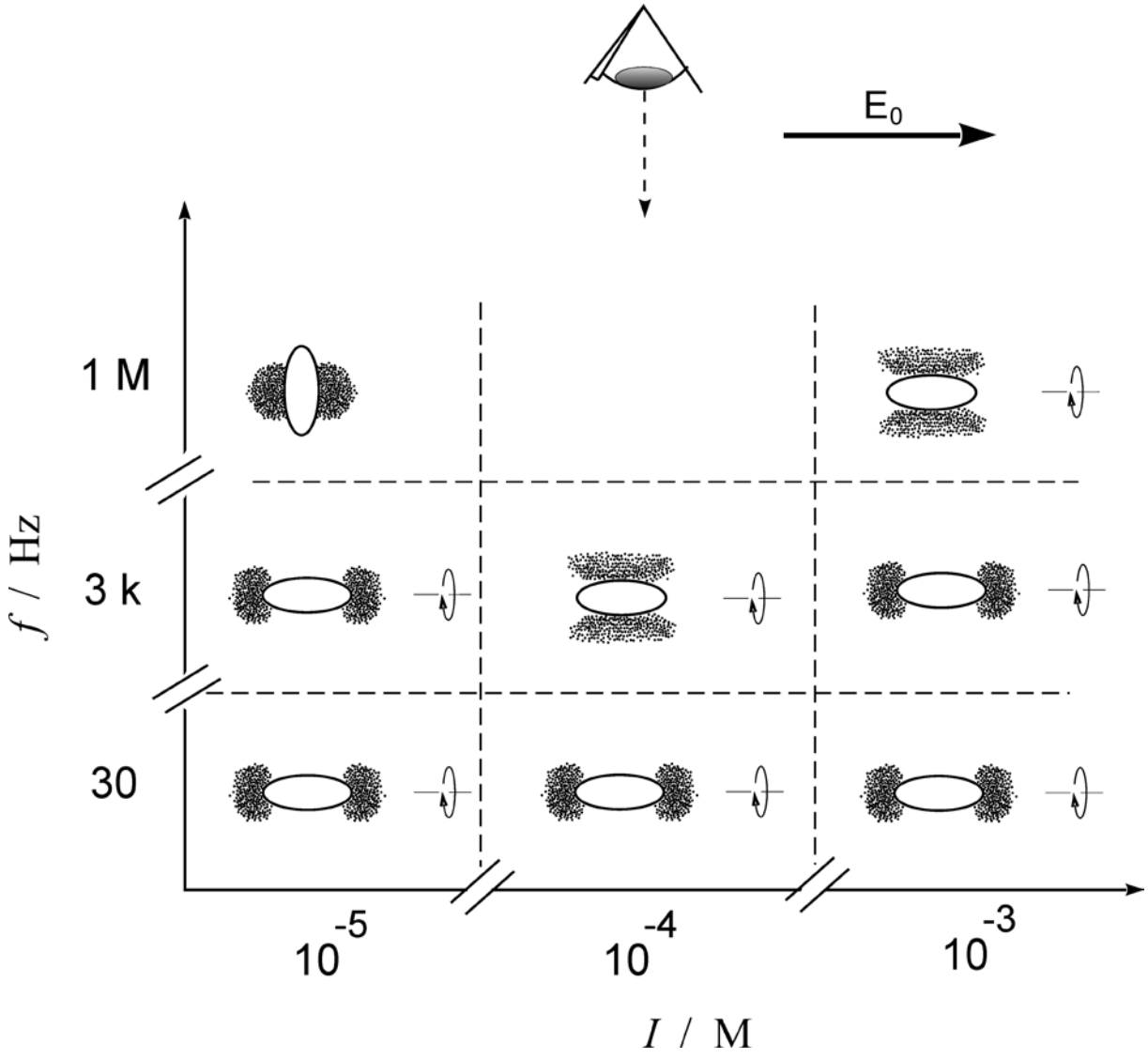

Fig. 3 Diagrammatic representation of the patterns formed by accumulation of polystyrene latex particles (black dots) around S. *pombe* yeast cell (the prolate ellipsoids) under action of an a.c. electric field. The position of the particles depends on both, the ionic strength *I* of the suspending medium (NaCl) and the frequency *f* of the applied field. Diagrams not to scale.
The circle-arrows on the right-hand side of the pictures denote rotational symmetry (if any exists).

The transition 'pole-caps' - 'equator' accumulation depends on the frequency and the conductivity of the solvent. Schematic representation of this dependence is given in Fig. 3. In the frequency range f = 1 Hz - 700 kHz, the yeast cells orientate with its longest axis parallel to the external field lines. The parallel orientation is not affected by the presence of the smaller latex particles. When the frequency exceeds 700 kHz, the yeast cells orient perpendicular to the field lines. The orientation modes can be consistently analysed in terms

of the Maxwell-Wagner (MW) polarization of yeast cell.[7], [8] However, in the kHz range the yeast cell membrane appears non conductive and completely polarized. In this state, the yeast cell can be treated as a pure dielelectric particle. In this case, according to MW polarization, the induced dipole moment of the yeast cell should not change sign at different medium conductivities and frequencies. It is the electric double layer (EDL) polarization that depends on the ionic strength of the solution. Therefore, the EDL-polarization of the biological cells (particles) should be taken into account by the quantification of the low-frequency aggregates.

4. Theory and analysis

4.1 Polarization mechanisms

When biological cells are manipulated by externally applied electric fields, weak electrolytes as a dispersion medium are preferred (minimizing Joule heating). Comonly, the calculation of the induced trans-membrane voltage (or the induced dipole moment of a biological cell) refers to the Maxwell–Wagner (MW) polarization mechanism. [13], [14] The MW analysis operates with the different conductivities or (for dielectric system) the different dielectric permittivities of the membrane/medium interfaces. In these approaches, usually the charges of various membrane components as the glycocalyx layer and the hydrophilic head groups of the lipid molecules are treated separately.[22], [23] The MW theoretical treatment is based on the assumption, that the conductivity of the electrolyte solution close to the cell surface has the same value as far away from the cell. In general this assumption is satisfied for cells in aqueous electrolytes under physiological conditions, but it is not fulfilled for cells of net surface charge suspended in a low conductive medium. As known for (charged) colloid particles, charged membrane surfaces attract oppositely charged ions forming a layer of counter ions. So, the higher ion density near the cell surface results in a much higher surface layer conductance than that of the bulk electrolyte. Thus, the fixed membrane charges contribute indirectly to the surface conductivity of the suspended cell and additionally modify the electric filed distribution around the cell body.

O'Konsky[24] first introduced a constant (integral) linear *surface-conductivity* K^{σ} (in utin S), defined via a two-dimensional Ohm's law for the (linear) *surface current density* (in A m^{-1}) $j^{\sigma} = K^{\sigma}E$ where E is the tangential component of the field. The *surface-conductivity* K^{σ} is an excess quantity which can be derived as the difference between the total conductivity of a

disperse system and the same in the absence of double layer. K^{σ} is a frequency-independent quantity which refers to ions flowing from one side of the spherical surface to the other. For a charged particle suspended in electrolyte solution with bulk conductivity K_e (S m^{-1}), EDL-polarization is finite only if $2K^{\sigma}/a > K_e$, where a is the radius of the particle. The outer surface of the conducting shell represents a boundary surface for the ionic Maxwell-Wagner polarization. The *surface-conductivity* K^{σ} of spherical particle with radius a is treated as a part of the total conductivity of the particle $K_p^{total} = K_p + 2K^{\sigma}/a$, where K_p is the conductivity of the particle.[24] A dielectric particle is qualified by $K_p = 0$ and the total particle conductivity is solely proportional to the surface conductivity $K_p^{total} = 2K^{\sigma}/a$.

In Fig. 4, the role of *surface-conductivity* for the induction of the dipole moment of the *S. pombe* yeast cells is illustrated (Maxwell-Wagner-O'Konsky (MWO) model). The shape of the yeast cell is approximated by prolate ellipsoid. The external field is applied along the longest axis of the cell. The electric potential distribution is calculated by solving the continuity equation for the two-dimensional case, $\nabla\cdot(K\,\nabla\varphi) = 0$, where the conductivity K is a known scalar field $K = K(x, y)$ and the electric potential $\varphi = \varphi(x, y)$ is the solution of the Laplace equation (also scalar field). The conductivity $K(x, y)$ is taken to be constant in each of the four regions: bulk electrolyte, double layer shell, cell membrane and the cell core, respectively. The external field intensity, which is given by $E_0 = -\nabla\varphi\,(x\to\infty, y\to\infty)$, is a known parameter. The integration is performed numerically using self-written source code (Matlab, finite element method). It can be seen that for a typical surface-conductivity of $K^{\sigma} = 2 \times 10^{-9}$ S, the induced transmembrane voltage $U_m = E_m/d_m$ is double-reduced compared to the case without surface conductivity. The induced MW-dipole moment of the cell is opposite to the external field vector $\mathbf{E_0}$ (counts negative for cell without surface conductance and no surface charges), Fig. 4(a). Counterion polarization leads to positive induced moment (counterion polarization of charged surface), Fig. 4(b).

The O'Konsky model disallows ion exchange between the conductive surface layer and the bulk electrolyte solution. For suspensions of charged spherical dielectric particles of radius a, the O'Konski theory provides expressions for the measured dielectric permittivity $\varepsilon_r(\omega)$ and the relaxation time τ, which are formally equivalent to those of the Maxwell-Wagner (MW) polarization. In the Maxwell-Wagner-O'Konsky (MWO) model the core conductivity of the particles K_p is replaced by $(K_p + 2K^{\sigma}/a)$. O'Konski describes $\varepsilon_r(\omega)$ near the characteristic frequency of MW, but offers no satisfactory interpretation for the high values of the static

permmitivity $\varepsilon_{r.}(0)$, and the relaxation time τ found in suspensions at frequencies below several kHz.[12] Later, Schwarz[15] attributed the low-frequency relaxation to EDL-polarization of entirely "bound" counterions (no net ion exchange with the bulk solution), i.e. , the charge conservation conditions contains no normal net flows (see Fig. 5(a)).

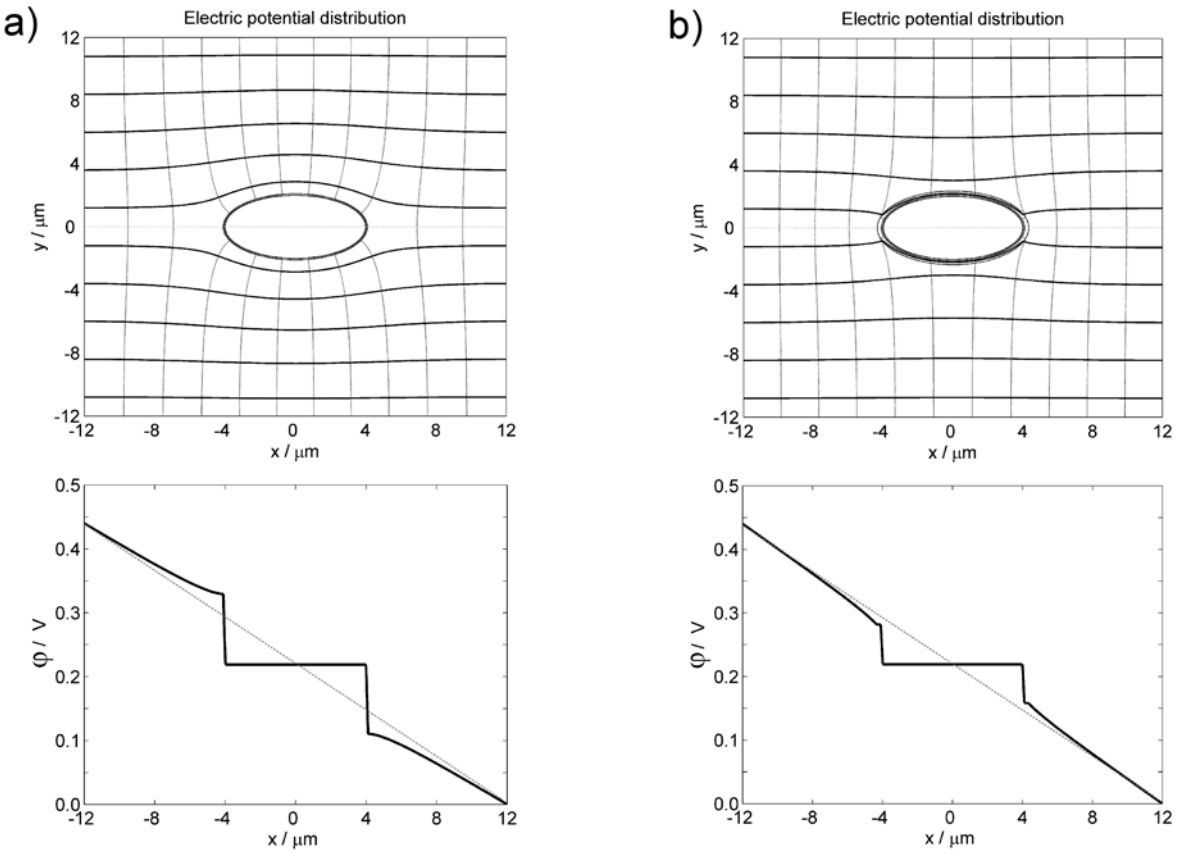

Fig. 4 The electric potential distribution around a yeast cell in uniform electric field (*x*-direction) in case of (a) uncharged membrane surface (Maxwell-Wagner polarization) and (b) charged membrane surface (Maxwell-Wagner-O'Konski model). The equipotential curves (vertical lines of the grid) and electric field lines (-horizontal) are calculated numerically by solving the Laplace's equation in two dimensional case with parameters: Electric field intensity E_0 = 180 V cm^{-1}; external medium conductivity $K_e = 14 \times 10^{-4}$ S m^{-1} ($\approx 10^{-4}$ M NaCl); cell interior conductivity K_i = 1 S m^{-1}; dielectric constants of the outer and inner cell medium $\varepsilon_e = \varepsilon_{in} = 78$, and that of the cell-membrane $\varepsilon_m = 2$; surface-conductivity of the cell $K^\sigma = 2.4 \times 10^{-9}$ S. The sloping dotted lines in the bottom of the figures show the potential profile $\varphi(x)$ in the electrolyte solution without cell. The bold line in the same figures is the potential $\varphi(x)$ in the presence of the yeast cell. The vertical drops in the potential profile $\varphi(x)$ around the pole caps of the yeast cell (solid curves at the bottom of the figures) correspond potential drop across the membrane.

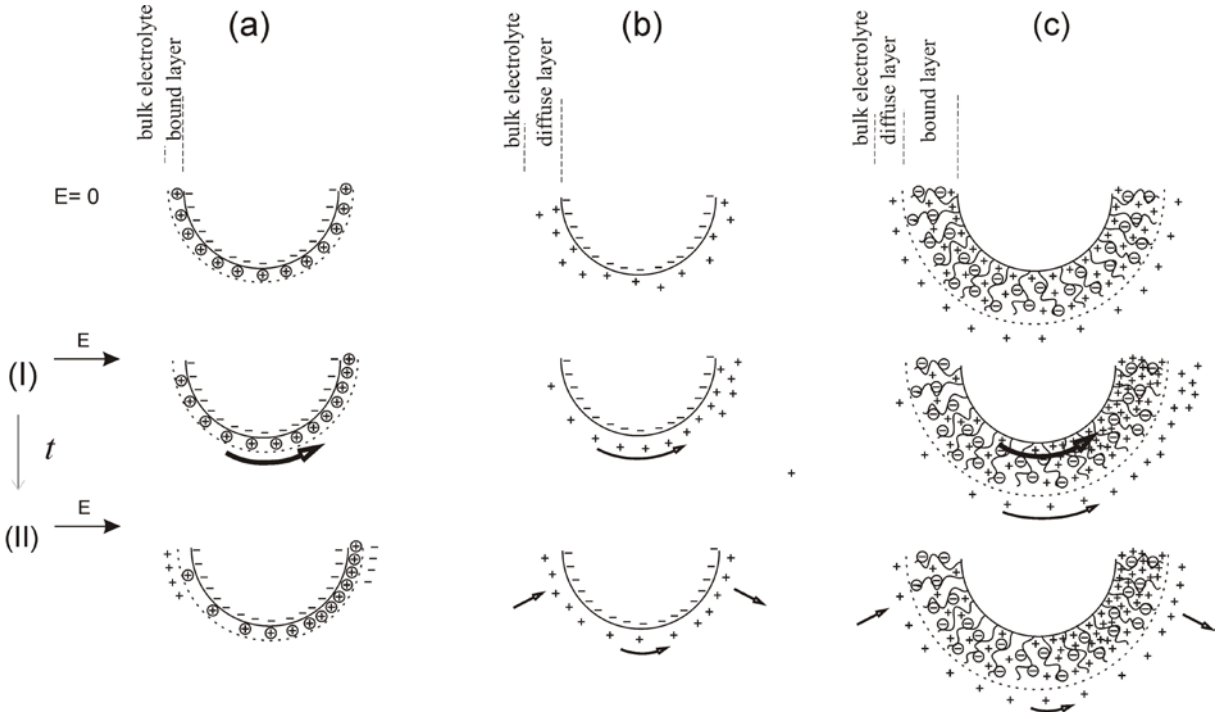

Fig. 5 Schematic representation of the polarization models discussed: (a) The *Schwarz* model - no counterion exchange between the bulk and the double layer; (b) The *diffuse double layer* polarization model (classical model) - ion exchange between the double layer and the bulk is allowed; (c) The here proposed polyionic glycocalyx polarization model that describes the polarization of the yeast cells: the bound ions (cyrcles) can move laterally but no net exchange with the diffuse ions.
The arrows on the particle surface denote the amplitude of the surface current I_S. Thin double layer is considered ($\kappa a >> 1$). The spherical dielectric particle is negatively charged. The time evolution of the polarization (under d.c. field) is shown in two steps: (I) $\tau^{\gamma} < t < \tau^{\alpha}$ and (II) $t > \tau^{\alpha}$, where $\tau^{\gamma} = (\kappa^{-1})^2 / D$ is the high-frequency γ-relaxation (or MWO-relaxation) time and $\tau^{\alpha} = a^2 / 2D$ is the low-frequency α-relaxation time, with D being the diffusion coefficient of the ions. Diagrams not to scale.

The tightly bound double layer in the Schwarz model was later abandoned in favour of Gouy-Chapman type models, dealing principally with the *diffuse* double layer. The characteristic thickness of the diffuse double layer is the Debye screening length κ^{-1}, where κ is the Debye – Hückel parameter given by:

$$\kappa = \left(2000 \frac{F^2 I}{\varepsilon_0 \varepsilon_e RT} \right)^{1/2}, \qquad (1)$$

where $I = (1/2)\cdot\Sigma_i z_i^2 c_i$ is the ionic strength of the electrolyte solution; z_i is the charge number (with singn) and c_i /M is the molar concentration. In the light of the Gouy-Chapman model, in the presence of an applied electric field, the governing equations that have to be considered are the Poisson and Boltzmann equations for the potential and ion distribution, respectively, the ion conservation equations together with the Nernst-Plank equation for the ion fluxes, and in certain cases the Navier-Stokes equation for the fluid flow. These coupled nonlinear electrokinetic equations do not have analytical solutions. However, the equations can be linearized provided the applied electric field strength is not too high compared to the field of the fixed surface charges. Analytical solutions for particles with large κa (thin double layer approximation) in symmetrical electrolytes have been derived by number of authors.[18]-[20] More general numerical solutions are also available.[21]

The polarization of a spherical dielectric particle, in principal, is completely determined by the surface-conductivity K^σ, the particle size and the ionic composition of the suspending electrolyte. The latter two are known from the experiment under consideration. The surface-conductivity K^σ is accounted for through the dimensionless *Dukhin* number *Du*,[25] which is given by the surface-to-bulk conductivity ratio: $Du \equiv K^\sigma / aK_e$. Although, in principle, *Du* can range from 0 to $+\infty$, in practice *Du* is of the order of 10^{-2} - 10^2 (for very low *Du* surface conduction can be ignored). For further analysis, it is convenient to distinguished between the surface-conductivity $K^{\sigma d}$ of the outer (diffuse) double layer and $K^{\sigma i}$ of the inner (Stern) double layer, using the relationship $K^\sigma = K^{\sigma d} + K^{\sigma i}$. $K^{\sigma d}$ consist of two parts: a migration contribution (movement of charges in respect to the liquid) and convective contribution (electro-osmotic liquid flow). Since $K^{\sigma d}$ can be expressed by the ζ-potential (through *Bikerman's equation), Du* (and thus the induced dipole moment of a particle) is expressed by ζ and the ratio $\Theta = K^{\sigma i}/K^{\sigma d}$ as a two parameter function $Du(\zeta, \Theta)$. Hence, the interaction energy U_{pc} between a latex particle (*p*) and a *S. pombe* cell (*c*) is completely determined by $Du(\zeta_p, \Theta_p)$ and $Du(\zeta_c, \Theta_c)$, respectively. For simplicity, the elongated body of the *S. pombe* cell is approximated by a sphere with effective radius of $a_c^{eff} \approx 3$ μm, where $a_c^{eff} = (a_c \times b_c^2)^{1/3}$, a_c and b_c being the polar and equatorial radii of the cell.

4.2 Dipole coefficient

Considering the case of a sphere with radius a embedded in an electroneutral electrolyte solution under the influence of a uniform, parallel external field E directed along the positive x-axis, the electric potential distribution $\varphi_e(\mathbf{r})$ at any point $\mathbf{r}$ outside the electric double layer of the sphere located at the origin ($|\mathbf{r}| \geq a + \kappa^{-1}$) is given by solution of the Laplace's equation in the far field (beyond the double layer) as:

$$\varphi_e = -E\,r\cos\theta + C_p \frac{a^3}{r^2} E\cos\theta\,, \tag{2}$$

where r is the radial distance to the observation point, θ is angle between the field direction and the radius-vector $\mathbf{r}$. The first term in Eq. (2) is the potential of the homogeneous external electric field. The second term is the potential due to the induced dipole of the spherical particle characterized by the dimensionless *dipole coefficient* C_p (also known as the Clausius - Mossotti factor). Eq. (2) may also be formulated in terms of the induced dipole moment: [25]

$$\varphi_e = -Er\cos\theta + \frac{p_{ind}}{4\pi\varepsilon_0\varepsilon_e}\frac{\cos\theta}{r^2}, \tag{3}$$

where $p_{ind} = 4\pi\varepsilon_0\varepsilon_e \cdot a^3 \cdot Cp \cdot E$ is the induced dipole moment of the spherical particle and ε_e is the dielectric constant of the electrolyte solution.

4.3 Frequency dependence of the dipole coefficient

If the external field is harmonic function of time, $E(t) = E_0 \cdot \cos(\omega t)$, it is convenient to represent the time dependence of the field as $E^*(t) = E_0 \cdot \exp(i\omega t)$, where ω is the angular frequency and the asterisk denotes a complex quantity. For a simple (linear) medium, the charge density, polarization and other descriptive parameters will also be sinusoidal, but not necessary in phase with the field. The full electric response of the particle can be characterized by the complex particle conductivity $K_p^* = K_p + i\omega\varepsilon_0\varepsilon_p$, where ε_0 is the vacuum permittivity, K_p is the conductivity and ε_p is the dielectric constant of the particle. The corresponding complex permittivity ε_p^* is given by $\varepsilon_p^* = K_p^* / i\omega$.

Consequently, the induced dipole moment is not in phase with the field. Therefore, the dipole coefficient C_p of the particle (see Eq. (2)) is expressed by the complex quantity C_p^* =

$C_p' + iC_p''$, where C_p' and C_p'' are the real and the imaginary parts, respectively. For spherical dielectric particle and biological cell, the dipole coefficients are given by

$$C_p^*(\omega) = C_p^{*\alpha}(\omega) + \Delta C_p^{\gamma}\left(1 - \frac{1}{1 + i\omega\tau_p^{\gamma}}\right) \tag{4}$$

and

$$C_c^*(\omega) = C_c^{*\alpha}(\omega) + \Delta C_c^{\beta}\left(1 - \frac{1}{1 + i\omega\tau_c^{\beta}}\right) + \Delta C_c^{\gamma}\left(1 - \frac{1}{1 + i\omega\tau_c^{\gamma}}\right), \tag{5}$$

respectively (see Appendix 1). Hereafter, we shall use the subscript *p* and *c* denoting latex *particle* and yeast *cell*, respectively. In Eq. (4) and Eq. (5), the superscripts α, β, and γ denote the characteristic relaxation modes, here specified after Schwan's definition for the three relaxations observed in the dielectric dispersion spectrum of suspension of cells.[8] The amplitudes ΔC and the relaxation times τ of the corresponding β and γ modes, which depend on the electric properties of the particle/medium as well as on the surface-conductivity K^{σ} of the particles (cells), are expressed in Appendix 1.

Fig. 6 shows the theoretical dipole coefficient of the polystyrene latex particles and *S. pombe* cells as function of frequency for different values of *Du*, Eq. (4) and Eq. (5).

The γ- relaxation corresponds to the MW-relaxation (particle without surface conduction) and MWO-relaxation (surface conductive particle). Both, MW and MWO relaxations have characteristic relaxation times of the same order of magnitude. The MW dispersion occurs when the dispersed phases in contact have different conductivities and dielectric permittivities. If the ratio between these two quantities differs from the medium and the particle, i.e., if $(\varepsilon_e / K_e) \neq (\varepsilon_p / K_p)$, a formation of free ionic charges near the surface occurs. The finite time needed for this formation is of the order of $O(\varepsilon_e/K_e)$, which characterizes the time required for the screening of charge or electric field perturbations. The same order of magnitude corresponds to the time of ion diffusion through a distance l_D, equal to the Debye length, $O(l_D^2/D)$, where $l_D^2 = 1/\kappa^2 = D\varepsilon_e / K_e$, see Eq. (1). The γ-relaxation of the latex particles can be seen in Fig. 6 (b) at a frequency of about $f = 10^6$ Hz.

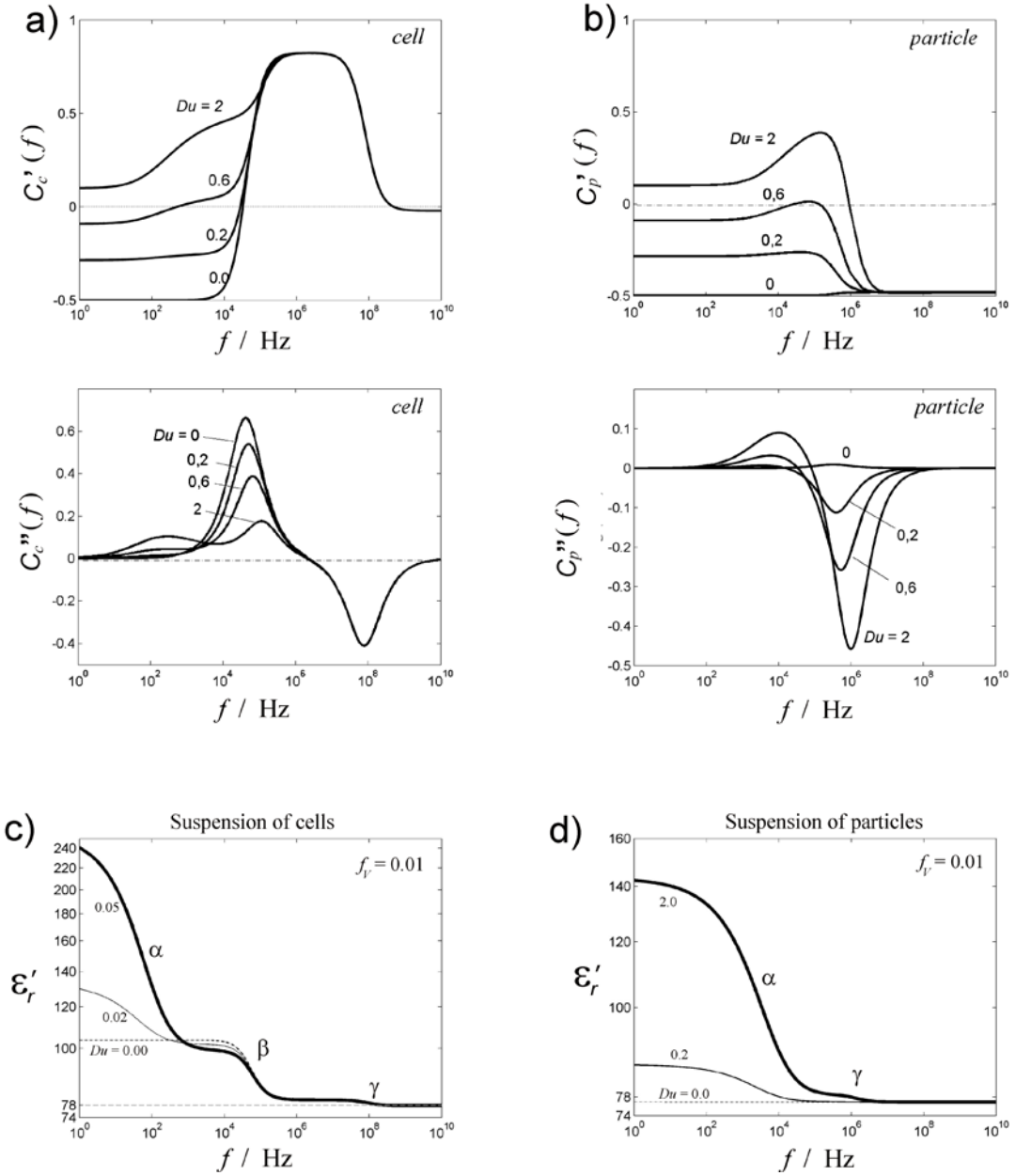

Fig. 6 The theoretical real $C'(2\pi f)$ (a) and the imaginary $C''(2\pi f)$ (b) parts of the dipolar coefficient $C^*(2\pi f) = C'(2\pi f) + iC''(2\pi f)$ of *S. pombe* yeast cell and polystyrene latex particle at different *Du* numbers ($Du = K^{\sigma} / aK_e$) as a function of the frequency f of the applied electric field calculated. (c) and (d): The real parts ε_r' of the dielectric constant $\varepsilon_r^* = \varepsilon_r' + i\varepsilon_r''$ of suspension of the yeast cells ((c)-left) and the latex particles ((c)-right), both at volume fraction $f_V = 0.01$, as a function of the frequency. $\varepsilon_r'(\omega)$ is calculated using the Maxwell's mixing formula $\varepsilon_r^* = \varepsilon_e^* \cdot (1+3f_V C^*)$, where ε_e^* is the complex dielectric permittivity of the suspending electrolyte. $C^*(\omega)$ is calculated using the classical (diffuse counterion cloud) polarization model, Eq. (6) and Eq. (12). The system parameters are: effective radius of the yeast cells $a_c^{\text{eff}} = 3$ μm; membrane thickness $d_m = 5 \times 10^{-9}$ m; cell-interior conductivity $K_i = 1$ S m^{-1}; membrane conductivity $K_m = 0$; dielectric constants of the outer and inner cell medium $\varepsilon_e = \varepsilon_{in} = 78$ and $\varepsilon_m = 2$ for the membrane; particle radius $a_p = 400$ nm; particle dielectric constant $\varepsilon_p = 2$; particle conductivity $K_p = 0$; ion diffusion coefficient $D^+ \approx D^- \equiv D = 2 \times 10^{-9}$ m^2 s^{-1} and medium conductivity $K_e = 20 \times 10^{-4}$ S m^{-1} .

The β-relaxation, usually found in the MHz range, is caused by the dielectric membrane properties of the cell. As can be seen by comparing Eq. (4) and Eq. (5), there is no β-relaxation in case of homogeneous dielectric particle. The β-relaxation (cell-model) is based on MW-polarization (or MWO in case of surface conduction) of the cell-membrane, whereas the γ-relaxation corresponds MW-polarization of the cell-core. For *S. pombe* yeast cells, the β- and γ-relaxation frequencies are $f_\alpha \approx 2 \times 10^5$ Hz and $f_\beta \approx 10^8$ Hz, respectively (see Fig. 6). The γ-relaxation of the yeast cells appears at higher frequency as that of the latex particles because the cell-core is high conductive ($K_i = 1$ S m^{-1}), whereas the conductivity of the particles is $K_p = 0$. In the case of nonconductive cell-core the γ-relaxation frequency is the same as that of the particles.

The α-relaxation. As mentioned above, in the kilohertz frequency range there is another high-amplitude dielectric dispersion caused by the polarization of the counterion layer of the suspended (charged) colloid particles. Analytical solutions for particles with large κa (thin double layer approximation) in symmetrical electrolytes have been derived by number of authors.[18]-[20] Here we use the analytical solution deduced by Lyklema, [25] with neglected contribution of the convection to the flow (particle radius much larger than the Debye screening length, $\kappa a >> 1$). The dipolar coefficient has a frequency dependence that does not correspond to a single time constant relaxation (being substantially broader): [26]

$$C^{*\alpha}(\omega) = -\frac{1}{2} + \frac{3Du}{2 + 2Du(\Gamma + 1)} \tag{6}$$

where

$$\Gamma = \frac{1 + \sqrt{\omega\tau^\alpha} + i\sqrt{\omega\tau^\alpha}}{1 + \sqrt{\omega\tau^\alpha} + i\sqrt{\omega\tau^\alpha} + i\omega\tau^\alpha} \tag{7}$$

$$Du = \frac{K^\sigma}{aK_e} \tag{8}$$

$$\tau^\alpha = \frac{a^2}{2D} \tag{9}$$

In Eq. (9), D is the diffusion coefficient of the ions in the solution. It is assumed that the diffusion coefficients of the positive and negative ions are approximately equal, $D_+ \approx D_- = D$.

4.4 Surface-conductivity

The dipole coefficient of a spherical (charged) dielectric particle is completely determined by the surface-conductivity K^{σ}, particle radius a and the Debye - Hückel parameter κ. The latter two parameters are known from the experiment under consideration. The surface conductivity K^{σ} has contributions owing to the diffuse-layer charge outside the plane of shear, $K^{\sigma d}$, and to the charge in the inner layer $K^{\sigma i}$: [25]

$$K^{\sigma} = K^{\sigma d} + K^{\sigma i} \tag{10}$$

Accordingly,

$$Du = \frac{K^{\sigma d}}{a K_e} + \frac{K^{\sigma i}}{a K_e} = Du^{d} + Du^{i} \tag{11}$$

The $K^{\sigma d}$ contribution is also called the *Bikerman surface conductivity* after Bikerman, who found a simple equation for $K^{\sigma d}$. In that case Du^{d} is expressed as:

$$Du^{d} = \frac{K^{\sigma d}}{aK_e} = \frac{2}{a\kappa}\left(1+\frac{3M}{z^2}\right)\left[\cosh\left(\frac{ze\varsigma}{2k_BT}\right)-1\right] \tag{12}$$

In Eq. (12), the parameter M indicates the relative contribution of electro-osmosis to the surface conductivity. For symmetrical electrolytes, M is given by:

$$M = \frac{2\varepsilon_0\varepsilon_e}{3\eta D}\left(\frac{k_BT}{e}\right)^2 \tag{13}$$

Substitution of Eq. (12) into Eq. (11) yields:

$$Du = \frac{2}{a\kappa}\left(1+\frac{3M}{z^2}\right)\left[\cosh\left(\frac{ze\zeta}{2k_BT}\right)-1\right]\left(1+\Theta\right), \tag{14}$$

where $\Theta = K^{\sigma i}/K^{\sigma d}$.

If we assume, as the experimental data suggest (see below), that the inner (Stern) double layer obeys a *Schwarz*-like polarization, that is, the surface conductivity of the inner layer is frequency dependent, we may substitute $K^{\sigma i}$ in Eq. (14) by:

$$K^{\sigma i} \equiv \frac{i\omega\tau^{\alpha i}}{1+i\omega\tau^{\alpha i}}K^{\sigma i} \tag{15}$$

Eq. (15) is essentially the surface-conductivity term in the Schwarz theory, with $\tau^{\alpha\,\mathrm{i}}$ being the characteristic relaxation time of the inner double layer. Substitution yields:

$$Du \equiv \frac{2}{a\kappa}\left(1+\frac{3M}{z^2}\right)\left[\cosh\left(\frac{ze\zeta}{2k_BT}\right)-1\right]\left(1+\frac{i\omega\tau^{\alpha\,\mathrm{i}}}{1+i\omega\tau^{\alpha\,\mathrm{i}}}\Theta\right) \tag{16}$$

In general, it is expected that the relaxation time of the inner counterion layer is larger than that of the diffuse layer, $\tau^{\alpha\,\mathrm{i}} > \tau^{\alpha\,\mathrm{d}}$. Here, for simplicity of calculation, we assume $\tau^{\alpha\,\mathrm{i}} \approx \tau^{\alpha\,\mathrm{d}} = a^2 / 2D$.

4.5 Induced dipole moment

The induced dipole moment of a spherical particle (or a biological cell) of radius a, p_{ind}^{*}, is expressed by the dipole coefficient C^{*} as:

$$p_{ind}^{*}\left(\omega, Du\right) = 4\pi\,\varepsilon_0\varepsilon_{\mathrm{e}}\,a^3\cdot C^{*}\left(\omega, Du\right)\cdot E^{*}(\omega) = \alpha^{*}(\omega, Du)\cdot E^{*}(\omega) \tag{17}$$

where $\alpha^{*} = \alpha^{*}(\omega, Du)$ denotes the electric polarizability of the particle. In Eq. (17), $Du = Du(\zeta, \Theta)$ depends on two parameters: the electrokinetic potential ς and the ratio Θ.

4.6 Simulation model

4.6.1 Simulation model specifics

The dynamics of the interaction between the latex particles and the yeast cells is simulated by two-dimensional model system of N identical particles and one yeast cell. The simulation is based on the analytical expressions for the particle-particle and particle-cell interaction energies. The model considers *induced dipole-induced dipole* interaction between particle i and j ($i, j = 1\ldots N$; $i \neq j$), as well as, between particle i and yeast cell c, see Fig. 8. The interaction energy depends on the induced dipole moments of the particles and the cells, $p_{i\,ind}^{*}$ and $p_{c\,ind}^{*}$, respectively, which in turn are determined by the dipole coefficients of C_p^{*} and C_c^{*}. In the low-frequency range (f < 10 kHz), C_p^{*} and C_c^{*} are given by Eq. (6). Since the size of the latex particles and the yeast cells, as well as, the conductivity K_{e} of the suspending medium are known, the dipole coefficients are solely functions of the frequency:

$$C_p^{*}(\omega) = C_p^{*}\left(\omega,\ \zeta_p, \Theta_p\right) \quad ; \qquad C_c^{*}(\omega) = C_c^{*}\left(\omega,\ \zeta_c, \Theta_c\right) \tag{18}$$

In Eq. (18), the zeta potential $\zeta_{p(c)}$ and the surface conductivity ratio $\Theta_{p(c)}$ of the particles (p) and the cells (c) are unknown parameters. By taking the value of Θ_p = 0.56 deduced by Lyklema and Minor,[27] the parameters that completely determine the potential energy of interaction, and thus the forces acting on the particles (cells) are: ζ_p, ζ_c and Θ_c. Finally, by integration of the equations of motion (see below), we obtain the pathways of the latex particles and the yeast cell:

$$\begin{aligned} \mathbf{r}_i(t) &= \mathbf{r}_i\left(t,\ \omega,\ \zeta_p,\ \zeta_{\text{wall}}\right) \\ \mathbf{r}_c(t) &= \mathbf{r}_c\left(t,\ \omega,\ \zeta_c,\ \Theta_c,\ \zeta_{\text{wall}}\right) \\ \mathbf{r}_{ic}(t) &= \mathbf{r}_c(t) - \mathbf{r}_i(t); \qquad i = 1 \ldots N \end{aligned} \tag{19}$$

In Eq. (19), the parameter ζ_{wall} is the electrokinetic potential of the glass walls of the measuring chamber (see Fig. 1). ζ_{wall} is a measure for the electroosmotic- (e.o.) flow of the electrolyte solution between the glass slides. It should be noted that the velocity profile of the e.o.-flow is frequency dependent in the middle of the measuring chamber (in the frequency range under consideration), but it is not in the regions near the glass walls (observation plane), see Fig. 1. The observations show that the e.o.-flow has the same direction as the external field (negatively charged glass-walls), which is opposite to the electrophoretic motion of the latex particles and the yeast cells (ζ_p and ζ_c are negative). At frequencies at which the electrophoretic displacement is small (f > 10 Hz), the trajectories can be calculated using mean-time averaged forces, so that the relative position $\mathbf{r}_{ic}$ between a latex particle i and yeast cell c depends on four parameters (ω is known from the experiment under consideration):

$$\mathbf{r}_{ic}(t) = \mathbf{r}_{ic}\left(t,\ \omega,\ \zeta_p,\ \zeta_c,\ \Theta_c\right); \qquad \text{at} \quad \omega > 2\pi\, 10/\text{Hz} \tag{20}$$

Hence, the three equations in Eq. (19) together with Eq. (20) completely determine the parameters ζ_{wall}, ζ_p, ζ_c and Θ_c, provided that at three different frequencies, say ω_1, ω_2 and ω_3 the positions $\mathbf{r}_{ic}$, $\mathbf{r}_c$ and $\mathbf{r}_i$ are known. As Fig. 2 shows, the configurations of particles around the yeast cells at $f = \omega/2\pi$ = 3 Hz; f = 30 Hz; and f = 3 kHz are well distinguishable, giving a good reference for the simulations. An additional experimental information that results from the experimental data is the half-time $t_{1/2}^{freq}$ which characterizes the time that the particles require to reach stable configuration around the cells by any stepwise change of the frequency (f = 3 Hz → 30 Hz → 3 kHz and vice versa). Thus, by varying the optimization parameters ζ_p,

ζ_c and Θ_c, and comparing the simulated particles/cell configurations with the observations, we obtain the optimum values that fit the experiment, see Fig. 9 – Fig. 12.

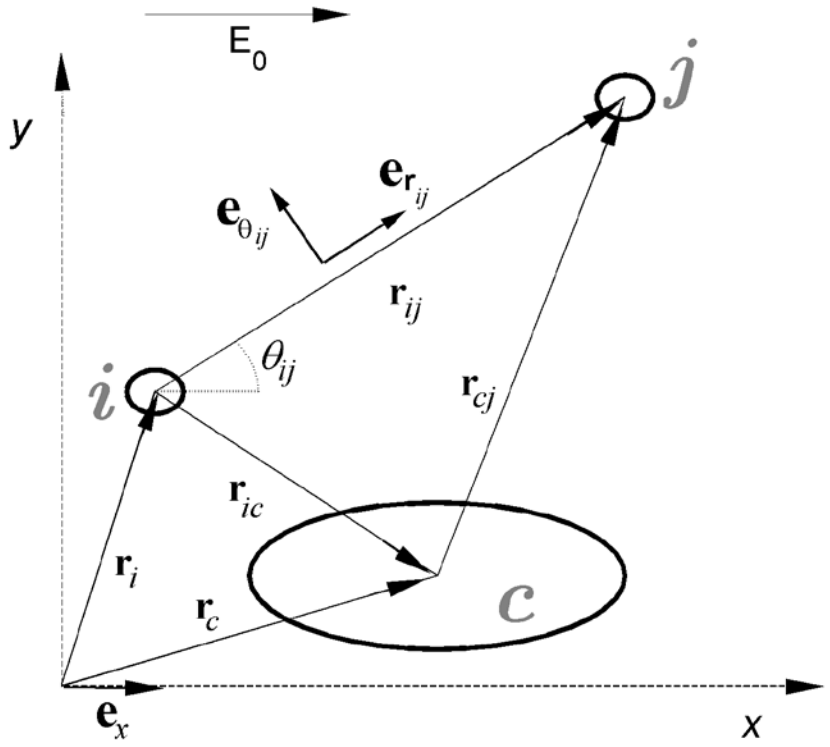

Fig. 7 Identification of symbols used in the derivation of the equations of motion of the polystyrene latex spheres (*i*, *j*) and a *S. pombe* yeast cell (*c*) in a uniform electric field $\mathbf{E} = \mathbf{E_0}\cos(\omega t)$.

4.6.2 Dielectrophoretic potential energy of interaction

If the external electric field is uniform and parallel, the force acting on each particle is due only the influence of the inhomogeneous electric field created by the neighboring particle. Because the force acting on a dielectric particle in inhomogeneous electric field is also called *dielectrophoretic* force, here we shall use the superscript "*diel*" notating a potential (or an force) of this kind.

The instantaneous interaction energy between two dissimilar particles *A* and *B* located at the origin of coordinates and at position **r**, respectively, is given by:

$$U_{AB}^{diel} = -\mathrm{Re}\left(\mathbf{p}_B^*\right)\cdot\mathrm{Re}\left(\mathbf{E}_A^*(\mathbf{r})\right) \tag{21}$$

In Eq. (21), $\mathbf{p}_B^*$ is the induced dipole moment of particle *B*, and $\mathbf{E}_A^*(\mathbf{r})$ is the field created by the induced dipole $\mathbf{p}_A^*$ of particle *A*, expressed as:

$$\mathbf{E}_A^*(\mathbf{r}) = \frac{3\left(\mathbf{p}_A^*\cdot\mathbf{r}\right)\mathbf{r} - r^2\mathbf{p}_A^*}{4\pi\,\varepsilon_0\varepsilon_e\,r^5} \tag{22}$$

Further, we only consider mutual polarization of first order, i.e., when considering the field $\mathbf{E}_A$ created by particle *A*, instead of using the net dipole moment $\mathbf{p}_A$ of particle *A* induced by its total local field $\mathbf{E}^*_{loc} = \mathbf{E}^* + \mathbf{E}^*_B$, where $\mathbf{E}^*$ denotes the external field, we only use the leading term in its dipole:

$$\mathbf{p}^*_{A,B} = \alpha^*_{A,B}\,\mathbf{E}^* \tag{23}$$

In Eq. (23), α^* denotes the polarizability of the colloid particle. Substituting Eq. (22) and Eq. (23) into Eq. (21), and considering a uniform electric field oscillating it the *x*-direction $\mathbf{E}^* = E_0.\exp(i\omega t).\mathbf{e}_x$, where $\mathbf{e}_x$ is the unit vector, we obtain for the instantaneous interaction energy between particle *A* and *B* the expression:

$$U_{AB}^{diel}(t) = -\frac{E_0^2}{4\pi\varepsilon_0\varepsilon_e}\mathrm{Re}\left(\alpha_A^*\,e^{i\omega t}\right)\mathrm{Re}\left(\alpha_B^*\,e^{i\omega t}\right)\frac{3\cos^2\theta - 1}{r^3} \tag{24}$$

In Eq. (24), r is the distance between particle centres and θ is the angle between the radius vector $\mathbf{r}$ and the unit vector $\mathbf{e}_x$.

The interaction energy, Eq. (24), is a product of simple harmonic functions of the time and we can evaluate the time average,[28] which in our yields:

$$\overline{U_{AB}^{diel}} = -\frac{E_0^2}{8\pi\varepsilon_0\varepsilon_e}\mathrm{Re}\left(\widetilde{\alpha_A^*}\,\alpha_B^*\right)\frac{3\cos^2\theta - 1}{r^3} \tag{25}$$

In Eq. (25), $\widetilde{\alpha^*}$ denotes the complex conjugate of the complex polarizability α^*. Consequently, the interaction energy can be expressed by the dipole coefficients C^* of the colloid particles by:

$$\alpha^*_{A,B} = 4\pi\,\varepsilon_0\varepsilon_e\,a^3_{A,B}C^*_{A,B}\ , \tag{26}$$

where a_A and a_B are the particle radii.

Applying Eq. (24) and Eq. (25) to the model system of N latex particles, each having radius a_p and dipole coefficient C_p^*, the instantaneous interaction energy between latex particles i and j, placed at positions $\mathbf{r}_i$ and $\mathbf{r}_j$, respectively, yields:

$$U_{ij}^{diel}(t) = -\,4\pi\,\varepsilon_0\varepsilon_e\,a_p^{\,6}\,C_p^{\,2}E_0^{\,2}\cos^2(\omega t+\psi_p)\,\frac{3\cos^2\theta_{ij}-1}{r_{ij}^3} \tag{27}$$

$$\overline{U_{ij}^{diel}} = -\,2\pi\varepsilon_0\varepsilon_e\,a_p^{\,6}\,C_p^{\,2}E_0^{\,2}\,\frac{3\cos^2\theta_{ij}-1}{r_{ij}^3} \tag{28}$$

In Eqs. (27) and (28), $r_{ij} = |\mathbf{r}_j - \mathbf{r}_i|$ is the center-to-center distance between the latex particles, $C_p = [C_p'^{\,2} + C_p''^{\,2}]^{1/2}$ is the magnitude and $\psi_p = \arctan[C_p'' / C_p']$ is the phase of the particle dipole coefficient $C_p^* = C_p \exp(i\psi_p)$.

Accordingly, the interaction energy between latex particle i and the yeast cell c placed at positions $\mathbf{r}_i$ and $\mathbf{r}_c$, respectively, is given by:

$$U_{ic}^{diel}(t) = -\,4\pi\,\varepsilon_0\varepsilon_e\,a_c^{eff\,3}a_p^{\,3}\,C_cC_p\,E_0^{\,2}\cos\left(\omega t+\psi_c\right)\cos\left(\omega t+\psi_p\right)\frac{3\cos^2\theta_{ic}-1}{r_{ic}^3} \tag{29}$$

and

$$\overline{U_{ic}^{diel}} = -\,2\pi\,\varepsilon_0\varepsilon_e\,a_c^{eff\,3}a_p^{\,3}\,C_cC_p\,E_0^{\,2}\cos\left(\psi_c-\psi_p\right)\frac{3\cos^2\theta_{ic}-1}{r_{ic}^3} \tag{30}$$

In Eqs. (29) and (30), $r_{ic} = |\mathbf{r}_c - \mathbf{r}_i|$ is the center-to-center distance, C_c is the magnitude, ψ_c is the phase of the dipole coefficient of the yeast cell and a_c^{eff} denotes the effective cell radius calculated by $a_c^{eff} = (a_c \times b_c^{\,2})^{1/3}$, with a_c and b_c being the polar and equatorial radii of the cell body (prolate spheroid oriented parallel to the applied field, see Fig. 7).

Eq. (30) shows that the interaction can be attractive or repulsive depending on the sign of two factors:[6] an electrical factor $\cos(\psi_c - \psi_p)$, that accounts for the phase difference of the induced dipole moments and a geometrical factor $(3\cos^2\theta - 1)/r$, that considers the relative positions of the interacting particles. For identical colloid particles (or cells) the factor $\cos(\psi_c - \psi_p)$ is positive at any ω (because $\psi_c \equiv \psi_p$) and the particles move to positions at which the geometrical factor is positive, that is $\theta = 0°$, leading to formation of chains along the field lines.

An example for dipolophoretic interaction of three particles of same kind is given in Fig. 8, where the trajectories are calculated by solving the equations of motion (see below). Same configuration of chain formation applies for particles of different kind (as the latex particles and the yeast cells) if the electrical factor positive: the particles aggregate on the cell-poles facing the external field. However, at frequencies where the electrical factor is negative, the geometrical factor tends also to become negative (in order to minimize the energy), giving a minimum at $\theta = 90°$. The latter configuration corresponds to aggregation of latex particles on the equators of the yeast cells. The two characteristic configurations for latex particles and yeast cells are shown schematically in Fig. 14(a).

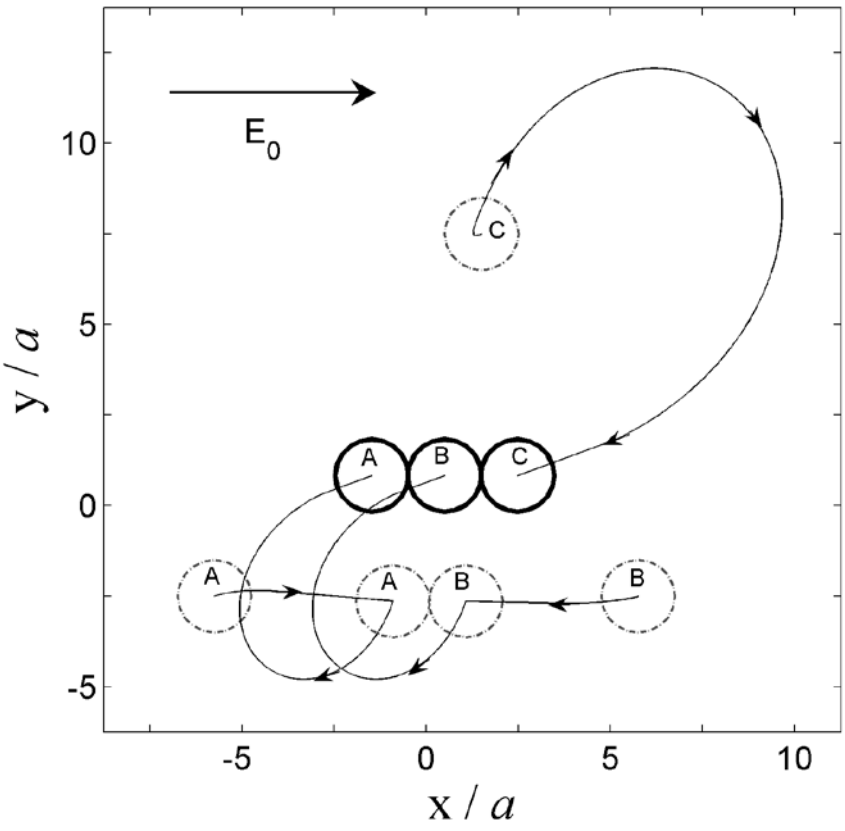

Fig. 8 Calculated pathways of three identical particles (or biological cells) of radius *a* obeying *induced dipole – induced dipole* interaction in uniform alternating electric field, $\mathbf{E} = \mathbf{E_0}\cos(\omega t)$.
In this particular case of initial configuration, the time that the system requires to build up the doublet AB is $t_{AB} = 6500\eta / \varepsilon_0\varepsilon_e E_0^{\,2} C^2$ s, where $C = C(\omega) = [C_p'^{\,2}(\omega) + C_p''^{\,2}(\omega)]^{1/2}$ is the magnitude of the complex dipole coefficient of the particles $C^*(\omega)$. The time for building up the triplet ABC is $t_{ABC} \approx 47 \times t_{AB}$. Trajectories calculated by integration of the mean-time average equations of motion for three spheres, Eq. (A5.1). In this example only hard-core repulsive force is considered, see Appendix 5.

4.6.3 Electrostatic energy of interaction

When a polystyrene particle approaches an identical neighboring particle so that the electrical double layers of the charged particles begin to overlap the result is usually a repulsive force, which tends to oppose further approach. If the particle approaches yeast cell which has a surface electrostatic potential of the same sign it experiences repulsion too. The magnitude of the repulsion force can be calculated from the repulsive potential energy U_{ij}^{rep} between the charged surfaces of particle *i* and *j*, respectively. U_{ij}^{rep} can be determined either by the electric surface potentials or by the surface electric charge of the surfaces. We shall use the first case, the constant surface potential approach, which is the basis of the DLVO theory of colloid stability. In this chase it is assumed that the surface potentials remain constant during approach. For particles of radii a_i and a_j, in the case of thin double layer ($\kappa a >> 1$), U_{ij}^{rep} is given by: [30]

$$U_{ij}^{rep} = \varepsilon_0 \varepsilon_e \left(\frac{k_B T}{e} \right)^2 Y_i Y_j \frac{a_i a_j}{r_{ij}} \exp\left(-\kappa H_{ij} \right), \tag{31}$$

where

$$\begin{aligned} H_{ij} &= r_{ij} - a_i - a_j \\ Y_i &= 4 \tanh\left(\hat{\varphi}_{0i} / 4 \right) \\ \hat{\varphi}_{0i} &= ze\varphi_{0i} / k_B T \end{aligned} \tag{32}$$

for $\kappa H \geq 4; \quad \hat{\varphi}_{0i} < 8; \quad \kappa a_i \geq 10$

In Eq. (31) and Eq. (32), H_{ij} is the distance of close-approach, r_{ij} is the distance between particle centers, z is the charge number of the electrolyte dissociated in the solution, κ is the *Debye-Hückel* parameter given by Eq. (1) and φ_{0i} represents the surface potential of particle *i*.

4.6.4 Forces between the latex particles and the yeast cells

The mean dielectrophoretic force. The force between particles *i* and *j*, as well as, between particle *i* and yeast cell *c*, can be calculated by taking the negative gradient of the potential energies of interaction, Eq. (28) and Eq. (30). The corresponding mean forces (time independent) may be expressed in dimensionless forms as:

$$\overline{\mathbf{f}_{ij}^{diel}} = \frac{\overline{\boldsymbol{F}_{ij}^{diel}}}{F_0} = \frac{C_p{}^2}{\hat{r}_{ij}^{\,4}}\left[\left(3\cos^2\theta_{ij} - 1\right)\mathbf{e}_{\mathbf{r}_{ij}} + \left(\sin 2\theta_{ij}\right)\mathbf{e}_{\boldsymbol{\theta}_{ij}}\right] \tag{33}$$

$$\overline{\mathbf{f}_{ic}^{diel}} = \frac{\overline{\boldsymbol{F}_{ic}^{diel}}}{F_0} = \left(\frac{a_c^{eff}}{a_p}\right)^3 \frac{C_p C_c \cos\left(\psi_c - \psi_p\right)}{\hat{r}_{ic}^{\,4}}\left[\left(3\cos^2\theta_{ic} - 1\right)\mathbf{e}_{\mathbf{r}_{ic}} + \left(\sin 2\theta_{ic}\right)\mathbf{e}_{\boldsymbol{\theta}_{ic}}\right] \tag{34}$$

where

$$F_0 = 6\pi a_p^2\, \varepsilon_0 \varepsilon_e\, E_0^2 \tag{35}$$

$$\hat{r}_{ij} = r_{ij} / a_p \quad ; \quad \hat{r}_{ic} = r_{ic} / a_p \tag{36}$$

$$\hat{t} = t / t_0 \quad ; \quad t_0 = 6\pi\eta a_p^2 / F_0 \tag{37}$$

In Eqs. (33) - (37), $\mathbf{e}_{rij}$ and $\mathbf{e}_{\theta ij}$ are the radial and the tangential unit vectors with respect to $\mathbf{r}_{ij}$, respectively (see Fig. 7). The superscript "^" denotes dimensionless variables. The natural time unit t_0, Eq. (37), allows for a convenient transformation to dimensionless differential equations (see below). Consequently, by taking the negative gradients of Eq. (27) and Eq. (29) we obtain the time-dependent (dimensionless) forces $\mathbf{f}_{ij} = \mathbf{f}_{ij}(t)$ and $\mathbf{f}_{ic} = \mathbf{f}_{ic}(t)$ expressed in the Appendix 2 by Eq. (A2.1) and Eq. (A2.2), respectively.

Hydrodynamic force. The spherical latex particles and the yeast cells are subject to hydrodynamic drag force due to their motion through the liquid phase. As initial approximation, the hydrodynamic resistance is given by the Stoke's law: $\mathbf{F} = -6\pi a\eta.(\mathrm{d}\mathbf{r}/\mathrm{d}t)$. The dimensionless drag forces ($\mathbf{f} = \mathbf{F}/F_0$) acting on a particle *i* and a cell *c* are given by:

$$\mathbf{f}_i^{hyd} = -\frac{d\,\hat{\mathbf{r}}_i}{d\,\hat{t}}; \qquad \mathbf{f}_c^{hyd} = -\left(\frac{a_c^{\mathrm{eff}}}{a_p}\right)\frac{d\,\hat{\mathbf{r}}_c}{d\,\hat{t}} \tag{38}$$

The repulsive electrostatic forces between particle *i* and particle *j*, as well as, between particle *i* and cell *c*, $\mathbf{f}_{ij}$ and $\mathbf{f}_{ic}$, respectivelly, are calculated by taking the negative gradient of U_{ij}^{rep} and U_{ic}^{rep}, Eq. (31) and Eq. (32). For simplicity of the calculations, the surface potentials are approximated by $\varphi_{0p} \approx \zeta_p$ (for the ith particle) and $\varphi_{0c} \approx \zeta_c$ (for the yeast cells). Applying the inequality $(a_i a_j / r_{ij}^2) << (\kappa a_i a_j / r_{ij})$ valid for $\kappa a > 10$ and $(r/a) > 2$, yields the dimensionless ($\mathbf{f} = \mathbf{F}/F_0$) forces:

$$\overline{\mathbf{f}_{ij}^{rep}} = A\left(\hat{\zeta}_p\right)\cdot\frac{\kappa a_p}{\hat{r}_{ij}}\exp\left[-\kappa a_p(\hat{r}_{ij}-2)\right]\ (-\mathbf{e}_{\mathbf{r}_{ij}}) \tag{39}$$

$$\overline{\mathbf{f}_{ic}^{rep}} = B\left(\hat{\zeta}_p, \hat{\zeta}_c\right)\cdot\frac{\kappa a_c^{eff}}{\hat{r}_{ic}}\exp\left[-\kappa a_p(\hat{r}_{ic}-\hat{r}_{ic}^{0})\right]\ (-\mathbf{e}_{\mathbf{r}_{ic}}), \tag{40}$$

In Eq. (39) and Eq. (40), the dimensionless factors $A(\hat{\zeta}_p)$ and $B(\hat{\zeta}_p, \hat{\zeta}_c)$ are function of the scaled ζ-potentials $\hat{\zeta}_{p(c)} = e\zeta_{p(c)}/k_BT$. The expressions for $A(\hat{\zeta}_p)$ and $B(\hat{\zeta}_p, \hat{\zeta}_c)$ are given by Eq. (A3.1) of the Appendix 3. In Eq. (40), $\hat{r}_{ic}^{0}$ is the particle-cell (center-to-center) distance at particle contact, that is, when the particle *i* contacts the yeast cell (i.e., at $H_{ic} = 0$, see Eq. (31)). The scaled center-to-center distance $\hat{r}_{ic}^{0}$ is expressed in the Appendix 3.

Electrophoretic force. Considering electrophoretic motion of a spherical colloid particle with radius *a* in a liquid phase under action of an external (vector) field **E**, the electrophoretic (scalar) mobility μ is defined by $\mathbf{v}^{el} = \mu.\mathbf{E}$, where $\mathbf{v}^{el}$ is the particle electrophoretic velocity.
In order to include the electrophoretic motion of the latex particles and the yeast cells in the equations of motion, we introduce an effective driving force F^{el} (*electrophoretic* force) such that, in competition with the Stoke's frictional force ($F = 6\pi a\eta$v) to result in motion with same velocity as the electrophoretic velocity $\mathbf{v}^{el}$, that is, $\mathbf{F}^{el} = 6\pi a\eta\,\mathbf{v}^{el}$. Note that this force is not the actual electrostatic driving force. The actual forces involved, such as for instance, the electrostatic force (exerted on the fixed surface charge) and the polarization force (retardation by the induced polarization field of the counterions), are all included by the derivation of the electrophoretic mobility as function of the electrokinetic potential $\mu = \mu(\zeta)$, and so they are all accounted for trough the electrophoretic velocity $\mathbf{v}^{el}$. Here we apply the expression for μ deduced by O'Brien and Hunter,[29] Eq. (A4.1) of the Appendix 4. Fig. 10(b) shows the mobility μ as a function of ζ for the latex particles and the *S. pombe* yeast cells. Including the electroosmotic liquid flow near the glass wall of the measuring chamber, we obtain $\mathbf{F}^{el} = 6\pi a\eta(\mathbf{v}^{el}+\mathbf{v}_w^{eo})$, where $\mathbf{v}_w^{eo}$ is the electro-osmotic velocity of the solution near the glass walls, see Fig. 1(b). The electro-osmotic velocity of the bulk electrolyte is related to the electrostatic potential at the slipping plane of the glass surface ζ_{wall} via $\mathbf{v}_w^{eo} = -(\varepsilon_0\varepsilon_e\zeta_{wall}/\eta)\mathbf{E}$. Hence, for electric field alternating in the x-direction $\mathbf{E} = E_0\cdot\cos(\omega t)\mathbf{e}_x$, the dimensionless electrophoretic forces ($\mathbf{f}^{el} = \mathbf{F}^{el}/F_0$) are given by:

$$\mathbf{f}_i^{el} = \frac{k_B T/e}{a_p E_0}\left(\hat{\mu}_p - \hat{\zeta}_{\text{wall}}\right)\cos\left(\hat{\omega}\hat{t}\right)\mathbf{e}_{\text{x}} \tag{41}$$

$$\mathbf{f}_c^{el} = \left(\frac{a_c^{eff}}{a_p}\right)\frac{k_B T/e}{a_p E_0}\left(\hat{\mu}_c - \hat{\zeta}_{\text{wall}}\right)\cos\left(\hat{\omega}\hat{t}\right)\mathbf{e}_{\text{x}} \tag{42}$$

In Eq. (41) and Eq. (42), $\hat{\zeta}_{wall} = e\zeta_{wall} / k_B T$ is the dimensionless electrokinetic potential of the measuring glass slit-chamber, see Fig. 1. The dimensionless electrophoretic mobility $\hat{\mu}_{p(c)} = \hat{\mu}_{p(c)}(\hat{\varsigma}_{p(c)})$ of the particles (cells), expressed by the dimensionless potential $\hat{\varsigma}_{p(c)}$, is given by Eq. (A4.1) of the Appendix 4.

4.6.5 Equations of motion

The motion of *N* identical latex particles, each having mass m_p and position $\mathbf{r}_i$, and one yeast cell with mass m_c placed at $\mathbf{r}_c$, is governed by Newton's equation of motion. Using the scale factors introduced by Eqs. (35), (36) and (37), we obtain the dimensionless set of equations:

$$\begin{aligned}
\Gamma_p \frac{d^2\hat{\mathbf{r}}_i}{d\hat{t}^2} &= \sum_{j(\neq i)} \mathbf{f}_{ij}^{del} + \mathbf{f}_{ic}^{del} + \sum_{j(\neq i)} \overline{\mathbf{f}_{ij}^{rep}} + \overline{\mathbf{f}_{ic}^{rep}} + \mathbf{f}_i^{el} - \frac{d\hat{\mathbf{r}}_i}{d\hat{t}} \\
\Gamma_c \frac{d^2\hat{\mathbf{r}}_c}{d\hat{t}^2} &= \sum_{j} \mathbf{f}_{cj}^{del} + \sum_{j} \overline{\mathbf{f}_{cj}^{rep}} + \mathbf{f}_c^{el} - \left(\frac{a_c^{eff}}{a_p}\right)\frac{d\hat{\mathbf{r}}_c}{d\hat{t}} \quad ; \quad i, j = 1...N
\end{aligned}, \tag{43}$$

where

$$\Gamma_{p,c} = \frac{m_{p,c} F_0}{36\pi^2\eta^2 a_p^3} \tag{44}$$

The last terms on the right-hand side of Eq. (43) represent the hydrodynamic drag forces (see Eq. (38)). For particle (cell) radius of a_p (a_c^{eff}) = 0.4 μm (3 μm), assuming particle (cell) density of same order as water, the mass of a particle and a cell are $m_p \approx O(10^{-16})$ kg and $m_c \approx O(10^{-14})$ kg, respectively. For $\eta \approx 10 \times 10^{-4}$ Pa s and E_0 = (1 … 5) × 10^4 V m^{-1}, the acceleration terms are $\Gamma_p \sim O(10^{-5})$ and $\Gamma_c \sim O(10^{-2})$, which are small compared to the corresponding velocity terms and can be safely neglected. Thus, the equations of motion, Eq. (43), transform to:

$$\frac{d\hat{\mathbf{r}}_i}{d\hat{t}} = \sum_{j(\neq i)} \mathbf{f}_{ij}^{diel} + \mathbf{f}_{ic}^{del} + \sum_{j(\neq i)} \overline{\mathbf{f}_{ij}^{rep}} + \overline{\mathbf{f}_{ic}^{rep}} + \mathbf{f}_i^{el};$$
$$\frac{a_c^{eff}}{a_p}\frac{d\hat{\mathbf{r}}_c}{d\hat{t}} = \sum_j \mathbf{f}_{cj}^{diel} + \sum_j \overline{\mathbf{f}_{cj}^{rep}} + \mathbf{f}_c^{el}; \qquad i, j = 1...N \tag{45}$$

Eq. (45) is the set of equations to be solved for the dimensionless trajectories $\hat{\mathbf{r}}_i = \hat{\mathbf{r}}_i(\hat{t})$ and $\hat{\mathbf{r}}_c = \hat{\mathbf{r}}_c(\hat{t})$. At higher frequency, where the electrophoretic displacement for a half-period of the alternating electric field is small, Eq. (45) is approximated by:

$$\frac{d\hat{\mathbf{r}}_i}{d\hat{t}} = \sum_{j(\neq i)} \overline{\mathbf{f}_{ij}^{diel}} + \overline{\mathbf{f}_{ic}^{diel}} + \sum_{j(\neq i)} \overline{\mathbf{f}_{ij}^{rep}} + \overline{\mathbf{f}_{ic}^{rep}}$$
$$\frac{a_c^{eff}}{a_p}\frac{d\hat{\mathbf{r}}_c}{d\hat{t}} = \sum_j \overline{\mathbf{f}_{cj}^{diel}} + \sum_j \overline{\mathbf{f}_{cj}^{rep}}; \qquad i, j = 1...N \tag{46}$$

6. Results and discussion

The polarization of the latex particle and the yeast cells in the low-frequency range $0 \le f$ / kHz ≤ 10 is dominated by the polarization of the counterion atmosphere of the charged particles. In order to quantify the main electro-kinetic characteristics of the yeast cells and the latex particles, the dynamics of the shape of the particles/cells aggregates were simulated in the two-dimensional case and compared with the experiment. Figure 9 shows an example of the simulation. The initial configuration was comprised of 40 identical latex particles randomly positioned around a cell (first placed on a square lattice and then randomly slightly dispersed), see Fig. 9(a). The starting configuration is the initial positions at $t = 0$ when the field is instantaneously applied. At that time, the system begins to evolve according to equations Eq. (46) and the latex particles reach an equilibrium configuration after time-interval characterized by the half-time $t_{1/2}{}^{on}$, see Fig. 9(b). After that, the frequency was changed stepwise and the system equilibrates to a new configuration characterized by $t_{1/2}{}^{freq}$. The equations of motion are solved numerically using self-written source code (Matlab environment, Runge-Kutta method). The Brownian forces are on the order of kT / a_p. In the field range of interest here, $100 \le E_0/(\mathrm{V\ cm^{-1}}) \le 600$, the inequality $F_0 >> kT/a_p$ holds, therefore the effect of Brownian motion can be safely neglected. Our computer simulation program also kept track of the trajectories and the velocities of the particles.

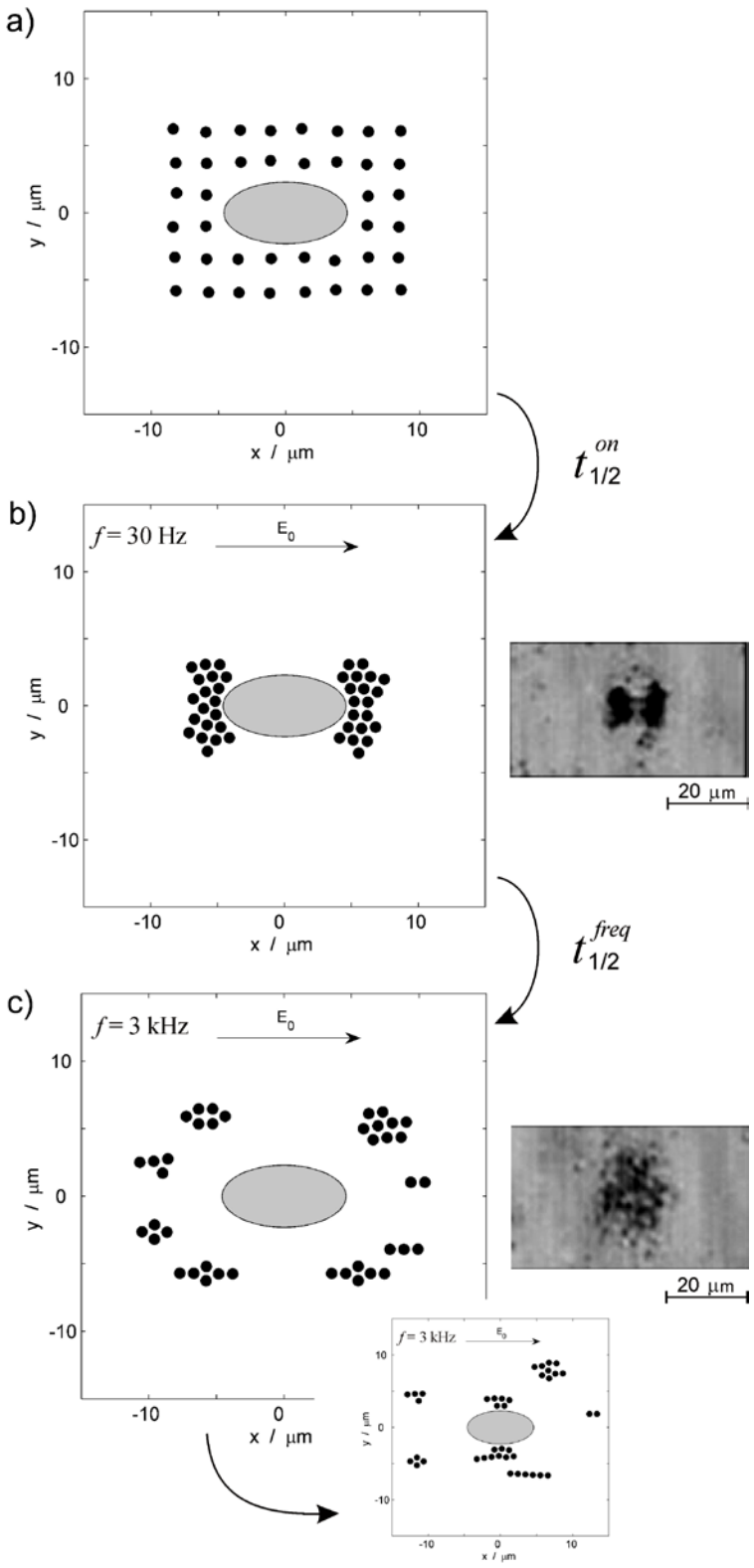

Fig.9 Simulated configurations of polystyrene latex particles and *S. pombe* yeast cell suspended in 10^{-4} M NaCl solution at different frequencies of the applied electric field: (a) initial configuration (E_0 = 0), (b) f = 30 Hz and (c) f = 3 kHz. The classical model (diffuse counterion cloud) polarization of the yeast cell fails to predict the shape and the half-times of the aggregates, whereas the new polarization model of polarization of the cell-glycocalyx agrees with the experiment, see Fig.11 and Fig. 12.

The values of the fixed parameters are: Θ_p = 0.56; a_c^{eff} = 3 μm; a_p = 400 nm. Field intensity range of the simulations: 100 ≤ E_0 /(V cm^{-1}) ≤ 600. The obtained values of the optimisation parameters are: ζ_p = –76 (± 4) mV, ζ_c = –57 (± 4) mV, ζ_{wall} = –51 (± 4) mV and Θ_c = 27 (± 3).

The results are coupled to the simulations at f = 3 Hz, see Fig. 10.

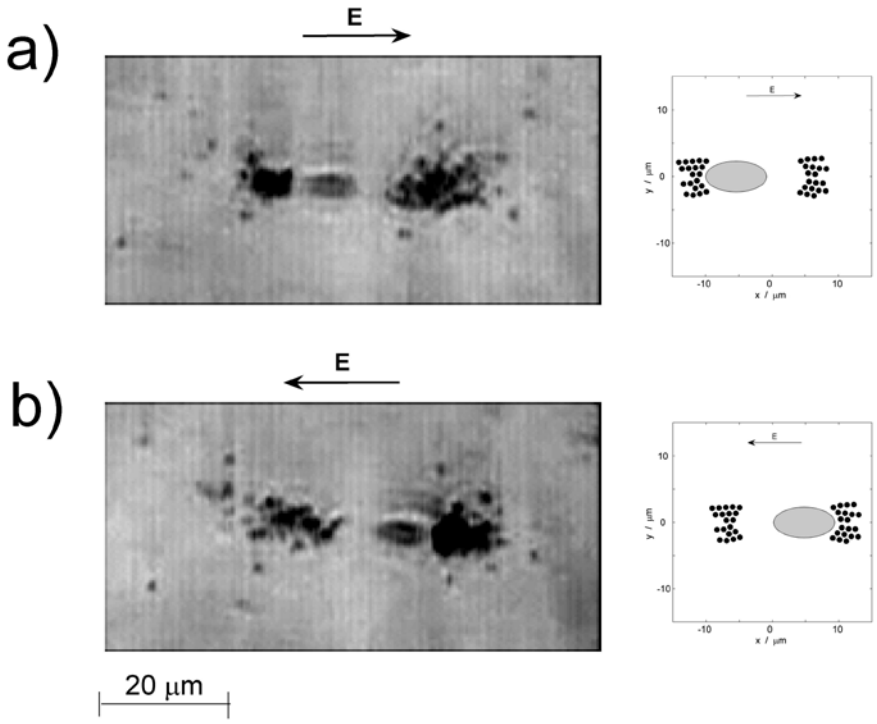

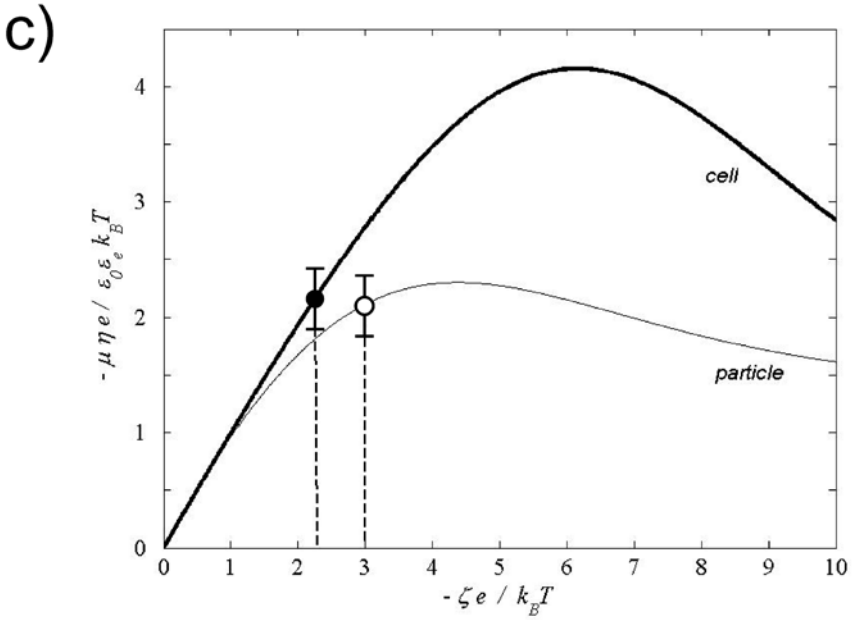

Fig. 10 The comparison of the experimental observation and the theoretical simulation of the particles/cell aggregates (a) in the two half-periods of the applied a.c. electric field (E_0 = 600 V/cm; f = 3 Hz) yields, via the electrophoretic mobility μ(ζ) (b), the electrokinetic potentials of the polystyrene-latex particles and the yeast cells, ζ_p and ζ_c, respectively. The results are related to the simulation at f = 30 Hz and f = 3 kHz, see Fig. 9. Same parameters as Fig. 9. Rest experimental conditions: η = 8.9×10^{-4} kg m^{-1} s^{-1}; T= 298 K.

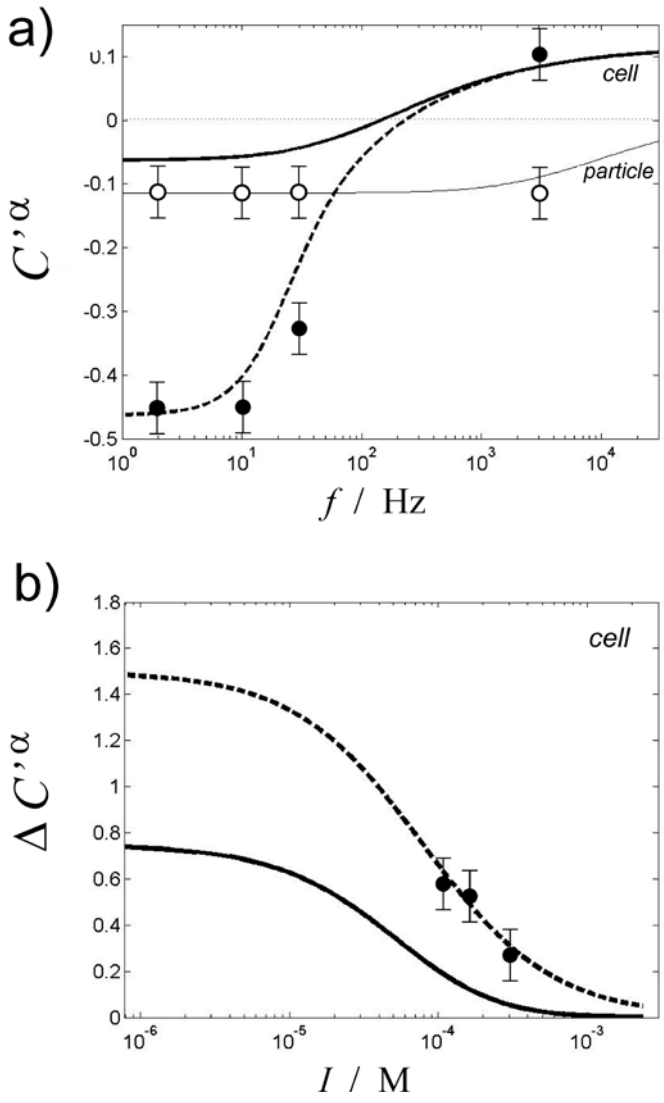

Fig. 11 (a) Comparison between the theoretical (continuous curves) and the experimentally obtained (symbols) frequency dependences of the real dipole coefficients of the latex particles and the yeast cells, $C'_p{}^{\alpha}(\omega)$ and $C'_c{}^{\alpha}(\omega)$, respectively, at I = 160 μM. The classical model of diffuse counterion-cloud polarization applied for polystyrene particles (o) agrees the experimental observation, but it fails to predict the polarization of the yeast cells (•). The new model of Schwarz-like polarization of the cell-glycocalyx (dashed curve) rationalizes the experiment.

(b) The magnitude of the α-polarization of the yeast cells, here described in terms of the dipole coefficient difference $\Delta C'_c{}^{\alpha} = C'_c{}^{\alpha H} - C'_c{}^{\alpha L}$, as a function of the ionic strength I of the suspending medium. The superscripts H and L denote the high- (10^4 Hz) and the low- (0 Hz) frequency limits of the dipole coefficient $C^{\alpha *}(\omega)$, respectively. The standard model (continuous curve) disagrees with the experimental data (•), whereas the new glycocalyx-shell polarization model (dashed curve) rationalizes the experiment. The theoretical curves are calculated using Eq. (6) - Eq. (9). Surface conductivity of the yeast cells: $K^{\sigma} = 3 \times 10^{-9}$ S. The rest parameters are the same as in Figure 9.

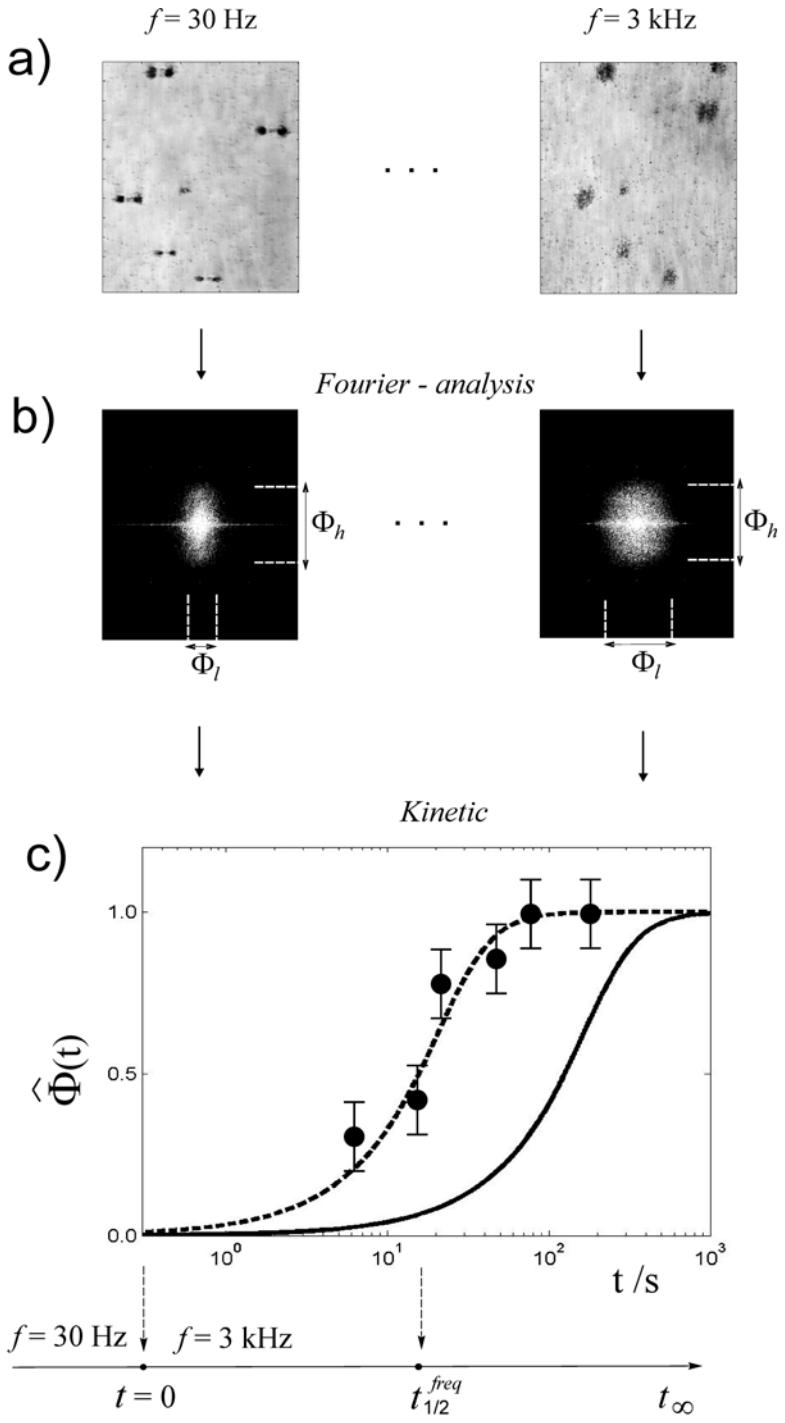

Fig. 12 The time evolution of the shape of the particles/cell aggregates by changing frequency from f = 30 Hz to f = 3 kHz (at constant E_0). The shape changes of the the aggregates with time are analyzed in terms of the (normalized) shape-factor $\widehat{\Phi}(t)$ defined as $\widehat{\Phi}(t) = [\Phi_{hl}(t) - \Phi_{hl}(0)] / \Phi_{hl}(t_\infty)$, where $\Phi_{hl} = \Phi_h / \Phi_l$ is the shape-factor of the Fourier transform (b) of the optical microscope images (a). (c) The comparison of the experimental data (•) (E_0 = 600 V/cm) with the theoretical simulation (continuous curves). The classical model of diffuse counterion-cloud polarization (continuous curve) fails to predict the experimental half-time $t_{1/2}^{freq}$ of the particles rearrangement, whereas the new glycocalyx-shell polarization model (dashed curve) rationalizes the experimental data.

First, the simulation was carried out using the classical (diffuse counterion-cloud) polarization model for the latex particles and the yeast cells. In this case, the dipole coefficients of the latex particles and the yeast cells, C_p^* and C_c^*, respectively, are expressed by Eq. (6) and Eq. (14). The corresponding ζ-potentials are related to the electrophoretic mobilities $\mu_p(\zeta_p)$ and $\mu_c(\zeta_c)$, Eq. (A4.1) in the Appendix 4. By varying the optimization parameters (ζ_p, ζ_c, ζ_{wall} and Θ_c) in the simulation and comparing the simulated particles/cell configurations with the experiment (see Fig. 9 - Fig. 12) we obtain the optimum values which fit the experimental data: ζ_p = −76 (± 4) mV, ζ_c = −57 (± 4) mV, ζ_{wall} = −51 (± 4) mV and Θ_c = 27 (± 3). The corresponding total (static) surface conductivity of the yeast cells (in the medium conductivity range $15 \le K_e/(\mathrm{S\ m^{-1}}) \le 25$ is K^{σ}_c = 3.0 (±0.3) nS. Since $\Theta_c = K^{\sigma i} / K^{\sigma d} = 27$, the inequality $K^{\sigma i} >> K^{\sigma d}$ holds, and the approximation $K^{\sigma}_c = K^{\sigma i} + K^{\sigma d} \approx K^{\sigma i}$ applies. Since $K^{\sigma} = u_i\, \sigma_i \approx u_i \cdot(-\sigma_0)$, and considering ion-mobility $u_i = u_L$, where u_i is the ion-mobility in the inner region of the double layer and $u_L = 8\times10^{-8}\ \mathrm{m^2\,V^{-1}\,s^{-1}}$ is that in the bulk, we obtain the surface charge density of the yeast cells $\sigma_{0,cell} = -4\ (\pm0.2)\ \mu\mathrm{C\ cm^{-2}}$.

The main result of the simulations is that the classical model of diffuse counterion-cloud polarization applied for the polystyrene particles agrees the experimental data, however it fails to predict the polarization of the yeast cells, see Fig. 9 – Fig. 12. This discrepancy can be seen, for instance, by changing the frequency of the applied field from f = 30 Hz to f = 3 kHz, resulting in shape change of the particles-cell aggregates (‘pole-capes’ - ‘equator’ transition). The experimental half-times of this transition $t_{1/2}^{freq}$ are approximately one order of magnitude shorter than that predicted by the classical model, see Fig. 12. This discrepancy cannot be rationalized by varying the optimization parameters alone. For example, an increase in the ζ_p -value of the latex particles leads in the simulation to higher induced dipole moment which decreases $t_{1/2}^{freq}$ to the proper value. However, the shape of the aggregates differs from that of the experiment: a higher particle dipole moment increases the interaction between the particles, resulting in long chains of particles on the pole-capes of the yeast cells instead of a clouds-like arrangement (as the experiment shows). Similarly, an increase in the ζ_c -value (or Θ_c) of the yeast cells also will decrease $t_{1/2}^{freq}$ to the proper value. However, in this case we cannot explain the observed ‘pole capes’ – ‘equator’ transition, since the real dipole coefficient of the yeast cells $C_c'(\omega)$ does not change sign with frequency. This can be seen in Fig. 6(a): at $Du(\zeta_c,\Theta_c)$ = 0.6 the dipole coefficient C_c' changes sign (at f = 100 Hz), whereas

at higher $Du(\zeta_c,\Theta_c) = 2$ it is positive in the entire low-frequency range (1 Hz - 4 kHz). Recall that, the parameters ζ_p and ζ_c are additionally related to experimental data via the electrophoretic displacement ($f \leq 10$ Hz, see Fig. 10).

The above examples show that the discrepancy between simulation and experiment cannot be rationalized in the frame of the classical (diffuse counterion-cloud) polarization model.

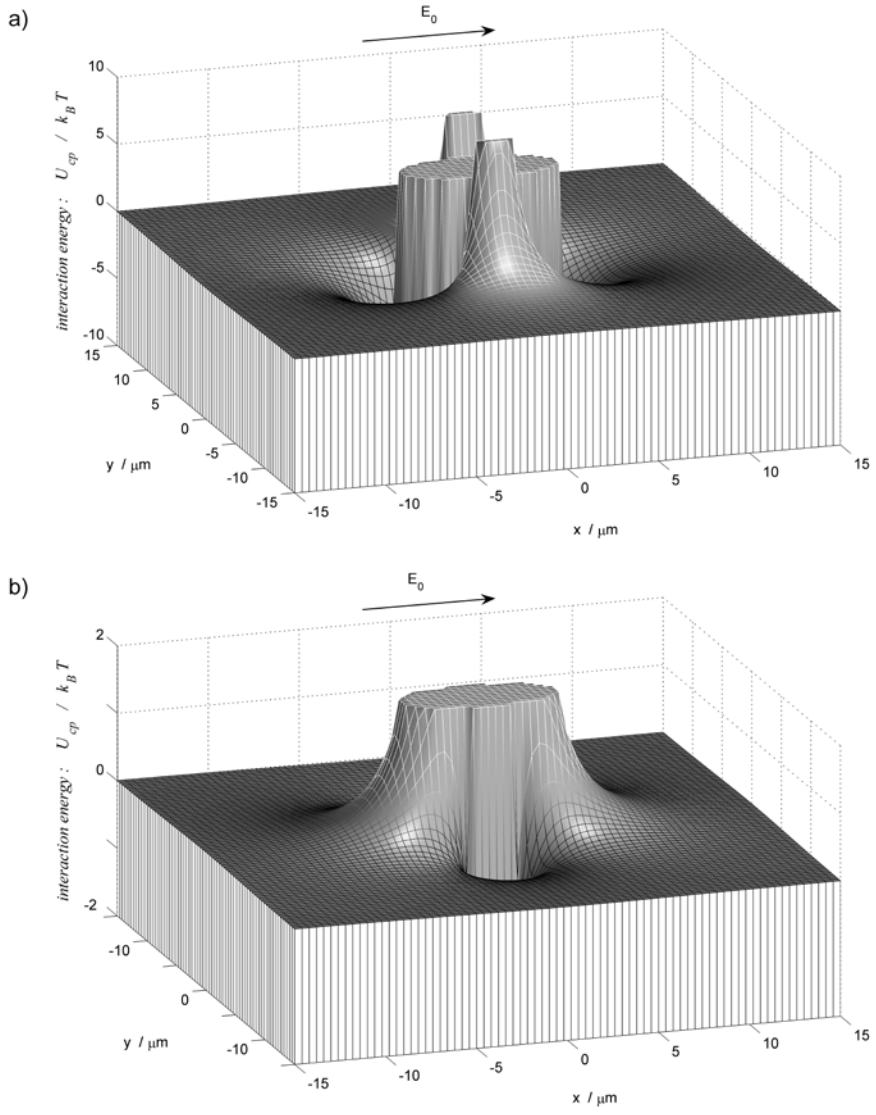

Fig. 13. The interaction potential energy profile between *S. pombe* yeast cell (effective radius $a_c^{\text{eff}} = 3$ μm; the prolate ellipsoidal cross section in the middle) and polystyrene latex particle (radius a_p = 400 nm), Eq. (30). The uniform electric field $\mathbf{E} = \mathbf{E_0}\cdot\cos(2\pi f\cdot t)$ is applied in the x-direction; (a) $f = 3$ Hz and (b) $f = 3$ kHz (b) according to Eq. (30). Same parameters as Fig. 9. By the assumption of retarded counterion exchange between the inner and the outer double layer (lateral redistribution is possible) we consider that the electrical surface properties of the yeast cells differ from that of the latex particles. Hence, the reason for such a difference should be sought in the glycocalyx layer of the biological cell.

If we assume that the polarization of the *S. pombe* yeast cells is governed by the new (*Schwarz* –like) polarization mechanism, the magnitude and the phase of the i.d.m. rationalizes the characteristic half-times of the aggregates and the sign change with frequency, as seen in Fig. 11(a) and Fig. 12. In the Schwarz's polarization model there is no (or retarded) ion exchange between the inner and the outer (diffuse) regions of the counterion-cloud layer. This restriction results in a phase shift between current and field in the inner part of the double layer. That is, the inner surface conductivity is frequency dependent and can be described (analogous to the Schwarz's model) by a complex surface conductivity given by Eq. (15). In Eq. (15), for simplicity of the calculations, we have chosen the relaxation time $\tau^{\alpha\,\mathrm{i}}$ of the inner layer equal to that of the diffuse layer: $\tau^{\alpha\,\mathrm{i}} \approx \tau^{\alpha\,\mathrm{d}} = a^2/2D$. In general, because the ion mobility in the diffuse layer exceeds that in the inner part, it is expected that $\tau^{\alpha\,\mathrm{i}} > \tau^{\alpha\,\mathrm{d}}$.

The influence of the plyionic glycocalyx charges on the potential distribution is theoretically investigated by Schnitzer,[31] who considered both cases: uniform and non-uniform (fixed) charge distribution in the glycocalyx layer. Experimental data reported in the literature suggest a non-uniformly charge distribution in the polyionic glycocalyx. Anionic glycolipids significantly alter lipophilic ion adsorption.[32], [33] This effect was greater for anionic site(s) in gangliosides being located several Å from the lipid membrane surface. X-ray diffraction [34] and electrokinetic studies of gangliosides embedded in bilayer membrane show that the sialic acid is located 10 Å from the lipid surface in a planar distribution.[31]

We suggest that the fixed charged groups in the cell glycocalyx shell are responsible for the *Schwarz*-like polarization of the *S. pombe* yeast cells at frequencies below 10 kHz. The electric potential profile of the proposed model is shown schematically in Fig. 13(b). Since the positive couterions, being electrostatically attracted by the fixed negative charges in the glycocalyx shell, are hindered to move normal to the surface but can move laterally. In external field this electro-kinetic behaviour of the couterions provides condition for *Schwarz*-like polarization. As consequence, the induced dipole moment of the yeast cells is much higher than that expected from the standard (diffuse double layer) polarization. There are (at least) two implications of the proposed model which could the model be correct:

(i) An additional dielectric dispersion of the suspension of cells $\varepsilon_r'(\omega)$ characterized by an additional α-relaxation frequency ω^{α}, whereby the static dielectric permittivity of the suspension $\varepsilon_r'(0)$ will be higher than that predicted by the classical (diffuse) counterion model. If the characteristic relaxation time of the inner (glycocalyx) layer exceeds that of the diffuse layer, $\tau^{\alpha\,\mathrm{i}} > \tau^{\alpha\,\mathrm{d}}$, the relaxation frequency ω^{α} is lower than that of the diffuse double layer, $\omega^{\alpha\,\mathrm{i}}$

$< \omega^{\alpha d}$, which may provide means of distinguishing between the both polarizations. In case $\tau^{\alpha i} \approx \tau^{\alpha d}$ it would be difficult to distinguish the additional polarization direct from the $\varepsilon_r'(\omega)$ dispersion curves. However, if the biological cells are elongated rod-like particles, the additional relaxation may be distinguished by means of electro-optical measurements of the electro-orientation of the colloid particles. Our electro-optical observations (see Part III) on orientation of *E. coli* cells in the low frequency range of f = 1 Hz -1 kHz (reverse polarity a.c. field) show that at frequencies f < 100 Hz (far below the relaxation frequency of the diffuse double layer which is about 10 kHz) the degree of orientation of the cells obeys peculiar low-frequency modulation that is usually attributed in the literature to permanent dipole orientational mechanism. Since the latter assumption is not realistic for biological cells, and because the diffuse double layer polarization cannot explain the observations, we suggest that the polarization of the cell-glycocalyx is responsible for anomalous electric field induced orientation. Our estimations show that, indeed, the new model of frequency dependent surface conductivity of the inner (polyionic glycocalyx) layer (Schwarz-like model, Eqs. (14) - (15)) is consistent with the experimental observations (see Part III of this thesis).

(ii) A second probable implication of the new model of glycocalyx-polarization is that the static dielectric permittivity of suspension of biological cells $\varepsilon_r'(0)$ would lowers with increasing the field strength because at higher external fields the fixed glycocalix charges could not hold anymore the counterions, alloying efflux of ions normal to the surface. This would diminish the *Schwarz*-like polarization, consequently $\varepsilon_r(0)$. The latter effect could be measured, for instance, by dielectric spectroscopy. Since that effect may come into view at very high fields where membrane electroporation occurs, it could be detected as a change in the electroporation efficiency of the cells. Our experiments on electroporation of *S. pombe* cells (see Part III of this thesis) show that the electroporation efficiencies at E = 1 kV cm^{-1} and E = 1.5 kV cm^{-1} have different frequency dependencies, indicating that the dispersion the induced trans-membrane voltage $U_m(\omega)$ (which is the driving force for electroporation) depends on the field strength. At E = 1.5 kV cm^{-1} the $U_m(\omega)$ dispersion is similar to that predicted by the classical (diffuse) double layer polarization, whereas at fields of E = 1 kV cm^{-1} the dispersion is similar to that of the here proposed polyionic glycocalyx polarization (see Part III).

In view of these experimental evidences we may well conclude that the basic concept of the glycocalyx polarization at low frequencies should be correct.

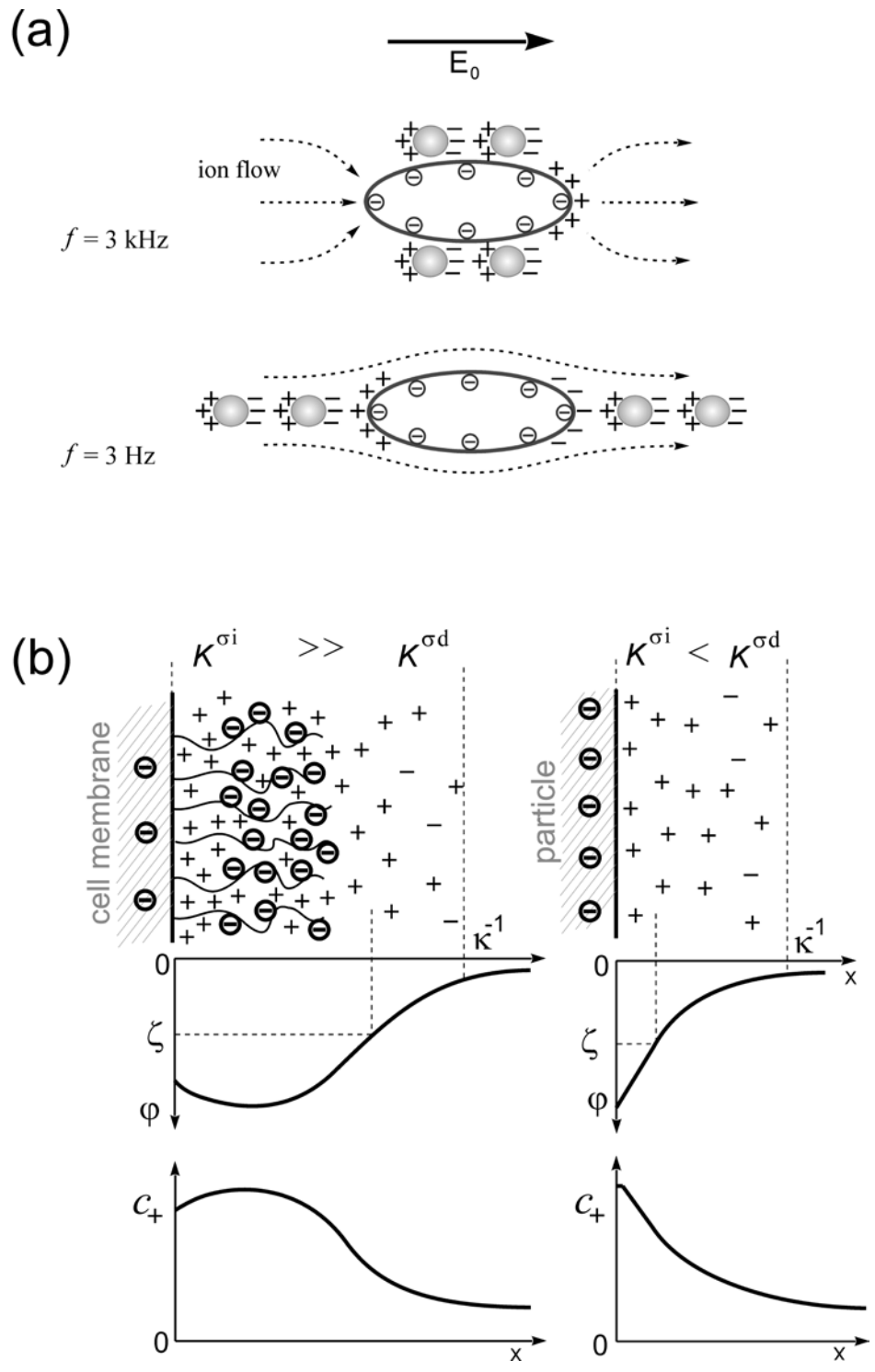

Fig. 14. Schematic representation of the results:
(a) The (low-) frequency dependence of field induced assembly between the polystyrene latex particles and the *S. pombe* yeast cells is caused by the change in the induced dipole moment of the cell.
(b) The suggested charge distribution in the cell glycocalyx layer (left) provides conditions for *Schwarz*-like polarization of the inner counterion layer, whereas the surface charge distribution on the particle surface (right) resides in diffuse-double layer polarization.

Conclusions

The aggregation of the polystyrene latex particles and the *S. pombe* yeast cells in a.c. electric field show characteristic patterns formed by accumulation of particles on the cell “pole-capes” facing the external field. Depending on the frequency of the applied field and the ionic strength of the solving medium, the particles accumulate either on the “equator” of the yeast cells or on the “pole-capes” of the yeast cells. The simulation indicates a *Schwarz*-like polarization of the polyionic glycocalyx of the yeast cells. Two implications of the model measurable in suspensions of biological cells at frequencies below 1 kHz should that the model be correct:

i) An additional dielectric dispersion with lower relaxation frequency and higher amplitude than that of the classical (diffuse) double layer polarization - could be measured either by dielectric spectroscopy or by electro-orientational electrooptic methods (if the biological cells are elongated);

ii) Lowering of the induced dipole moment of the cells with increasing field strength - measurable either by dielectric spectroscopy or by membrane electroporation.

The existence of frequency dependent aggregation of particles either on ‘pole-capes’ or on the ‘equator’ of biological cells, which depend on the conductivity of the suspending medium, might also have important and significant applications in the area of electroporative nanoparticle-based gene/drug delivery.

Appendix

Appendix 1: The dipole coefficient dispersion

The dipole coefficient C^* of a spherical particle of radius a is determined by the conductivity of the sphere and that of the suspending medium as follow:

For a particle with radius a, conductivity K_p and dielectric constant ε_p suspended in an electrolyte solution with conductivity K_e and dielectric constant ε_e, the (complex) dipole coefficient is given by:

$$C^* = \frac{K_p^* - K_e^*}{K_p^* + 2K_e^*} \tag{A1.1}$$

where

$$K_e^* = K_e + i\omega\varepsilon_0\varepsilon_e \tag{A1.2}$$

$$K_p^* = K_p + i\omega\varepsilon_0\varepsilon_p \tag{A1.3}$$

For a particle with surface conductivity K^σ, the total particle conductivity K_p^* in Eq. (A1.1) is replaced by:[24]

$$K_p^* \equiv \left(2K^\sigma / a\right) + K_p^* \tag{A1.4}$$

where K_p^* is given by Eq. (A1.3). In this case Eq. (A1.1) can be rewritten in Debye type relaxation form as:

$$C_p^{*\gamma} = C_p^{\gamma L} + \Delta C_p^\gamma \left(1 - \frac{1}{1 + i\omega\tau_p^\gamma}\right) \tag{A1.5}$$

In Eq. (A1.5), $\Delta C_p^\gamma = C_p^{\gamma H} - C_p^{\gamma L}$, where $C_p^{\gamma H}$ and $C_p^{\gamma L}$ are the low- and the high-frequency limits of $C_p^{*\gamma}(\omega)$, given by:

$$C_p^{\gamma L} = \frac{K_p + \left(2K^\sigma / a\right) - K_e}{K_p + \left(2K^\sigma / a\right) + 2K_e} \tag{A1.6}$$

$$C_p^{\gamma H} = \frac{\varepsilon_p - \varepsilon_e}{\varepsilon_p + 2\varepsilon_e} \tag{A1.7}$$

The characteristic time of the γ-relaxation is given by:

$$\tau_p^{\gamma} = \frac{\varepsilon_0 \varepsilon_{\mathrm{p}} + 2\varepsilon_0 \varepsilon_{\mathrm{e}}}{K_{\mathrm{p}} + \left(2K^{\sigma} / a\right) + 2K_{\mathrm{e}}} \tag{A1.8}$$

The subscripts *p* and *c* are used to denote the latex *particles* and the yeast *cells*, respectively.

For yeast cell with surface conductivity K^{σ}, cell-membrane and cell-inner conductivities (dielectric constants), K_{m} (ε_{m}) and K_{i} (ε_{i}), respectively, the dipole coefficient can be calculated by substituting the total particle conductivity K_{p}^{*} in Eq. (A1.1) by:

$$K_{\mathrm{p}}^{*} \equiv \left(2K^{\sigma} / a\right) + K_{\mathrm{p}}^{*\mathrm{eq}} \tag{A1.9}$$

where $K_{\mathrm{p}}^{*\mathrm{eq}}$ is the conductivity of an "equivalent"-particle, i.e., a homogeneous particle with same complex conductivity as the cell $K_{\mathrm{p}}^{*\mathrm{eq}} = K_{cell}^{*}$, which is given by:

$$K_{\mathrm{p}}^{*\mathrm{eq}} = K_{\mathrm{m}}^{*} \frac{2K_{\mathrm{m}}^{*} + K_{\mathrm{i}}^{*} - 2\nu\left(K_{\mathrm{m}}^{*} - K_{\mathrm{i}}^{*}\right)}{2K_{\mathrm{m}}^{*} + K_{\mathrm{i}}^{*} + \nu\left(K_{\mathrm{m}}^{*} - K_{\mathrm{i}}^{*}\right)} \tag{A1.10}$$

where

$$\nu = \left(1 - \frac{d_{\mathrm{m}}}{a}\right)^3 \cong 1 - 3\frac{d_{\mathrm{m}}}{a} \; ; \qquad d_{\mathrm{m}} \ll a \tag{A1.11}$$

$$K_{\mathrm{m}}^{*} = K_{\mathrm{m}} + i\omega\varepsilon_0\varepsilon_{\mathrm{m}} \tag{A1.12}$$

$$K_{\mathrm{i}}^{*} = K_{\mathrm{i}} + i\omega\varepsilon_0\varepsilon_{\mathrm{i}} \tag{A1.13}$$

(d_{m} is the thickness of the cell membrane) The subscripts 'm' and 'i' denote cell-membrane and cell-inner (cell-core), respectively.

In case of nonconductive membrane $K_{\mathrm{m}} = 0$ and the dipole coefficient of the cell, Eq. (A1.1), can be rewritten in *Debye*-type relaxation form:

$$C_c^{*}(\omega) = C_c^{\beta L} + \Delta C_c^{\beta}\left(1 - \frac{1}{1 + i\omega\tau_c^{\beta}}\right) + \Delta C_c^{\gamma}\left(1 - \frac{1}{1 + i\omega\tau_c^{\gamma}}\right) \tag{A1.14}$$

In Eq. (A1.14), $\Delta C_c^{\beta} = C_c{}^{\beta H} - C_c{}^{\beta L}$ and $\Delta C_c^{\gamma} = C_c{}^{\gamma H} - C_c{}^{\gamma L}$, where $C_p{}^{\beta H}$, $C_p{}^{\beta L}$ $C_p{}^{\gamma H}$ and $C_p{}^{\gamma L}$ are given by:

$$C_c^{\beta L} = \frac{\left(2K^{\sigma}/a\right) - K_{\mathrm{e}}}{\left(2K^{\sigma}/a\right) + 2K_{\mathrm{e}}} \tag{A1.15}$$

$$C_c^{\beta H} = C_c^{\gamma L} = \frac{\left(K_{\mathrm{i}} + \frac{2K^{\sigma}}{a}\right) - \left(K_{\mathrm{e}} + K_{\mathrm{i}}\frac{d_m \varepsilon_{\mathrm{e}}}{a\,\varepsilon_{\mathrm{m}}}\right)}{\left(K_{\mathrm{i}} + \frac{2K^{\sigma}}{a}\right) + 2\left(K_{\mathrm{e}} + K_{\mathrm{i}}\frac{d_m \varepsilon_{\mathrm{e}}}{a\,\varepsilon_{\mathrm{m}}}\right)} \tag{A1.16}$$

$$C_c^{\gamma H} = \frac{\varepsilon_{\mathrm{p}}^{\mathrm{eq}} - \varepsilon_{\mathrm{e}}}{\varepsilon_{\mathrm{p}}^{\mathrm{eq}} + 2\varepsilon_{\mathrm{e}}} \tag{A1.17}$$

where

$$\varepsilon_{\mathrm{p}}^{\mathrm{eq}} = \varepsilon_{\mathrm{m}} \frac{2\varepsilon_{\mathrm{m}} + \varepsilon_{\mathrm{i}} - 2\nu\left(\varepsilon_{\mathrm{m}} - \varepsilon_{\mathrm{i}}\right)}{2\varepsilon_{\mathrm{m}} + \varepsilon_{\mathrm{i}} + \nu\left(\varepsilon_{\mathrm{m}} - \varepsilon_{\mathrm{i}}\right)} \tag{A1.18}$$

In Eq. (A1.14), the characteristic times τ_c^{β} and τ_c^{γ} are given by:

$$\tau_c^{\gamma} = \frac{\varepsilon_0\varepsilon_{\mathrm{i}} + 2\varepsilon_0\varepsilon_{\mathrm{e}}}{K_{\mathrm{i}} + 2K_{\mathrm{e}} + \left(2K^{\sigma}/a\right)} \tag{A1.19}$$

$$\tau_c^{\beta} = \varepsilon_0\varepsilon_{\mathrm{m}} \frac{a}{d_m}\left(\frac{1}{K_{\mathrm{i}}} + \frac{1}{\left(2K^{\sigma}/a\right) + 2K_{\mathrm{e}}}\right) \tag{A1.20}$$

If the membrane is thin compared to the cell radius ($d_m << a$), Eq. (A1.19) can be approximated by:

$$C_c^{\gamma H} \approx \frac{\varepsilon_{\mathrm{i}} - \varepsilon_{\mathrm{e}}}{\varepsilon_{\mathrm{i}} + 2\varepsilon_{\mathrm{e}}} \tag{A1.21}$$

As mentioned in the main text, in the kilohertz frequency range there is another (low-frequency) dielectric dispersion caused by the polarization of the electric double layer of the suspended colloid particles, which is here specified as α-dispersion, $C^{*\alpha} = C^{*\alpha}(\omega)$. Thus the total dispersion (α, β and γ dispersions) of the dipole coefficient of a latex particle (*p*) and a yeast cell (*c*) can be expressed as:

$$C_p^*(\omega) = C_p^{*\alpha}(\omega) + \Delta C_p^{\gamma}\left(1 - \frac{1}{1 + i\omega\tau_p^{\gamma}}\right) \tag{A1.22}$$

$$C_c^*(\omega) = C_c^{*\alpha}(\omega) + \Delta C_c^{\beta}\left(1 - \frac{1}{1 + i\omega\tau_c^{\beta}}\right) + \Delta C_{cell}^{\gamma}\left(1 - \frac{1}{1 + i\omega\tau_c^{\gamma}}\right) \tag{A1.23}$$

where $C^{*\alpha}(\omega)$ is given by Eq. (6) of the main text.

Appendix 2: The time-dependent dielectrophoretic forces

The field induced dielectrophoretic force between particle *i* and *j*, as well as, between particle *i* and cell *c*, is deduced by taking the negative gradient of the (time-dependent) dielectrophoretic energy of interaction, Eq. (27) and Eq. (29), yielding the (dimensionless) expressions:

$$\mathbf{f}_{ij}^{diel} = 2\frac{C_p{}^2 \cos^2\left(\hat{\omega}\hat{t} + \psi_p\right)}{\hat{r}_{ij}^{\,4}}\left[\left(3\cos^2\theta_{ij} - 1\right)\mathbf{e}_{\mathbf{r}_{ij}} + \left(\sin 2\theta_{ij}\right)\mathbf{e}_{\boldsymbol{\theta}_{ij}}\right] \tag{A2.1}$$

$$\mathbf{f}_{ic}^{diel} = 2\left(\frac{a_c^{\text{eff}}}{a_p}\right)^3 \frac{C_c C_p \cos\left(\hat{\omega}\hat{t} + \psi_c\right)\cos\left(\hat{\omega}\hat{t} + \psi_p\right)}{\hat{r}_{ic}^{\,4}} \times \left[\left(3\cos^2\theta_{ic} - 1\right)\mathbf{e}_{\mathbf{r}_{ic}} + \left(\sin 2\theta_{ic}\right)\mathbf{e}_{\boldsymbol{\theta}_{ic}}\right] \tag{A2.2}$$

where $\hat{\omega} = \omega t_0$. ω and t_0 are the angular frequency of the electric field and the natural time-unit (Eq. (37)of the main text), respectively. The dimensionless forces and distances are scaled to F_0 and a_p, respectivelly, i.e., $\mathbf{f} = \mathbf{F} / F_0$ and $\hat{r} = r / a_p$, where F_0 is given by Eq. (35) of the main text.

Appendix 3: The repulsive force factors

The factors $A\left(\hat{\zeta}_p\right)$ and $B\left(\hat{\zeta}_p, \hat{\zeta}_c\right)$ in the expressions for the *particle–particle* and *particle–cell* repulsive forces, Eq. (39) and Eq. (40) of the main text, are given by:

$$A\left(\hat{\zeta}_p\right) = \frac{16\varepsilon_0\varepsilon_e(k_B T/e)^2}{F_0}\tanh^2\left(z\hat{\zeta}_p/4\right)$$
$$B\left(\hat{\zeta}_p,\hat{\zeta}_c\right) = \frac{16\varepsilon_0\varepsilon_e(k_B T/e)^2}{F_0}\tanh\left(z\hat{\zeta}_p/4\right)\ \tanh\left(z\hat{\zeta}_c/4\right) \qquad \text{(A3.1)}$$

The electrokinetic potentials ζ_p and ζ_c in Eq. (A3.1) are taken as an approximation for the surface potentials φ_0, i.e., $\varphi_{0p} \approx \zeta_p$ for the *i*th latex particle and $\varphi_{0c} \approx \zeta_c$ for the yeast cell. The scaled center-to-center distance $\hat{r}_{ic}^0$ in Eq. (40) of the text is approximated by:

$$\hat{r}_{ic}^0 = \frac{r_{ic}^0}{a_p} \cong 1 + \sqrt{\left(\frac{a_c}{a_p}\right)^2\cos^2\theta_{ic} + \left(\frac{b_c}{a_p}\right)^2\sin^2\theta_{ic}} \qquad \text{(A3.2)}$$

Recall that $\hat{r}_{ic}^0$ is the (scaled) center-to-center distance at particle contract, that is, when the particle *i* contacts the yeast cell *c*. The cell is approximated as prolate spheroid of revolution, having polar and equatorial radii a_c and b_c, respectively. θ_{ic} is the angle between $\mathbf{r}_{ic}$ and $\mathbf{e}_x$ (see Fig. 7).

Appendix 4: The electrophoretic mobilities.

The electrophoretic mobility of a spherical latex particle *p*, or yeast cell (*c*), can be expressed by the corresponding particle (cell) ζ-potential, $\hat{\mu} = \hat{\mu}\left(\hat{\zeta}\right)$, using the connection deduced by O'Brien and Hunter,[29] which can be expressed in dimensionless form as:

$$\hat{\mu}_{p(c)} = \mu_{p(c)}\frac{\eta e}{\varepsilon_0\varepsilon_e k_B T} = \hat{\zeta}_{p(c)} - \frac{\delta_{p,c}}{1+\delta_{p,c}}\left(\hat{\zeta}_{p(c)} - \frac{2\ln 2}{z}\left[1-\exp\left(-z\hat{\zeta}_{p(c)}\right)\right]\right) \qquad \text{(A4.1)}$$

where

$$\delta_{p(c)} = \frac{2}{\kappa a_{p(c)}}\left(1+\frac{3M}{z^2}\right)\exp\left(\frac{z\hat{\zeta}_{p(c)}}{2}\right); \qquad \text{(A4.2)}$$

$$M = \frac{2\varepsilon_0\varepsilon_e}{3\eta D}\left(\frac{k_B T}{e}\right)^2; \qquad \hat{\zeta} = \frac{\zeta e}{k_B T} \qquad \text{(A4.3)}$$

In Eqs. (A4.1) - (A4.3), $\hat{\zeta}_{p\,(c)}$ is the scaled electrokinetic potential and $a_{p,(c)}$ the particle (cell) radius. The effective radius of the *S. pombe* yeast cells is calculated as $a_c^{eff} = (a_c \times b_c^2)^{1/3}$, where a_c and b_c are the polar and equatorial radii , respectively. Recall that the shape of the yeast cell is approximated by prolate spheroid of revolution oriented parallel to the applied field, see Fig. 7.

Appendix 5: Three identical particles in uniform electric field.

In the example given in Fig. 8, the trajectories $\mathbf{r}_i(t)$ of the three identical spheres of radius a are calculated by integrating the equations of motion applied for time-averaged forces:

$$\frac{d\hat{\mathbf{r}}_i}{d\hat{t}} = \sum_{j\,(\neq i)} \overline{\mathbf{f}_{ij}^{del}} + \sum_{j\,(\neq i)} \overline{\mathbf{f}_{ij}^{rep}} \quad ; \quad (i,\, j = 1 \ldots 3) \tag{A5.4}$$

where the scaled dielectrophoretic force $\overline{\mathbf{f}_{ij}^{diel}}$ is expressed by Eq. (33) of the main text.

In this example, only a hard-core repulsive force is considered:

$$\overline{\mathbf{f}_{ij}^{rep}} = \exp\left(-100\frac{\hat{r}_{ij}-2}{2}\right)\cdot\left(-\mathbf{e}_{\mathbf{r}_{ij}}\right) \qquad ; \qquad \hat{r}_{ij} = r_{ij}\,/\,a \tag{A5.5}$$

Notes and references

[1] E. Neumann, and K. Rosenheck, *Permeability changes induced by electric impulses in vesicular membrane,* J.Membrane Biol. **10**, 279-290 (1972).

[2] E. Neumann, M. Shaefer-Ridder, Y. Wang and P. H. Hofschneider. *Gene Transfer into mouse lyoma cells by electroporation in high electric fields.* EMBO J. **1**, 841-845 (1992).

[3] Zimmerman, U. *Electric field-mediated fusion and related phenomena*. Bichim. Biophys. Acta. **694**, 227 (1992).

[4] Ristenpart W. D., Aksay I. A., and Saville D. A., *Electrically guided Assembly of Planar Superlattices in Binary Colloid Suspension*, Phys. Rev. Let., 128303 (2003).

[5] Mantegazza F., Caggioni M., Jimenez M. L.Bellini T., *Anomalous field-induced particle orientation in dilute mixtures of charged rod-like and spherical colloids*, Nature Physics, **1,** 103 (2005).

[6] Giner, V., Sancho, M., Lee, R. S., Martinez, G., and Pething, R., J. Phys. D, **32**, 1182 (1999).

[7] Schwarz, G., Saito, M., and Schwan, H. P., *On the orientation of nonspherical particles in an alternating electric field*. J. Chem. Phys. **43**, 3562-3569, (1965).

[8] Saito, M., Schwan, H. P., and Schwarz, G., *Response of nonspherical biological particles to alternating electric fields*. Biophys. J., **6**, 313-327 (1966).

[9] Eigen, M.,and Schwarz, G., Z. physik. Chem. [N. F.] **4** (5/6) 380 (1955).

[10] Mandel, M., Mol.Phys. **4** 489 (1961).

[11] Neumann, E. and Katchalski, A., Proc. Natl. Acad. Sci. U.S.A. **69** 993 (1972).

[12] H. P. Schwan, G. Schwarz., Maczuk, and H. Pauly, J. Phys. Chem. **66**, 2626 (1962).

[13] Maxwell, J. C., *Treatise on electricity and Magnetism*, 1873 (Dover, New York, 1954).

[14] Wagner K. W., *Arch. Elect.* **2**, 37 (1914).

[15] Schwarz, H. G., *J. Phys. Chem.* **66**, 2626 (1962).

[16] P. N. Sen, *Appl. Phys. Lett*. **39,** 667 (1981).

[17] J. M. Schurr, J. Phys. Chem. **68,** 2407 (1964).

[18] Dukhin, S. S. and Shilov, V. N., Dielectric Phenomena and the Double Layer in Disperse Systems and Polyelectrolytes (Halsted, New York, 1974).

[19] Dukhin, S. S., and Derjaguin, B. V., in *Surface and Colloid Science*, (Wiley, New York, 1974), Vol. 7.

[20] Fixman, M., J. Chem. Phys. **72**, 5177 (1980).

[21] Delacey, E. H. B. and White, L. R., J. Chem. Soc. , Faraday Trans. 2, **77**, 2007 (1981).

[22] Heinrich, R., M. Gaestel, and R. Glaser. 1982. The electric potential profile across the erythrocyte membrane. J. Theor. Biol. 96:211-231.

[23] Neumann, E., *The relaxation hysteresis of membrane electroporation*, in: E. Neumann, A.E. Sowers, C. Jordan (Eds.), *Electroporation and electrofusion in cell biology*, Plenum, New York, 1989, pp. 61-82.

[24] O'Konski, C. T., J. Phys. Chem., **64**, 605 (1960).

[25] Lyklema, J., *Fundamentals of Interfaces and Colloid Science*, Vol. II, Chap. 3, 4, Academic Press, New York (1995).

[26] Note that different authors use different sign conventions writing complex quantity, $a^* = a' + ia''$ or $a^* = a' - ia''$, and alternating fields, $E^* = E_0 \exp(i\omega t)$ and $E^* = E_0 \cdot \exp(-i\omega t)$. The expressions, Eq. (6) and Eq. (7), cited here, [25], are rewritten for the case of counterclockwise complex field vector rotation, $E_0 \cdot \exp(i\omega t)$.

[27] Lyklema, J., Minor, M., Colloid Surf. A, **140**, 33 (1998).

[28] Stratton, J. A., Electromagnetic Theory, (McGraw-Hill, Inc, 1941, pp. 135-137).

[29] O'Brien, R. W. and R. J. Hunter R. J., *Can. J. Chem.,* **59**, 1878 (1981).

[30] Bell, G. M., Levine, S., and McCartney, L. N., J. Colloid Interface Sci., **33**, 335 (1970).

[31] Schnitzer, J. E., Yale J. Biol. Med., **61**, 427 (1988).

[32] Usai, C., Robello, M., Gambale, F., Marchetti, C., J. Memb. Biol. **82**, 15 (1984).

[33] Feinstein, M. B., Spero, L., Felsenfield, H., FEBS Lett., **6**, 245 (1970).

[34] McDaniel, R.V., McIntosh, T. J., Biophys. J., **49**, 94 (1986).

Part III

Electroorientation and electroporation of *E. coli* bacteria and *S. pombe* yeast cells in external a.c. electric fields

Abstract

The new (*Schwarz*-like) flow-polarization model of the polyionic glycocalyx shell of the yeast cells is used to describe the electro-orientation and electroporation of *E. coli* and *S. pombe* cells, respectively, induced by low-frequency ($f \leq 3$kHz) a.c. electric fields (reverse polarity square-wave).

The orientation of the *E. coli* cells in the low-field intensity range $E = 20 \ldots 150$ V cm^{-1}, measured by static 90°-light scattering, shows a peculiar modulation at frequencies $f \leq 10$ Hz which is not consistent with the classical (diffuse) double layer polarization model, but agrees with new (Schwarz-like) flow-polarization (proposed in Part II).

The electroporation efficiency of *S. pombe* yeast cells shows a frequency dependence in the same frequency range $f = 3$Hz … 3 kHz. At field intensity amplitude $E = 1$ kV cm^{-1}, the profile of the dispersion curve correlates with the new flow-polarization model of the polyionic *glycocalyx* shell. At $E = 1.5$ kV cm^{-1}, the dispersion curve can be described by the classical (diffuse) double layer polarization model.

Thus, both the low-frequency data of the electro-orientation of the *E. coli* cells and the electroporation of the *S. pombe* yeast cells are consistent with the higher ionic flow-polarization residing in the particular ionic structure of the cell-glycocalyx.

1. Electroorientation of E. coli cells in the frequency range 0 – 2 kHz

1.1 Materials and methods

The principal setup of the electro-optical light-scattering detection system is shown in Fig. 1. The apparatus for electro-optical observations is the "field-jump" relaxation spectrometer described in Part (I) of this thesis. For the purposes of this investigation, the high-voltage cable discharge technique was not used, and the low-intensity (up to 160 V/cm) long durative (several seconds) electric fields were supplied using a function waveform generator and an (home-made) amplifier capable of delivering voltages of up to 200 V in the range from d.c. up to 1MHz. The temperature variations due to the applied fields were < 3°C in all cases.

E. coli XL-1-blue strain was used: recA1, end A1, gyrA96, rhi-1, hsd R-17, supE44, relA1, lac[F' pro AB, lacIq Z M15, Tn10(tet)r]. E. coli strain was grown in LB (Lutria Bertani) medium-yeast extract, 0.5%; bactotriptone, 1% from Difco and 1% NaCl. Single colony of *E. coli* was grown overnight to mid-log phase at a specific optical density $OD_{600\ nm}$ = 0.4. The E. coli cells are elongated rod-like particles of length 2 μm and axial ratio of 3.

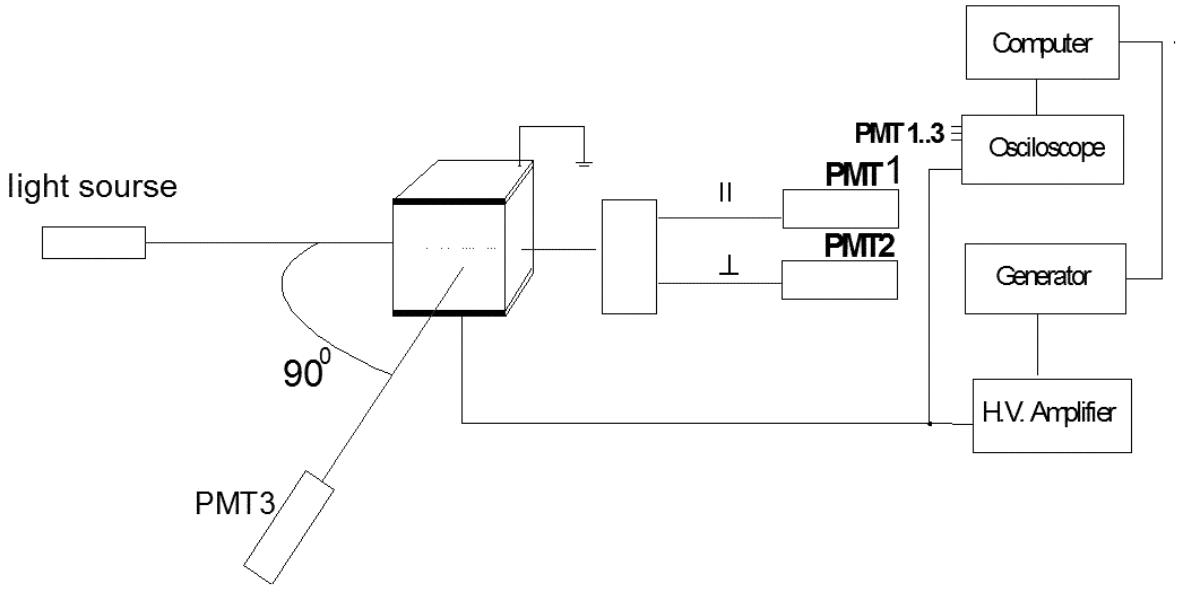

Fig. 1.1 Principal scheme of the electro-optical light scattering measurements.

1.2. Results and discussion

Fig. 1.2(a) shows a typical electro-optical response of *E.coli* cells induced by square-wave low-frequency (up to 1 kHz) electric field with constant amplitude. In the first second of the field onset the frequency is f = 1 kHz followed by a "d.c." frequency of f = 1 Hz and f = 6 Hz. The amplitude of the electro-optical effect reflects changes in the degree of orientation of the cells. It can be seen that, with lowering frequency the amplitude of the electro-optical effect decreases. When the electric field changes polarity, the electro-optical response peaks to the higher level (since the electric field jump is described by harmonics of higher frequencies) and relaxes again to the lower d.c.-amplitude. The electro-optical response is measured by 90° (static) light scattering, see Fig. 1.2(a). Similar modulations in the electro-optical responses is observed by measuring the turbidity dichroism (0° static light scattering, see the scheme in Fig. 1.1), indicating that the modulation of the scattered light reflects changes in the degree of orientation of the *E. coli* cells.

It should be noted that, the shape of the modulation of the electro-optical responses in the low-frequency range 1 Hz $\leq f \leq$ 1 kHz is usually attributed to electro-orientation due to permanent dipole moment of the elongated particles. The linear-like field dependence of the electro-optical effect (Fig. 1.2(b)) is also misinterpreted as being due to permanent dipole. Here we show that the new polarization mechanism proposed in Part (II) (polarization of the cell-glycocalyx in the light of the *Schwarz*'s model) may rationalize the experimental observations without the need of the unrealistic (especially for biological cells) permanent dipole explanation.

In order to describe the electro-orientation of the *E. coli* cells one needs to estimate the driving force for the orientation, that is, the potential energy U of interaction of the *E. coli* particle with the externally applied electric field. The potential energy of interaction depends on the induced dipole of the particle, which is governed by the electric double layer (EDL) polarization of the cells. The analytical expressions for the induced dipole moment due to the EDL polarization given in the literature (as that for instance used in Part II of this thesis) consider spherical particle with thin electric double layer, $\kappa a >> 1$. The expressions are usually calculated by solving the frequency dependent electro-diffusion equations. Since these equations written in spheroidal coordinates do not separate, [1] no theoretical results exist for the low-frequency induced dipole moment of spheroidal particle.

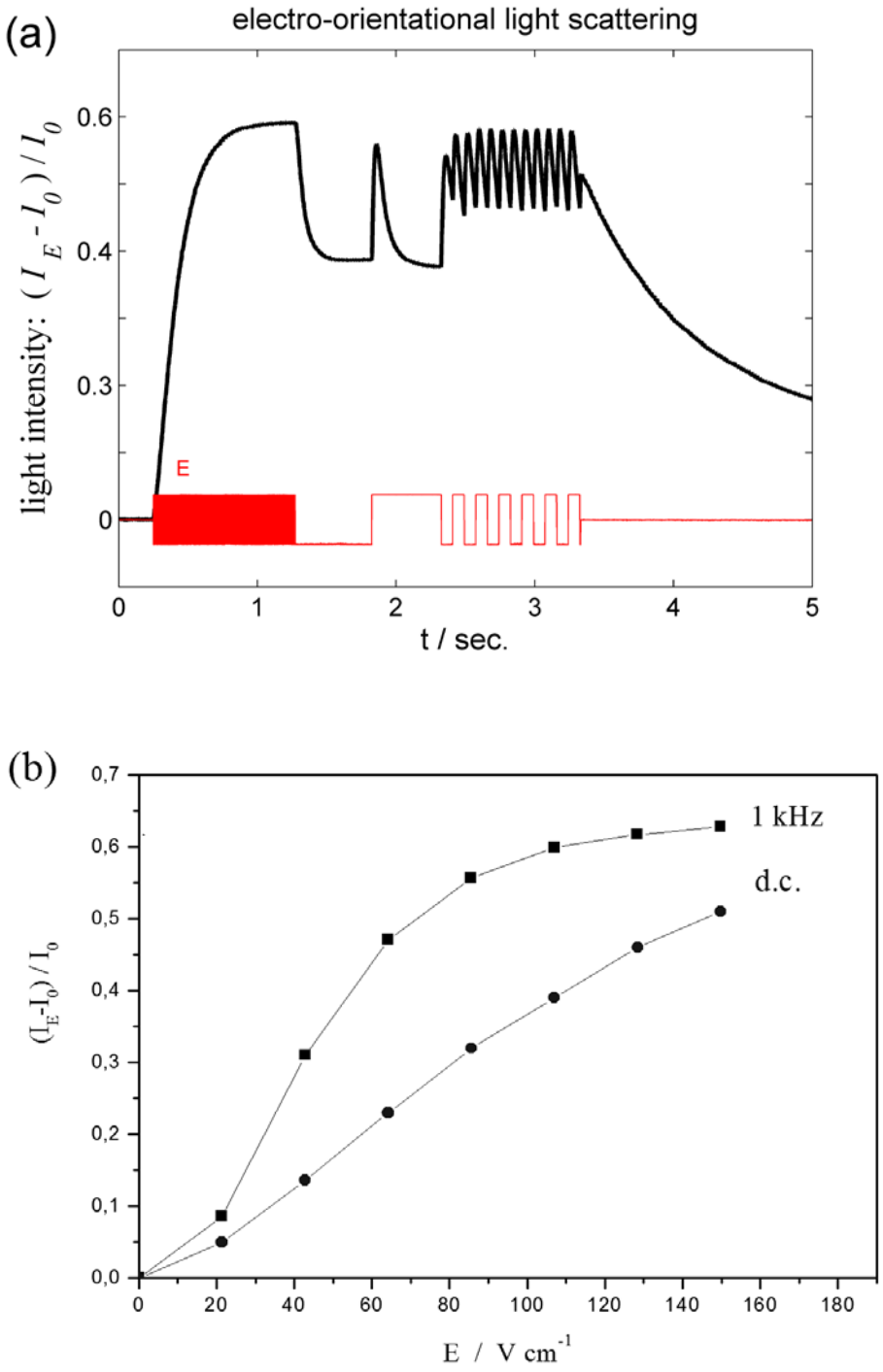

Fig. 1.2 (a) The electric field induced changes in the intensity of the (90°) scattered light (λ = 465 nm) of suspension of *E. coli* cells (10^8 cells/ml suspended in week NaCl solution with conductivity of $K_e \approx 7 \times 10^{-4}$ S m^{-1}, pH ≈ 6) and the field dependence the electrooptical effect (b) measured at frequency f = 0 Hz (•) and f = 1 kHz (■). The intensity of the electric field in (a) is E = 110 V/cm (reverse pulse field with frequency f = 1 kHz, f = 1 Hz and f = 6 Hz).

In order to sidestep this problem by estimating the dielectric properties of suspensions of spheroid colloid particles, Grosse at al. [1] used another method which relates the dielectric properties of the suspension to the energy stored in the system. They deduced expressions for the dipole coefficient of prolate ellipsoidal particle oriented parallel (||) and perpendicular (⊥) to the direction of the externally applied electric field in the low (0) and high (∞) frequency limits of the α-dispersion, $C^0_{\mathrm{II}(\perp)}$ and $C^\infty_{\mathrm{II}(\perp)}$, respectively. They also give expressions for the (weighted average) characteristic time of the α-dispersion of the suspended particles in the two cases of orientation, τ_{II} and $\tau_\perp$, respectively. The expressions for $C^0_{\mathrm{II}(\perp)}$, $C^\infty_{\mathrm{II}(\perp)}$ and $\tau_{\mathrm{II}(\perp)}$ are here summarized in the Appendix. With these expressions we can calculate the frequency dependence of the dipole coefficient $C^*(\omega)$ using a simple Debye-type dispersion (single time constant relaxation) by:

$$C^*_{\|\perp}(\omega) = C^\infty_{\|\perp} + (C^0_{\|\perp} - C^\infty_{\|\perp})\frac{1}{1+i\omega\tau_{\|\perp}} \qquad (1)$$

where $C^0_{\mathrm{II}(\perp)}$, $C^\infty_{\mathrm{II}(\perp)}$ and $\tau_{\mathrm{II}(\perp)}$ depend on the surface conductivity K^σ (see Appendix).

As mentioned in Part II, the α-dispersion (EDL polarization) has a frequency dependence that does not correspond to a single time constant relaxation, being substantially broader. By applying Eq. (1) for the case of equal semi-axes (by taking $a = b$) and comparing the resulting $C^*(\omega)$ with that given in the literature for spherical particle (and making some rationalizations) we found that the broader frequency dispersion of the dipole coefficient can be expressed by:

$$C^*_{\|\perp}(\omega) = C^\infty_{\|\perp} + (C^0_{\|\perp} - C^\infty_{\|\perp})\frac{1+X_{\|\perp}\sqrt{i\omega\tau_{\|\perp}}}{1+X_{\|\perp}\sqrt{i\omega\tau_{\|\perp}}+i\omega\tau_{\|\perp}} \qquad (2)$$

where $\tau_{\|(\perp)}$ is the single (weighted average) relaxation time of Eq. (1). The factor $X_{\|,\perp}$ (given in the Appendix) depends on the same parameters as Eq. (1): the surface conductivity K^σ and the shape of the particle (determined by the length of the semi-axes a and b). If $X_{\|,\perp}= 0$ Eq. (2) transforms to Eq. (1). In general, both Eq. (1) and Eq. (2) apply, since the low- and high-frequency values of the dipole coefficient, $C^0_{\mathrm{II}(\perp)}$ and $C^\infty_{\mathrm{II}(\perp)}$, respectively, are the same for both equations. It is only the shape of the frequency α-dispersion that is different, being substantially broader by using Eq. (2). In the calculation bellow we used the latter equation.

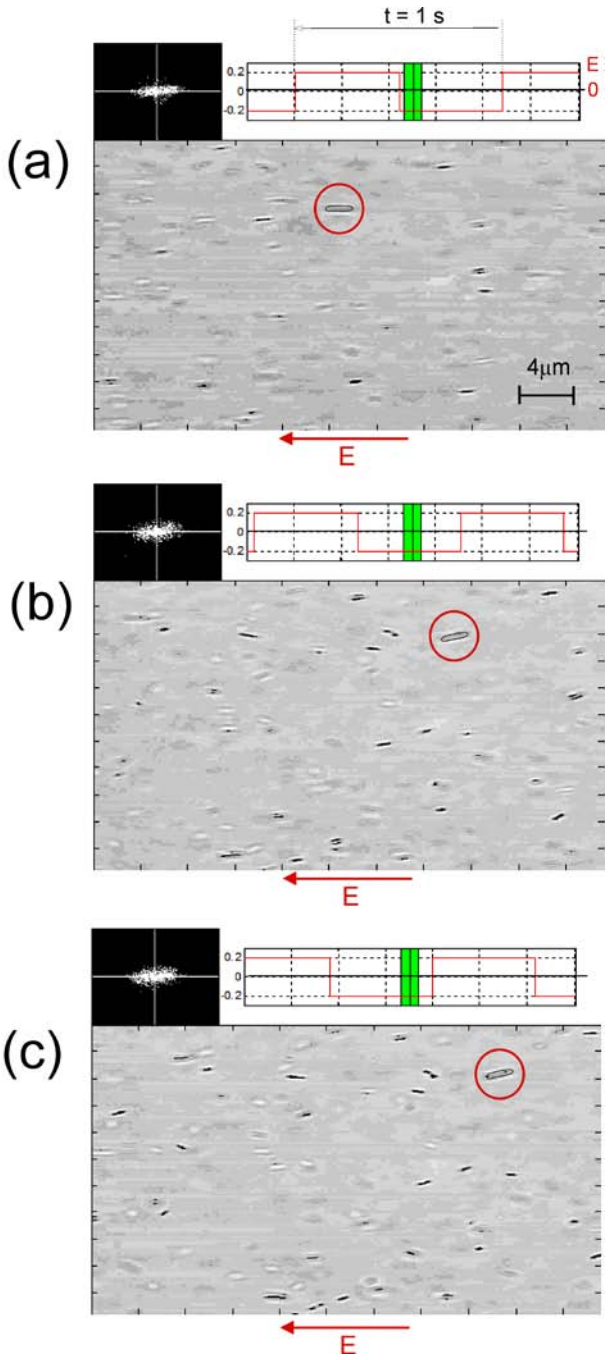

Fig. 1.3. Optical microscope images of the *E. coli* cells suspended in low conductive medium (NaCl solution, $K_e \approx 7 \times 10^{-4}$ S m^{-1}, pH ≈ 6) exposed to electric field with intensity E = 10 V/cm and frequency f = 1 Hz (square-wave field). The field is applied in the horizontal direction. The images are taken at t ≈ 0.05 s (a), 0.25 s (b) and 0.4 s (c) after a reverse in the field direction. The image of the marked (with circle) *E. coli* cell is contoured in black for better contrast. The black squares at the top of the figures are Fourier images of the pictures, indicating the orientation of the *E. coli* cells.

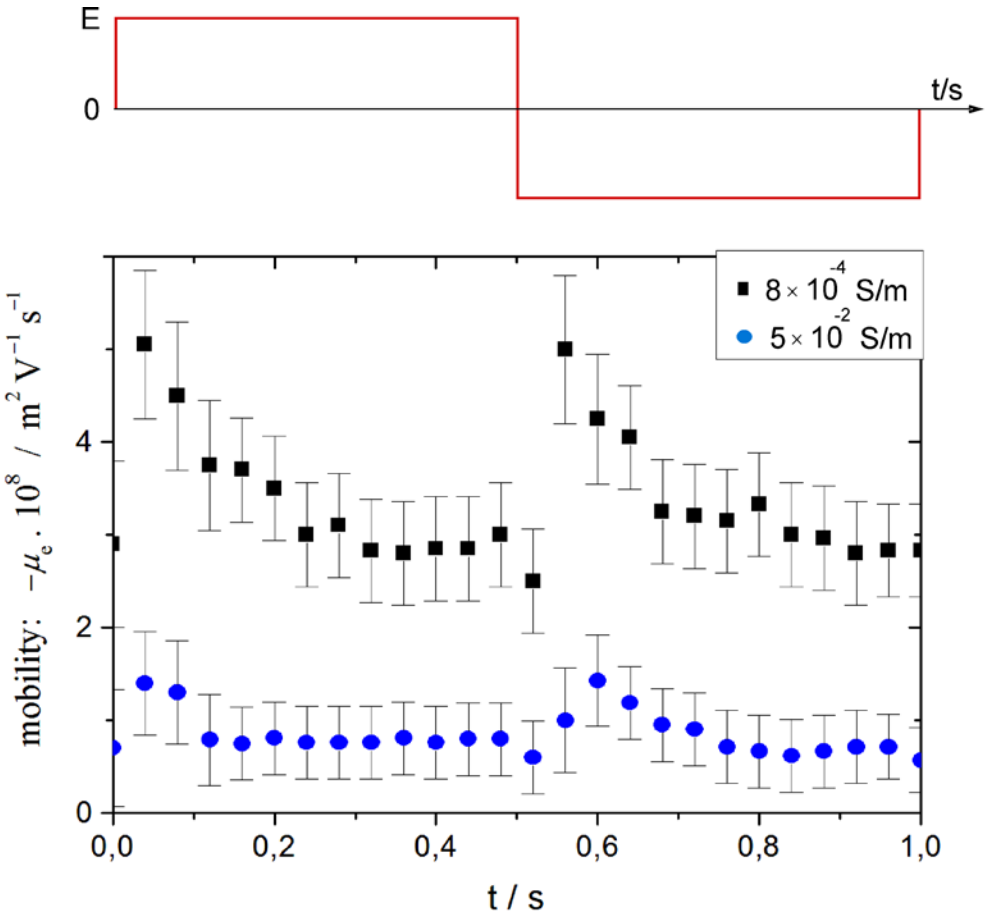

Fig. 1.4 The average electrophoretic mobility of *E. coli* cells measured in the direction of the electric field E (square-wave reverse polarity field; E = 10 V/cm, f = 1 Hz) at two conductivities of the suspending medium: $K_e = 8 \times 10^{-4}$ S m^{-1} (■) and $K_e = 5 \times 10^{-2}$ S m^{-1} (•). From the average electrophoretic mobility $\mu_e = 3 \times 10^{-8}$ m^2 V^{-1} s^{-1} (at $K_e = 8 \times 10^{-4}$ S m^{-1} is), by applying the theoretical model for the electrophoretic motion of a cylinder, we obtain the electro-kinetic potential $\varsigma = -40$ mV, which is used to estimate the induced dipole moment of the *E. coli* cells (see Fig. 1.3).

In Eq. (1) and Eq. (2), the unknown parameter is the surface conductivity K^σ of the particle. K^σ has contributions owing to the diffuse-layer charge outside the plane of shear, $K^{\sigma d}$, and to the charge in the inner layer $K^{\sigma i}$, $K^\sigma = K^{\sigma d} + K^{\sigma i}$ (see Eq. (10) of Part II). Applying the equations for the surface conductivity of the classical (diffuse) double layer (Eq. 12 of Part II) together with the new model of frequency dependent surface conductivity (Eq. (14) of Part II), we obtain the expressions for the surface conductivity K^σ in the case of the moth models :

$$K^{\sigma} = K_{\mathrm{e}} \frac{2}{\kappa}\left(1+\frac{3M}{z^2}\right)\left[\cosh\left(\frac{ze\zeta}{2k_BT}\right)-1\right](1+\Theta) \tag{3}$$

for the classical (diffuse) double layer polarization, and

$$K^{\sigma} = K_{\mathrm{e}} \frac{2}{\kappa}\left(1+\frac{3M}{z^2}\right)\left[\cosh\left(\frac{ze\zeta}{2k_BT}\right)-1\right]\left(1+\frac{i\omega\tau^{\alpha \mathrm{i}}}{1+i\omega\tau^{\alpha \mathrm{i}}}\Theta\right) \tag{4}$$

for the new (*Schwarz*-like) model of the polyionic glycocalyx polarization.

In Eq. (3) and Eq. (4), K_{e} is the conductivity of the suspending medium, κ is Debye - Hückel parameter given by Eq. (1) of Part II, and M is the relative contribution of electro-osmosis to the surface conductivity. For symmetrical electrolytes M is given by Eq. (13) of Part II. According to the classical model (Eq. (3)), the surface conductivity K^{σ} is frequency independent, whereas in the new (*Schwarz*-like) model K^{σ} is frequency dependent with characteristic time $\tau^{\alpha \mathrm{i}}$, see Eq. (4). In both cases, the magnitude of the surface conductivity K^{σ} is determined by two parameters: the electro-kinetic potential ζ (obtained experimentally, see Fig. 1.4) and the ratio $\Theta = K^{\sigma \mathrm{i}} / K^{\sigma \mathrm{d}}$ between the surface conductivity $K^{\sigma \mathrm{i}}$ of the inner counterion layer and $K^{\sigma \mathrm{d}}$ of the diffuse layer (outside the plane of share). Since in our case ζ = – 40 mV (see Fig. 1.4), the parameter that remains unknown is Θ.

In Eq. (4), the parameter $\tau_{\mathrm{II}}^{\mathrm{i}}$ is the characteristic relaxation time of a cell oriented parallel to the field. Recall that the 'transverse' relaxation time $\tau_{\perp}^{\mathrm{i}}$ is expressed by $\tau_{\mathrm{II}}^{\mathrm{i}}$ via the relationship $\tau_{\perp}^{\mathrm{i}} = (b/a) \times \tau_{\mathrm{II}}^{\mathrm{i}}$, where a and b are the semi- major and the minor axes of the *E.coli* cell, respectively.

The induced dipole moment of an *E. coli* cell is calculated using the polarizability $\alpha^{*}(\omega) = 3\varepsilon_0\varepsilon_{\mathrm{e}}V_{cell}\cdot C^{*}(\omega)$ of the cell, where V_{cell} and $C^{*}(\omega)$ are the volume and the dipole coefficient of the cell, respectively. Since in our experiment the electric field $E(t)$ is defined function of the time, and since the dipole coefficient is expressed as an frequency-domain function $C(i\omega)$ (by Eq. (1) or Eq. (2)), the induced dipole moment (in the time-domain) is given by:

$$\begin{aligned} p_{ind}(t) &= \mathcal{L}^{-1}\left\{\alpha(i\omega)\cdot\mathcal{L}\left[E(t)\right]\right\} = \mathcal{L}^{-1}\left\{\alpha(i\omega)\right\} * \mathcal{L}^{-1}\left\{\mathcal{L}\left[E(t)\right]\right\} \\ &= \mathcal{L}^{-1}\left\{\alpha(i\omega)\right\} * E(t) \end{aligned} \tag{5}$$

where $\mathcal{L}$ and $\mathcal{L}^{-1}$ are the Laplace and the inverse Laplace transforms, respectively, and f∗g being the convolution integral of functions f(t) and g(t). Substituting $\alpha(i\omega) = 3\varepsilon_0\varepsilon_e V_{cell} \cdot C(i\omega)$ into Eq. (5) yields:

$$p_{ind}(t) = 3\varepsilon_0\varepsilon_e V_{cell} \cdot \int_0^t \mathcal{L}^{-1}\{C(i\omega)\}(t-\theta) \cdot E(\theta) \cdot d\theta \tag{6}$$

Applying now the (Debye-) approximation for C($i\omega$) given by Eq. (1) we obtained the induced dipole of the particles in the case of parallel (p_{II}^{ind}) and perpendicular ($p_{\perp}^{ind}$) orientation in respect to the field:

$$p_{\|,\perp}^{ind}(t) = 3\varepsilon_0\varepsilon_e V_{cell} C_{\|,\perp}^{\infty} \cdot E(t) \quad + \\ 3\varepsilon_0\varepsilon_e V_{cell} \cdot \left[C_{\|,\perp}^{0} - C_{\|,\perp}^{\infty}\right] \frac{\exp\left(-t/\tau_{\|,\perp}\right)}{\tau_{\|,\perp}} \int_0^t \exp\left(\frac{\theta}{\tau_{\|,\perp}}\right) E(\theta)\, d\theta \tag{7}$$

In our calculations we have used the exact expression for C($i\omega$) given by Eq. (2), whereby $\mathcal{L}^{-1}\{$ C($i\omega$)$\}$ is calculated numerically.

The potential energy is calculated by:

$$U_{\|,\perp}(t) = p_{\|,\perp}^{ind}(t) \cdot E(t) \tag{8}$$

The difference between the parallel and perpendicular particle orientation is given by:

$$\Delta U(t) = U_{\|}(t) - U_{\perp}(t) \quad = \left[p_{\|}^{ind}(t) - p_{\perp}^{ind}(t)\right] \cdot E(t) \tag{9}$$

Thus, by varying the optimization parameters Θ and (for the case of the new, glycocalyx polarization model) τ_{II}^{i}, and comparing the magnitude of the modulation in $\Delta U(t)$ with that of the measured $[I_E(t) - I_0]/\ I_0$ electro-optical effect, we obtain the approximate values $\Theta = K^{\sigma i} / K^{\sigma d} \approx 12$ and $\tau_{II}^{i} \approx 10^{-2}$ s. The results are shown in Fig. 1.5, Fig. 1.6 and Fig. 1.7. The modulation in the electro-optical effect of *E. coli* cells cannot be rationalized in the view of the classical model of diffuse double layer polarization, whereas the new model of *Schwarz*-like polarization of the cell-glycocalyx agrees with the experiment.

It should be noted that the classical model predicts small modulation in $\Delta U(t)$ too, however the magnitude and the relaxation time of this modulation are very small. For example, even at (unrealistic) Θ-values of $\Theta > 200$, the modulation magnitude is less than 5% of the maximum amplitude, whereas that of the measured electro-optical effect is about 30%. Also the

relaxation time of the (classical model) modulation is much smaller ($\tau_{II}^{i} \approx 10^{-4}$ s) than that of the experimental data ($\tau_{II}^{i} < 10^{-2}$ s). Additionally, the time dependence of the electrophoretic mobility shows a peak-like modulation (see Fig. 1.4), indicating frequency dispersion below 100 Hz which cannot be explained in the view of the classical (diffuse) double layer polarization. For this frequency dependence of the electrophoretic mobility more elaborated models, including the new (*Schwarz*-like) polyionic glycocalyx polarization, are needed.

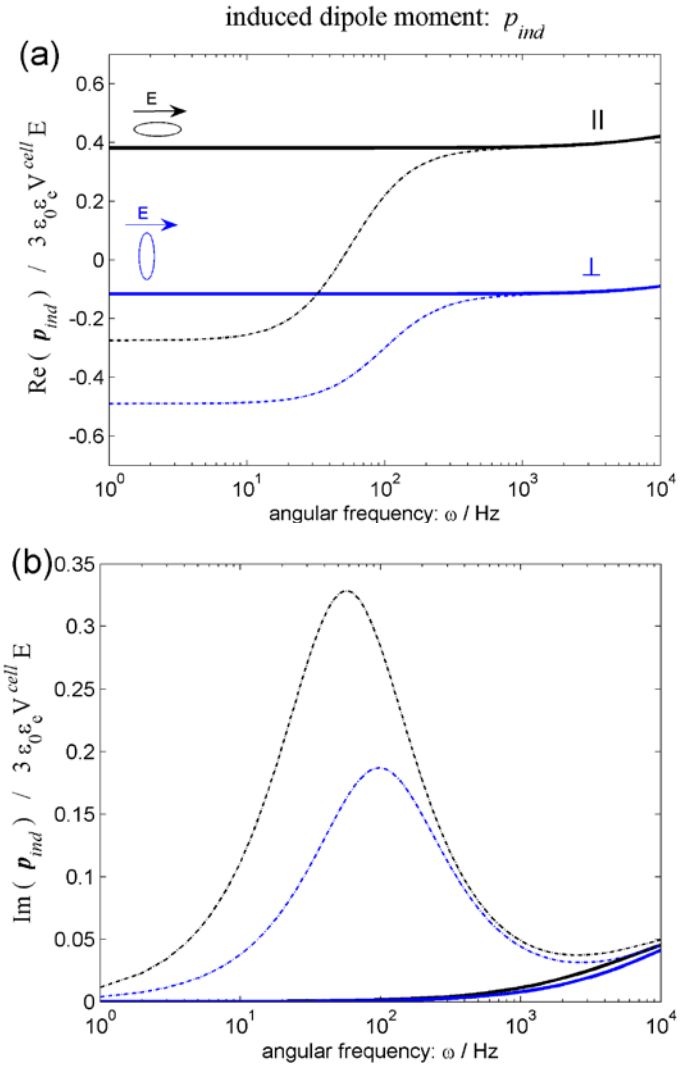

Fig. 1.5. The relative real (a) and imaginary (b) parts of the induced dipole moment of *E. coli* cell as function of frequency according to the classical model of diffuse double layer polarization (bold curves) and the new (Schwarz-like) polarization (dashed curves). The conductivity of the suspending medium is $K_e = 8 \times 10^{-4}$ S m (dielectric constant $\varepsilon_e = 78$, ion diffusion coefficient $D = 2 \times 10^{-9}$ m^2 s^{-1}). The dielectric constant of the cell membrane is $\varepsilon_m = 2$ ant the membrane conductivity $K_m = 0$. The *E. coli* cell is approximated by prolate ellipsoid with semi-major and semi-minor axes $a = 1$ µm and $b = 0.4$ ×µm, respectively. The ratio $\Theta = 12$ and the electrokinetic potential is $\varsigma = -40$ mV (for both, the classical and the *Schwarz*-like polarization model). Characteristic relaxation times $\tau_{II}^{i} = 3$ µs and $\tau_{\perp}^{i} =$

$(b/a) \times \tau_{II}^{i}$.

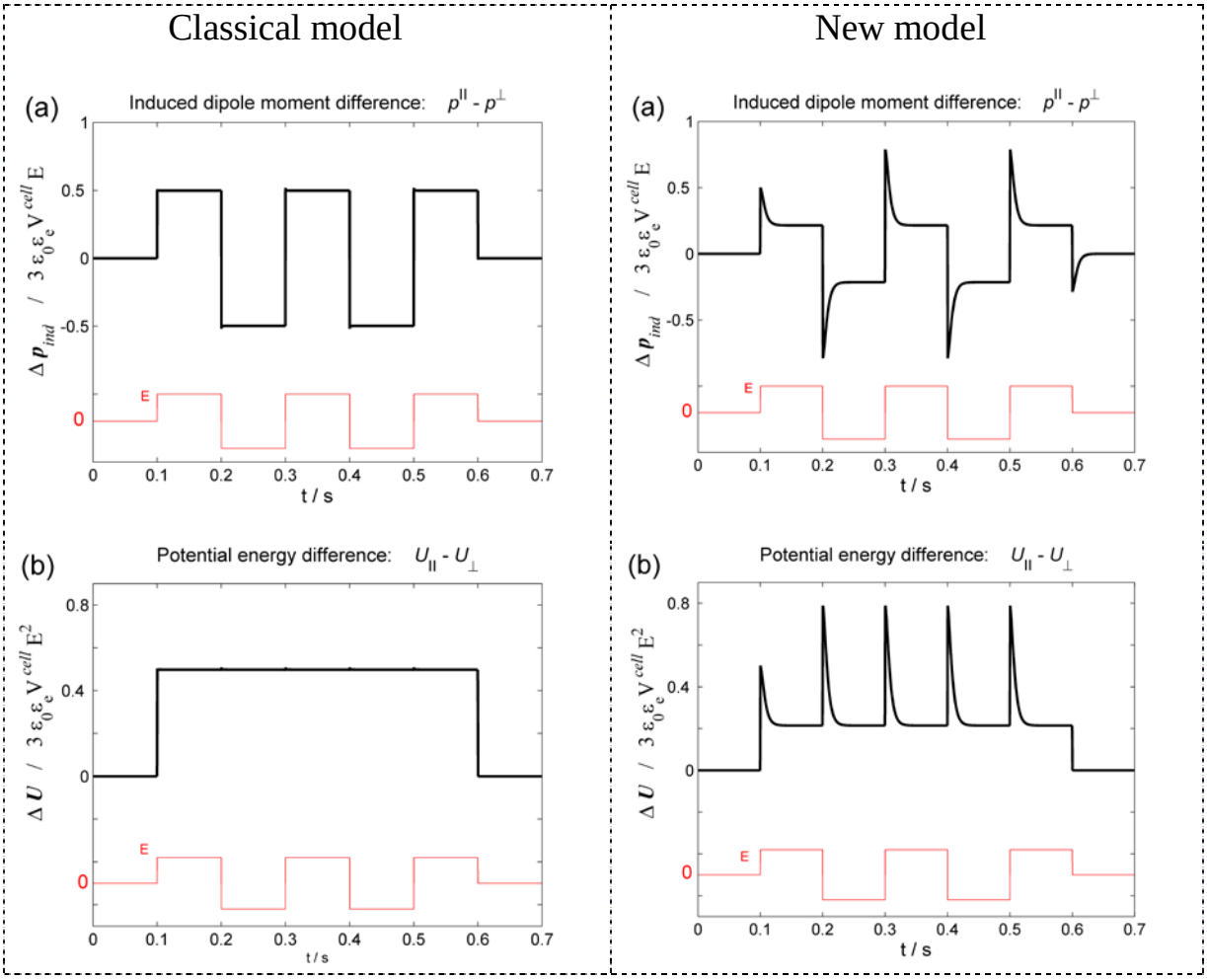

Fig. 1.6 The induced dipole moment difference $\Delta p_{ind} = p_{II} - p_{\perp}$, (a), and the potential energy difference $\Delta U = U_{II} - U_{\perp}$, (b), of an *E. coli* cell as functions of time according the classical model of diffuse counterion polarization (left) and the new model of polyionic glycocalyx polarization (right). The electric field is applied at t = 0.1 s. The electric field trace (amplitude *E*, frequency f = 5 Hz) is shown at the bottom of the figures. Same parameters as Fig. 1.4 and Fig. 1.5.

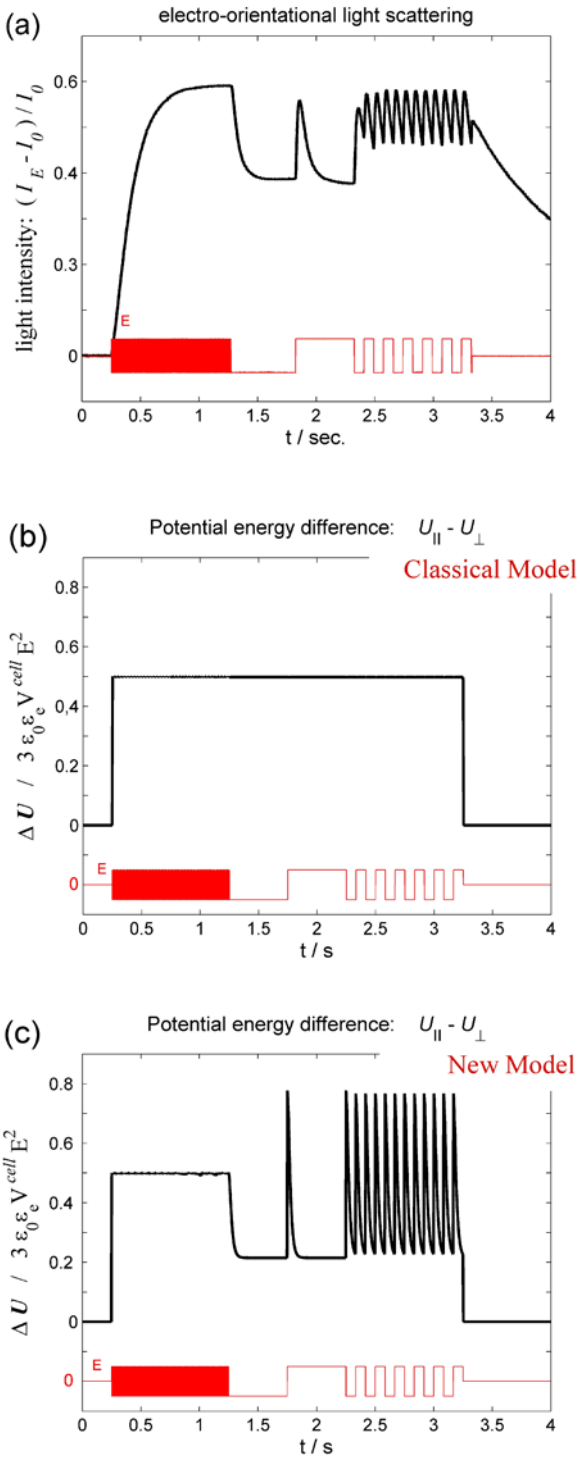

Fig. 1.7 Comparison between the electro-optical effect of suspension of *E. coli* cells (a) and the calculated potential energy difference $\Delta U = U_{II} - U_{\perp}$ according to the classical (diffuse) counter-ion polarization (b) and the new (*Schwarz*-like) polarization of the polyionic glycocalyx shell (c). Here, the characteristic relaxation times of the inner (glycocalyx) double layer polarization are $\tau_{II}^{i} = 10^{-2}$ s and $\tau_{\perp}^{i} = (b/a) \times \tau_{II}^{i}$. All other parameters as Fig. 1.4 and Fig. 1.5. The classical model of diffuse double layer polarization (b) cannot rationalize the modulation of the scattered light at low frequencies, whereas the proposed new model of *Schwarz*-like polarization of the cell glycocalyx (c) agrees with the experiment.

Conclusions

The polarization and orientation of *E. coli* cells in externally applied electric field is not consistent with the classical model of diffuse double layer polarization, but agrees with new model of *Schwarz*-like polarization of the polyionic glycocalyx of the *E. coli* cells, indicating that the new (proposed in Part II) is correct.

Appendix: Dipole coefficient of prolate ellipsoidal particle

The dipole coefficient $C^{*}_{\mathrm{II},\perp}(\omega)$, Eq. (2), of prolate ellipsoidal particle oriented parallel (||) and perpendicular (⊥) to the direction of the externally applied electric field is expressed by its low (0) and high (∞) frequency dispersion limits $C^{0}_{\mathrm{II}(\perp)}$ and $C^{\infty}_{\mathrm{II}(\perp)}$, respectively, as well as, by the (weighted average) characteristic times for the two cases of orientation, τ_{II} and $\tau_{\perp}$, respectively.[1] The expressions are given in the Appendix 1 and the Appendix 2.

Appendix 1: Prolate spheroid parallel to the applied field

$$C_{\parallel}^{0}=\frac{1}{2ab^{2}}\left(\gamma_{\parallel}^{+}+\gamma_{\parallel}^{-}\right) \tag{A.1}$$

$$C_{\parallel}^{\infty}=\frac{\left(\widehat{K}_{\mathrm{p}\parallel}-K_{\mathrm{e}}\right)\Big/3}{K_{\mathrm{e}}+\left(\widehat{K}_{\mathrm{p}\parallel}-K_{\mathrm{e}}\right)A_{\parallel}} \tag{A.2}$$

$$\tau_{\parallel}=\frac{\left(\gamma_{\parallel}^{+}+\gamma_{\parallel}^{-}\right)I_{\parallel}}{16\pi ab^{2}\left(C_{\parallel}^{\infty}-C_{\parallel}^{0}\right)D} \tag{A.3}$$

where K_{e} is the conductivity of the suspending electrolyte, a is the half the distance between the poles, b is the half the diameter of the equator and $\widehat{K}_{\mathrm{p}\parallel}$ is the conductivity of the particle together with its double layer, which is given by:

$$\widehat{K}_{\mathrm{p}\parallel}=\frac{3aK^{\sigma}}{2bh}\left[\frac{a^{2}-2b^{2}}{h^{2}}\operatorname{arctanh}\frac{h}{b}-\frac{b}{h}\right] \tag{A.4}$$

where

$$h=\sqrt{a^{2}-b^{2}} \tag{A.5}$$

In Eq. (A.4), K^{σ} is the surface conductivity, *a* and *b* are the semi-axes of the prolate ellipsoid of revolution (a>b). The rest parameters in the Eqs. (A.1) - (A.3) are:

$$\gamma_{\parallel}^{+} = ab^2 \frac{\left(\widehat{K}_{\mathrm{p}\parallel} - K_{\mathrm{e}}/2\right)/3}{K_{\mathrm{e}}/2 + \left(\widehat{K}_{\mathrm{p}\parallel} - K_{\mathrm{e}}/2\right)A_{\parallel}} \tag{A.6}$$

$$\gamma_{\parallel}^{-} = ab^2 \frac{-1/3}{1 - A_{\parallel}} \tag{A.7}$$

$$I_{\parallel} = \frac{3\pi}{5h^6}\left[-a^3b^2 \ln^2\frac{a+h}{a-h} + 2hb^2(a^2+b^2)\ln\frac{a+h}{a-h} + 4ah^2(a^2-2b^2)\right] \tag{A.8}$$

$$A_{\parallel} = \frac{ab^2}{h^3}\left[\operatorname{arctanh}\frac{h}{a} - \frac{h}{a}\right] \tag{A.9}$$

$$X_{\parallel} = \sqrt{\frac{1 + \widehat{K}_{\mathrm{p},\parallel}/K_{\mathrm{e}}}{1 + \widehat{K}_{\mathrm{p},\parallel}/2K_{\mathrm{e}}}} \tag{A.10}$$

Appendix 2: Prolate spheroid perpendicular to the applied field

$$C_{\perp}^{0} = \frac{1}{2ab^2}\left(\gamma_{\perp}^{+} + \gamma_{\perp}^{-}\right) \tag{A.11}$$

$$C_{\perp}^{\infty} = \frac{\left(\widehat{K}_{\mathrm{p}\perp} - K_{\mathrm{e}}\right)/3}{K_{\mathrm{e}} + \left(\widehat{K}_{\mathrm{p}\perp} - K_{\mathrm{e}}\right)A_{\perp}} \tag{A.12}$$

$$\tau_{\perp} = \frac{\left(\gamma_{\perp}^{+} + \gamma_{\perp}^{-}\right)I_{\perp}}{16\pi ab^2\left(C_{\perp}^{\infty} - C_{\perp}^{0}\right)D} \tag{A.13}$$

$$I_{\perp} = \frac{3\pi}{20h^6}\left[-ab^4 \ln^2\frac{a+h}{a-h} + 4h(a^4+b^4)\ln\frac{a+h}{a-h} - 4ah^2(3a^2-2b^2)\right] \tag{A.14}$$

$$\widehat{K}_{\mathrm{p}\perp} = \frac{3aK^{\sigma}}{2bh}\left[\frac{a^2}{2h^2}\operatorname{arccot}\frac{b}{h} + \frac{b\left(a^2-2b^2\right)}{2a^2h}\right] \tag{A.15}$$

$$\gamma_{\perp}^{+} = ab^2 \frac{\left(\widehat{K}_{\mathrm{p}\perp} - K_{\mathrm{e}}/2\right)/3}{K_{\mathrm{e}}/2 + \left(\widehat{K}_{\mathrm{p}\perp} - K_{\mathrm{e}}/2\right) A_{\perp}} \tag{A.16}$$

$$\gamma_{\perp}^{-} = ab^2 \frac{-1/3}{1 - A_{\perp}} \tag{A.17}$$

$$A_{\perp} = \frac{1 - A_{\parallel}}{2} \tag{A.18}$$

$$X_{\perp} = \sqrt{\frac{1 + \widehat{K}_{\mathrm{p},\perp}/K_{\mathrm{e}}}{1 + \widehat{K}_{\mathrm{p},\perp}/2K_{\mathrm{e}}}} \tag{A.19}$$

References

[1] Grosse, C., Pedrosa, S. and Shilov, V. N., *Calculation of the Dielectric Increment and Characteristic Time of the LFDD in Colloid Suspensions of Spheroidal Particles*, J. Colloid Interface Sci., **220**, 31-41 (1999).

2. Electroporation of *S. pombe* cells in the frequency range 10 Hz – 3kHz.

(field strengths range: $1 \leq E / (\mathrm{kV\ cm^{-1}}) \leq 1.5$)

2.1 Materials and methods

The *S. pombe* yeast cells are suspended in a weak electrolyte solution of 10^{-5}-10^{-3} M NaCl (volume fraction of the cells ≈ 0.01). The culture of *Schizosaccharomyces pombe* (*S. pombe*) 972h^{-} was propagated in YED (yeast extract 1%, glucose 2%) in Erlenmeyer flasks at 250 rpm and 24°C. The cells were washed 4 times in doubly-distilled water followed by final washing with NaCl solution of desired concentrations. The so prepared cell dispersions were mixed to become suspensions with a given ionic strengths of the medium.

The electroporation procedure is explained schematically in Fig. 2.1. The electroporation efficiency was measured by cellular uptake of propidium iodide (PI), a membrane impermeant fluorescent probe for nucleic acids (total concentration in the suspension of 4 μM). Amplifier, capable of delivering voltages of up to 200 V in the frequency range $0 \leq \nu / \mathrm{kHz} \leq 10$, supplied an square-wave (reverse-pulse) a.c. electric field (duration t_E = 4 s and amplitudes $E = (10 - 15) \times 10^4\ \mathrm{V\ m^{-1}}$) across the electroporation chamber (BioRad).

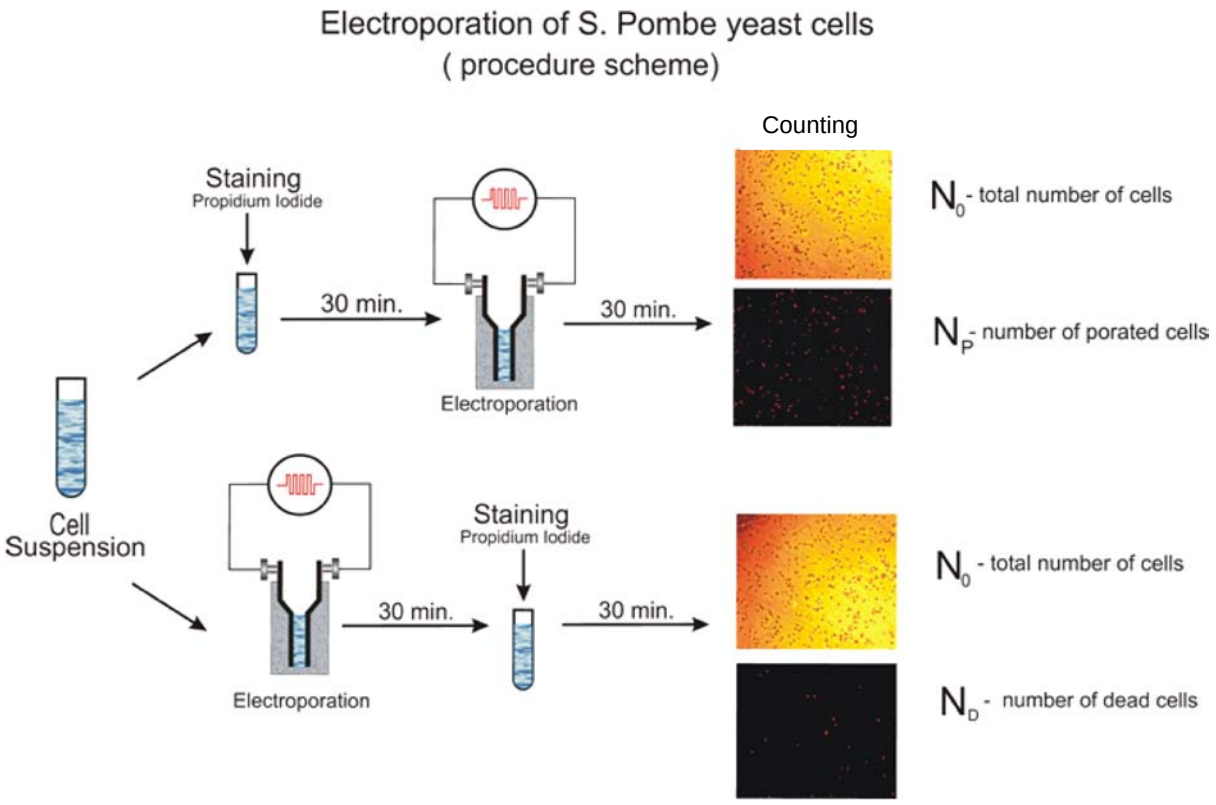

Fig. 2.1 The procedure scheme of the electroporation experiment

2.2 Results and discussion

The frequency dependence of the transmembrane voltage $U_m(\omega)$ is calculated using the expressions of Grosse and Schwan [1] deduced for the case of diffuse double layer polarization of a spherical cell. For the case of the new (*Schwarz*-like) polarization of the cell-glycocalyx, the frequency independent surface conductivity $K^{\sigma i}$ is replaced (as in Part II) by the Schwarz's frequency dependent surface conductivity: $K^{\sigma} = K^{\sigma d} \cdot [1 + i\omega\tau^{\alpha i} (1+ i\omega\tau^{\alpha i})^{-1} \Theta]$, where $\tau^{\alpha i}$ is the characteristic relaxation time of the inner (polyionic *glycocalyx*) shell and $K^{\sigma d}$ is the conductivity of the diffuse double layer, see Eq. (12) of Part II.

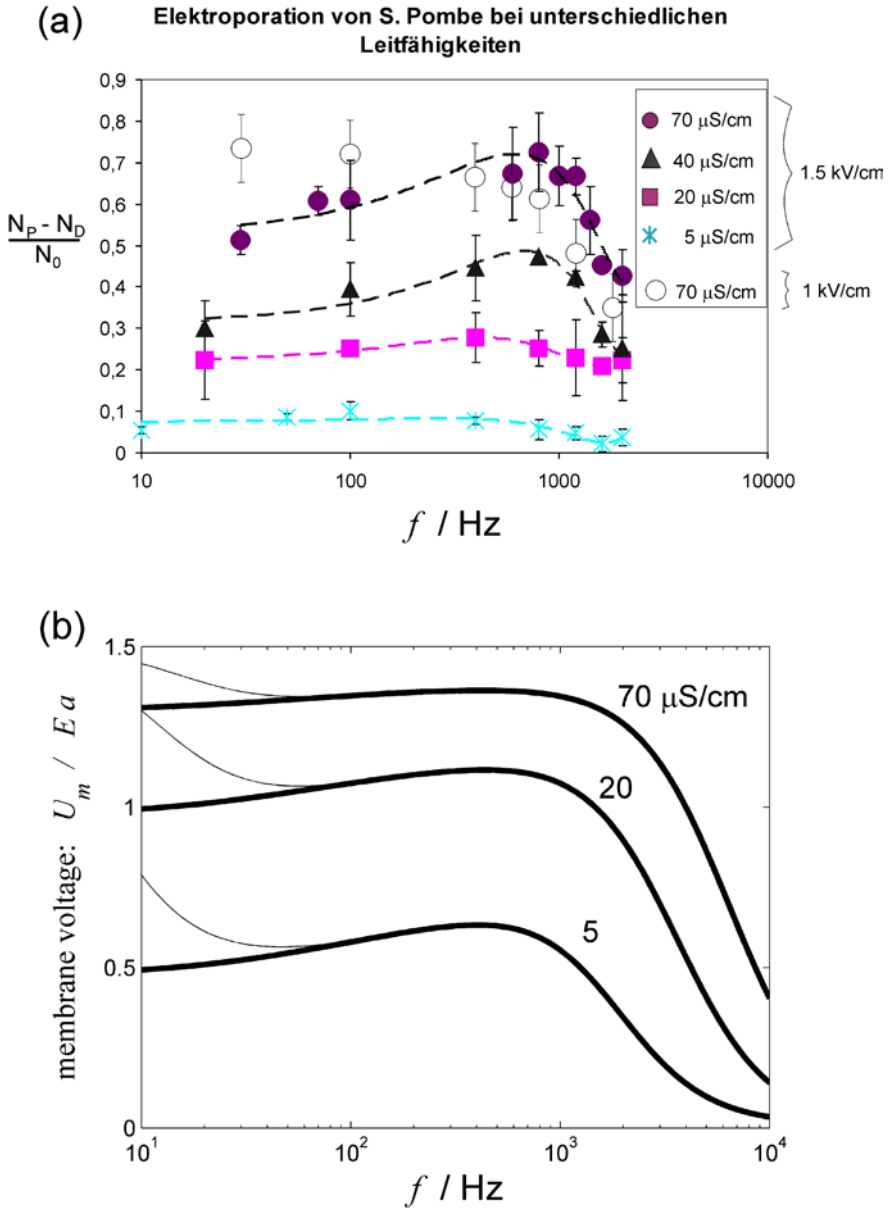

Fig. 2.2 (a) The efficiency of the electroporation of *S. pombe* cells as function of the conductivity of the suspending medium (NaCl, K_e = 5, 20 and 70 µS/cm), the frequency of the electric field (reverse a.c. field) and the field strength. (b) The theoretical prediction for the potential difference across the cell membrane as function of frequency and the conductivity of the suspending medium according to the classical (diffuse) double layer polarization model (bold curves) and the new (*Schwarz*-like) polarization model (thin curves). The cell is approximated as a prolate ellipsoid of revolution with semi-axes of $a = 5 \times 10^{-6}$ m and $b = 2.5 \times 10^{-6}$ m, capacitance of the membrane per unit area $C_m = 3 \times 10^{-2}$ F m^2, '*inner*' to '*diffuse*' surface conductivity ratio $\Theta = K^{\sigma i} / K^{\sigma d} = 27$ (obtained in Part II), electrokinetic potential $\varsigma = -56$ mV (at 5 µS/cm). Rest parameters: conductivity of the cell core $K_i = 10^{-2}$ S m^{-1} with dielectric constant $\varepsilon_i = 80$ and that of the cell membrane $\varepsilon_m = 2$.

Using the values $K^{\sigma d} = 10^{-10}$ S and $\Theta = K^{\sigma i} / K^{\sigma d} = 27$ obtained in Part II, and membrane capacitance per unit area $C_m = 3 \times 10^{-2}$ F m^2, we calculate the transmembrane voltage as function of frequency $U_m(\omega)$. The calculations are performed for both polarization models: the classical (*diffuse*) EDL-model and the proposed in Part II new (polyionic *glycocalyx shell*) polarization model. The results are given in Fig. 2.2(b), where the electroporation efficiency curves (Fig. 2.2(a)) are compared with the theoretical transmembrane voltage $U_m(\omega)$ (Fig. 2.2(b)). Since U_m is the driving force for the electroporation, we may use the theoretical $U_m(\omega)$ dispersion curves as a reference and by comparing the frequency dependencies of the electroporation efficiency with $U_m(\omega)$, to prove whether the *glycocalyx*-polarisation model is correct.

2.3 Conclusions

The electroporation efficiency of *S. pombe* yeast cells shows frequency dependence within the frequency range f = 3Hz … 3 kHz. The profile of the dispersion curves changes with the field strength: at field intensity amplitude E = 1 kV cm^{-1} it correlates with the new (*Schwarz*-like) flow-polarization of the polyionic *glycocalyx* shell of the yeast cells, whereas at E = 1.5 kV cm^{-1} it shows dispersion similar to that expected from the classical (diffuse) double layer polarization model. The change in the shape of the dispersion curves with increasing field strength indicates that the proposed new model of flow-polarization of the polyionic *glycocalyx* shell of the biological cells is correct.

2.4 References

[1] Grosse, C. and Schwan, H.P., *Cellular membrane potentials induced by alternating fields,* Biophys. J., **63**, 1632-1642 (1992).

Danksagung

Herrn Prof. Dr. E. Neumann danke ich recht herzlich für die Themenstellung und die zahlreichen Diskussionen, die zu neuen Ergebnissen, wie sie in dieser Arbeit zum Teil vorgestellt werden, geführt haben. Weiterhin danke ich Herrn Prof. Neumann für die Möglichkeit, in seiner Forschungsgruppe zu arbeiten, wo ich nicht nur, neue biophysikalische Methoden und Messtechniken, sondern auch, viele interessante Leute kennen gelernt habe.

Herrn Prof. Dr. T. Hellweg danke ich für die freundliche Bereitschaft, das Zweigutachten zu übernehmen und für die Gastfreundschaft die endgültige Form dieser Arbeit in seiner Arbeitsgruppe zu schaffen.

Herrn Dr. S. Kakorin danke ich für die gute Zusammenarbeit, die fundierten Diskussionen und für seinen guten Rat bei der Fertigung der Publikation.

Herrn Dr. C. R. Rabl danke ich für die technische Unterstützung bei der Erweiterung der Feldsprunganlage für die elektrooptischen Untersuchungen in dem längeren (Mikrosekunden) Zeit-Skala Bereich.

Weiterhin danke ich Herrn Priv. Doz. Dr. U. Pliquett für die Einführung in die MATLAB-Programmierung und die Unterstützung bei wichtigen elektronischen Neuerungen.

Frau Dr. K. Tönsing danke ich herzlich für die gute Zusammenarbeit.

Herrn Uwe Güth danke ich für seine Hilfsbereitschaft und sehr akkurate Präparation der Zell-Kulturen und Kolloid-Lösungen.

Nicht zuletzt danke ich herzlich Frau Ina Ehring und Frau Claudia Pudel für die sehr sorgfältige, oft mühsame Präparation und Dialyse der Vesikel-Lösungen.